

UNIVERSITY OF OKLAHOMA
GRADUATE COLLEGE

LABEL-FREE, LIVE CELL NANOPARTICLE IMAGING FOR REAL-TIME UPTAKE
PATHWAY ANALYSIS

A THESIS
SUBMITTED TO THE GRADUATE FACULTY
in partial fulfillment of the requirements for the
Degree of
MASTER OF SCIENCE

By
EVAN MATTHEW METTENBRINK
Norman, Oklahoma
2022

LABEL-FREE, LIVE CELL NANOPARTICLE IMAGING FOR REAL-TIME UPTAKE
PATHWAY ANALYSIS

A THESIS APPROVED FOR THE
STEPHENSON SCHOOL OF BIOMEDICAL ENGINEERING

BY THE COMMITTEE CONSISTING OF

Dr. Stefan Wilhelm, Chair

Dr. Wei Chen

Dr. Rebecca Scott

Abstract

Nanoparticles are biomedical devices capable of a wide range of applications ranging from drug delivery to molecular sensing and bioimaging agents. Within bioimaging, nanoparticles face numerous obstacles in both *in vitro* and *in vivo* applications. Upconversion nanoparticles, capable of absorbing photons and emitting photons at a shorter wavelength, provide a promising modality for addressing many of these *in vitro* and *in vivo* obstacles, including low background, comprehensive surface coating options, and applications in multimodal imaging. When considering specific applications however, such as monitoring of nanoparticle endocytosis, simpler, more environmentally friendly, and more cost-effective techniques could improve the rate at which research is conducted by reducing the overhead cost and laboratory expertise required to run such an experiment. To those aims, this thesis serves two primary purposes: first to introduce, evaluate, and direct the current research aimed at developing upconversion nanoparticles as a widely used bioimaging modality, and then to develop a simple technique capable of monitoring living cell nanoparticle uptake rates in a model macrophage system.

Table of Contents

1. Literature Review	1
a. Thesis Introduction	
b. Upconversion Nanoparticles in Bioimaging	
i. Introduction	
ii. Basic Concepts of Upconversion Nanoparticles	
1. <u>The Photophysical Mechanisms of Photon Upconversion</u>	
2. <u>Imaging in the Near-Infrared Range</u>	
3. <u>Tunability</u>	
iii. Bioimaging of Individual Upconversion Nanoparticles	
1. <u>Photostability</u>	
2. <u>Upconversion Luminescence Enhancement</u>	
3. <u>Super-Resolution Imaging</u>	
iv. Bioimaging of Upconversion Nanoparticles in Live Cells	
1. <u>Cytotoxicity</u>	
2. <u>Surface Modification</u>	
3. <u>Multiplexed Imaging</u>	
4. <u>Cellular Actions</u>	
v. Bioimaging of Upconversion Nanoparticles in Whole Animals	
1. <u>Biocompatibility & Biodistribution</u>	
2. <u>Imaging Depth</u>	
3. <u>In Vivo Targeting</u>	

vi. Applications of Upconversion Nanoparticles in Multimodal Bioimaging	
vii. Limitations in Advancement of Upconversion Nanoparticle Bioimaging	
viii. Conclusions	
c. Live Cell Nanoparticle Uptake Imaging	
i. Light Scattering Imaging	
ii. Endocytosis Pathways	
iii. Heparosan Gold Nanoparticle Model	
iv. Project Introduction and Goals	
2. Materials and Methods	42
a. Gold Nanoparticle Synthesis and Characterization	
b. PEGylation of Gold Nanoparticles	
c. Creation of Gold Nanoparticle Polyacrylamide Gels	
d. Confocal Imaging of Polyacrylamide Gels	
e. Preparation of Cy5-Labeled Gold Nanoparticles	
f. Photostability Study Imaging Experiment	
g. Heparosan Coating of Gold Nanoparticles	
h. Culture of RAW 264.7 Macrophages	
i. Fixing of Cells	
j. Cell Imaging Settings	
k. Live-Cell Heparosan-Coated Gold Nanoparticle Uptake Study	
3. Results	50

a.	Correlation of Scattered Light Intensity and Gold Nanoparticle Size	
b.	Photostability of Cy5-Gold Nanoparticles in Fluorescent and Scattered Light Imaging	
c.	Live Cell Imaging Validation and Optimization	
d.	Fixed Cell Nanoparticle Uptake	
e.	Live Cell Endocytosis Pathway Monitoring of Gold Nanoparticles	
4.	Discussion & Future Directions	55
a.	Discussion	
b.	Future Directions	
c.	Contributions	
5.	Acknowledgements	58
6.	Figures	59
a.	Figure 1: Interactions Between Light and Biological Tissue	
b.	Figure 2: Visualization of Individual Upconversion Nanoparticles Through Super-Resolution Techniques	
c.	Figure 3: Potential Approaches for Upconversion Nanoparticles-Based Multiplexing in Cellular Imaging	
d.	Figure 4: Upconversion Nanoparticles Enable Multimodal Bioimaging and In Vivo Imaging	
e.	Figure 5: Agarose Gels	
f.	Figure 6: Correlation of Scattered Light Intensity and TEM Size in Gold Nanoparticles	
g.	Figure 7: Photostability of Light Scattering Imaging	

h.	Figure 8: Effect of Frame Averaging	
i.	Figure 9: Effect of Background Filtering	
j.	Figure 10: Heparosan Coating of AuNPs	
k.	Figure 11: Fixed Cell Imaging of Heparosan AuNPs with Uptake Inhibitors	
l.	Figure 12: Live Cell Imaging of Heparosan AuNPs with Uptake Inhibitors	
m.	Figure 13: Quantification of Heparosan AuNP Nanoparticle Uptake	
7.	Tables	74
a.	Table 1: Select Examples of Bioimaging Applications with Upconversion Nanoparticles	
b.	Table 2: Reagents Used in Synthesis of Gold Nanoparticles of Varying Size	
c.	Table 3: Characterization of Synthesized Nanoparticles	
8.	References	84

1. Literature Review:

a. Thesis Introduction & Aims

This thesis serves two primary purposes: first, to explore upconversion nanoparticles, a versatile bioimaging agent with strong potential for future growth, and second to highlight and experimentally validate a relatively simple, low-cost, label-free bioimaging method to monitor endocytosis pathways in living cells.

b. Upconversion Nanoparticles in Bioimaging

i. Introduction

Bioimaging enables the spatiotemporal visualization of biological processes at scales ranging from the molecular level to whole organisms using a wide-range of techniques and modalities. These modalities include light, ultrasound, magnetic resonance, X-rays, and other types of radiation to capture processes within complex biological systems.^{[1], [2], [3]} To facilitate the visualization of these processes and to enhance the imaging contrast, nanoparticles are often used.^[4] Advancements in bioimaging have realized a unique type of nanoparticles, called upconversion nanoparticles (UCNPs), that show promise due to their ability to be applied with many imaging modalities, including optical imaging.^[5]

With overall dimensions in the nanoscale size range, UCNPs are often made from crystalline inorganic host materials that are doped with lanthanide ions.^[6] These lanthanide ions enable the unique optical properties of UCNPs, resulting in anti-stokes luminescence.^[7] The anti-stokes (or upconversion) luminescence is generated by the sequential absorption of multiple low-energy (or longer wavelength) photons followed by the emission of a photon with a relatively higher energy (or shorter wavelength).^{[8],[9],[10]} The photon upconversion phenomenon has been used in a wide array of applications including solar cell enhancement,^[11] biological and chemical sensing,^{[12],}

[13],[14],[15],[16] photodynamic therapy,^[17] diagnostic devices,^{[18], [19]} photoactivated gene editing,^[20] and even to give mice infrared vision capabilities.^[21]

While sometimes criticized for their relatively low overall quantum yields when compared to fluorescent probes and quantum dots, UCNPs have vast potential in bioimaging due to a unique combination of properties and capabilities not found in other imaging probes including: (1) A relatively high absorbance cross-section of lanthanides, the essential dopant ions of UCNPs, in the near-infrared (NIR) range paired with multi-photon upconversion capabilities to enable excitation and emission in the 700-1,000 nm range where biological tissue shows relatively low attenuation, known as the NIR-I optical window.^[22] (2) An ability to both absorb two, three, or more photons as well as emit multiple wavelengths across the ultraviolet, visible, and NIR spectra enables applications in super-resolution imaging, multiplexed bioimaging, and tuning of emission spectra.^{[23], [24]} (3) Energy transitions with extended time frames as well as the engineering of nanoparticle architecture allowing for wide spans of emission lifetimes ranging from micro- to milliseconds.^[25] (4) A non-blinking, photostable, and reliable luminescence signal enabling stable imaging for accurate comparative, or long-term observational studies.^[26] (5) Luminescence origins within the nanoparticle, allowing for an ever-expanding library of surface modifications to enable targeting, sensing, energy-transfer, prolonged circulation/reduced toxicity upon exposure to biological systems, or light-activated nanodevices with minimal effects on luminescence.^{[27], [28], [29],[30]} (6) Ease of compositional modification and tunability to enable X-ray, magnetic resonance, photoacoustic, or single-photon emission computed tomography-based multimodal imaging for added potential in clinical applications.^[31]

While fluorescent probes may have NIR capabilities and are being developed for multi-photon applications, these probes often exhibit limited photostability, have a substantially lower range of

possible emission lifetimes,^[32] have limited upconversion capabilities, and typically lack the multimodal potential found in UCNPs. Quantum dots and carbon dot nanoparticles exhibit relatively higher photostability, but only recent research has enabled their use in NIR-NIR imaging.^[33] In addition, these nanoparticles are often prone to photoblinking^[34] and have limited capabilities regarding photon upconversion than UCNPs.^[35]

To investigate the intersection of bioimaging and UCNPs, this review seeks to introduce the readers to the photophysical mechanisms, advantages, and limitations, as well as applications of UCNPs. We highlight recent advancements in the field before focusing on how UCNPs address the primary needs for bioimaging probes at the individual nanoparticle level, including upconversion luminescence tunability, photostability, quantum yield, and super-resolution; the cellular level, including UCNP cytotoxicity, surface modification, multiplexing, and enacting cellular processes; and the whole animal level, including UCNP biocompatibility and biodistribution, imaging depth, *in vivo* targeting, and multimodal imaging. Additionally, this review provides a perspective on the current state of UCNP bioimaging and identifies opportunities and challenges in advancing this technology. Finally, we hope that this review will serve as a useful resource for researchers who wish to explore UCNPs as a potential technology for enhancing their own bioimaging experiments.

ii. Basic Concepts of Upconversion Nanoparticles

1. The Photophysical Mechanisms of Photon Upconversion

To achieve photon upconversion, UCNPs often employ two separate classes of lanthanide ions, called the sensitizer and activator ions that are added to the crystalline UCNP host material during synthesis. The sensitizer ion (often ytterbium) has an absorbance peak in the NIR range, typically ~980 nm, and can transfer energy in its excited state to activator ions (often erbium, thulium, or holmium).^[2] To enable this transfer, the UCNP design requires selection of lanthanide ions with matching or closely matching excited energy levels, enabling electron transfer between them. These energy levels further dictate the wavelength of the emitted (upconverted) photon. Depending on which activator energy state the electrons occupy, the wavelength of the emission will vary. For example, the $^4F_{9/2} \rightarrow ^4I_{15/2}$ and $^4I_{13/2} \rightarrow ^4I_{15/2}$ energy transition in erbium results in the emission of a 660 nm and 1532 nm wavelength photon, respectively, and the $^1G_4 \rightarrow ^3H_6$ transition in thulium results in the emission of a 478 nm wavelength photon.^{[36], [37]} Since each of these energy transitions involves the absorption and transfer of different numbers of photons, a single UCNP will typically multiple prominent upconversion emission peaks upon excitation. Notably, anti-Stokes shifts between excitation and emission wavelengths as high as ~1,200 nm are possible.^[38] ^[39] Przybylska and colleagues presented a diagram summarizing the corresponding energy transitions in common UCNP sensitizer/activator ion systems and their resultant emission wavelengths and number of involved photons following ~976-nm excitation.^[40] If multi-wavelength emission is unwanted in a specific application, these photophysical upconversion processes can be engineered to isolate specific emission wavelengths by targeting energy transitions through modulation of the excitation laser.^[41]

It is worthwhile to note that a common form for the nomenclature of UCNPs is to start with the core matrix, followed by the activator and sensitizer ions along with their doping ratios, and then an “@” sign denoting each additional shell around the core matrix. For example, an NaYF₄: 20% Yb³⁺, 2% Er³⁺@ NaYF₄ UCNP would have a sodium yttrium fluoride core matrix with an ytterbium sensitizer and an erbium activator surrounded by a shell made of sodium yttrium fluoride. The UCNP’s core matrix would contain the following mol percentages: 78% yttrium, 20% ytterbium, and 2% erbium.

2. Imaging in the Near-Infrared Range

An important feature of UCNPs is that they enable the imaging in the NIR range with typical excitation wavelengths of ~808 nm or ~980 nm. In some circumstances, even longer wavelengths have been used (Table 1). The primary advantages of NIR imaging are deeper tissue penetration of the light and reduced phototoxicity of the tissue upon exposure to incident light.^[42] Additionally, tissue components, namely erythrocytes and collagen, display autofluorescence when exposed to visible light excitation sources, increasing signal background and decreasing the signal-to-noise ratio in imaging experiments. Photon upconversion imaging in tandem with NIR excitation circumvent these issues because NIR light drastically reduces tissue autofluorescence as compared to visible light excitation.^[43]

The enhanced light penetration by NIR light was modeled by Ash *et al.* and is summarized in Figure 1A.^[44] The figure depicts the corresponding tissue depth at which incident light is reduced to 1% of its original intensity in a dermal model. The observed increase in light penetration is due to the chromophores in dermal tissues having lower extinction coefficients at longer wavelengths.^[44] The light attenuation in tissue is driven primarily by two factors: (i) absorbance,

i.e. light absorption by tissue components, including molecules and ions, and (ii) scattering, i.e. incident light being redirected when travelling through tissue often due to changes in refractive index in tissue components (Figure 1B).^{[45], [46], [47], [48]}

As shown in Figure 1C, NIR-I (700-1,000 nm) light exhibits reduced absorbance (and extinction, i.e. the combination of absorption and scattering) in tissue, which enables deeper light penetration. In addition, these longer wavelengths cause reduced tissue phototoxicity than shorter wavelengths, enabling the use of increased laser power without increasing the energy being transmitted to the tissue, which may otherwise result in tissue hyperthermia and cell death.^{[49], [50]} This deeper light penetration of tissue and reduction of phototoxic effects on tissue provide NIR UCNP with enhanced utility in full-body *in vivo* bioimaging.

Within the NIR-I optical window (700-1,000 nm), the performance of excitation lasers is not all equal. For example, early UCNP research focused more heavily on the 980-nm laser excitation due to ytterbium, the most common UCNP sensitizer, having a relatively strong absorbance peak at ~980 nm.^[51] However, as shown in Figure 1C, water exhibits an absorbance peak in the 980 nm wavelength range, causing a reduction in imaging depth when using ~980 nm lasers in comparison to 808 nm lasers, with one study finding 808 nm lasers penetrate 50% deeper than a 980-nm excitation laser in tissue.^[52] Additionally, 808-nm lasers, due to the decrease in water's light absorbance, lead to a reduction in photothermal effects in tissue as well as associated phototoxicity.^{[53], [54]} Potentially even further supporting the benefits of using 808-nm excitation lasers, Nd³⁺, commonly used in lieu of, or in tandem with Yb³⁺ to sensitize UCNP to 808 nm excitation, exhibits a relatively stronger absorbance at 808 nm than Yb³⁺ at 980 nm, leading to an increase in upconversion luminescence in UCNP doped with both ions.^[55]

3. Tunability

An additional characteristic of UCNPs is their tunability of the corresponding emission lifetimes. One way this emission lifetime tunability can be achieved is through selecting specific ions or combinations of ions. For example, UCNPs with a commonly used activating ion, Tb^{3+} , exhibit an emission lifetime lasting 3.64 ms, whereas Er^{3+} -doped UCNPs exhibit a notably shorter emission lifetime of 0.13 ms.^[56] This phenomenon is exploited in time-gated imaging, where the emission signals are collected at different timepoints to reduce background or to view multiple agents with a single excitation and emission wavelength.^{[56], [57]} Leading research has shown significant reductions in spectral lifetimes to as short as 2 μs .^[58] Multiple other groups have varied dopant ion concentrations to obtain spectral lifetimes as short as 25.6 μs to longer than 1 ms for specific hybrid UCNPs, enabling multiple probes to be imaged in rapid succession from a single excitation laser.^{[59], [60], [61], [62]}

In addition to the luminescence lifetime tunability, UCNPs have been engineered to emit in the entire visible spectrum and beyond. Full-spectrum chromatic tuning of UCNP-perovskite quantum dot (UCNP-PeQD) hybrids has been demonstrated with an increase in emission wavelength range from what has been achieved with either UCNPs or PeQDs alone. These results indicate a synergistic effect between the two nanoparticle types.^[59] Initial attempts at full-color tuning involved selecting different activator lanthanide ions for the nanoparticle core to take advantage of their unique emission profiles.^[63] A recent study showed that a single architecture of multi-shell UCNPs can be designed to emit a full spectrum of colors in response to a single excitation wavelength with varying pulse lengths.^[64]

Another study showed the fabrication of UCNPs with emission peaks at 540 nm and 654 nm. The ratio of the emission peaks were altered through excitation with 800-nm, 980-nm, or 1,530-

nm lasers.^[65] A similar effect was achieved when altering the voltage applied to the UCNPs, resulting in a voltage-dependent red, green, or yellow emission upon laser excitation.^[66] Similarly, due to the multiple emission peaks of UCNPs, bandpass filters can be used to isolate the emission wavelength of specific luminescence peaks. For example, one study specifically used the 455-nm emission peak of Yb/Tm particles for multiplexed super-resolution imaging.^[24]

Using multiple lanthanide dopants in the same UCNP or cluster of UCNPs has led to the design of particles with light-dependent action. In one study, UCNP clusters were synthesized with orthogonal activation capabilities, enabling 980-nm excitation to be used for UCNPs tracking and a 808-nm excitation to release a drug molecule from the UCNP cluster.^[67] Other researchers have found that, in addition to lanthanides and their compositional ratios, emission properties may be affected by various factors, including sample concentration, temperature, surface modification, and excitation power.^{[68], [69], [70]}

iii. Bioimaging of Individual Upconversion Nanoparticles

Ensemble imaging of UCNPs is often used for *in vivo* imaging applications, but notable research is aimed at imaging and quantifying of individual nanoparticles. For example, recent advancements in elemental analysis enable the quantification of chemical compositions and reactions kinetics of individual colloidal nanoparticles.^{[71], [72]} The spatiotemporal visualization of individual nanoparticles enables investigations into nanoparticle dynamics and the analysis of nanoparticle heterogeneity in structure or luminescence, which can impact biological outcomes.^[73]^{[74], [75]} At the individual particle level, the ideal UCNP exhibits a few key properties. First, the ideal UCNP is photostable, meaning that the signal does not noticeably decrease in intensity upon continued excitation. Next, the ideal UCNP has a relatively high quantum yield, defined as the ratio of emitted upconversion photons and the photons absorbed by the upconversion system.^[76] Brightness and quantum yield are sometimes considered limitations of UCNPs in bioimaging experiments, but may be balanced by other photophysical characteristics of UCNPs, including anti-stokes luminescence with long emission lifetimes and photostability. Further, at the individual nanoparticle level, individual UCNPs can be resolved at sub-diffraction limit distances with super-resolution imaging.

1. Photostability

One of the most prominent advantages to using UCNPs in imaging applications is the ability to excite with NIR lasers and capture light in the visible range. This anti-stokes luminescence behavior reduces image background noise, sample autofluorescence, and tissue overheating. However, the NIR excitation is not unique to UCNPs as NIR fluorescent probes have also been developed to achieve similar advantages of NIR excitation. By utilizing detectors in the NIR-II

range (900-1,700 nm), downconverting NIR fluorescent probes enable impressive imaging results.^{[77], [78], [79]} However, in comparison to quantum dots, carbon dots, and UCNPs, when excited for extended periods of time, traditional fluorophores, including NIR dyes, tend to photobleach. Photobleaching is the process by which cycling between excited, and ground-states of the molecule causes irreversible damage to the molecular structure of the probes, reducing or eliminating a dye's ability to emit light when excited.^[80]

Quantum dots are another imaging probe that are commonly used in nanoparticle applications.^{[81], [82], [83]} However, quantum dots are sometimes less photostable than UCNPs and are often prone to luminescence intermittency, or photoblinking, during imaging experiments.^[34] UCNPs, in contrast, have been shown to exhibit strong, unchanged, and continuous signals for greater than one hour of uninterrupted excitation.^{[84], [85], [22], [41], [86]} In addition, the non-blinking, steady signal makes UCNPs an ideal contrast agent for experiments requiring imaging over extended periods of time, such as cellular uptake or (intracellular) nanoparticle tracking experiments.^[73] It is worth noting that when combining UCNPs with organic dyes for photodynamic therapy or imaging applications, the photostability of the UCNP-dye hybrid is typically limited by the photobleaching properties of the dye rather than the UCNP.

2. Upconversion Luminescence Enhancement

Extended UCNP imaging experiments with high laser powers can lead to tissue overheating due to water exhibiting an absorption peak in the NIR range.^{[87], [88], [89]} One potential way to overcome this challenge is to engineer UCNPs with higher quantum yields to achieve enhanced luminescence intensities with lower laser excitation powers. Initial UCNP systems oftentimes resulted in quantum yields of <5%, whereas quantum dots and fluorescent probes are regularly

able to achieve >50% quantum yields, and recent carbon dots have quantum yields as high as 86%.^{[89], [5], [90], [91]} More recent studies reported UCNPs quantum yields in the 5-7% range.^{[92], [93]} Jones *et al.* proposed an initial framework for standardizing quantum yield measurements to enable better comparability between studies.^[93] A common cause for the low upconversion luminescence quantum yield is concentration quenching, where UCNPs with high lanthanide dopant ion concentrations will either transfer their excitation energy to the surface or to nearby dopant ions, instead of through photon emission.^{[8], [94], [95]}

Additional research has shown reductions in luminescence intensity as a result of quenching, dissolution, and leaching of dopant ions when in solution, specifically aqueous solutions.^[96] However, this effect may be overcome through intentional selection of surface coatings.^[27] Simply increasing lanthanide ion concentration can lead to increased intensity due to increased ion concentrations, but does not necessarily lead to an increase in quantum yield.^{[39], [97]} A well-established approach to increasing upconversion emission intensity and quantum yield is adding a shell to the UCNP architecture, which often consists of the same material as the core without sensitizing and activating ions. One group found a 13x increase in upconversion luminescence intensity simply by adding a shell to the UCNPs.^[98] Other research found the shell-mediated upconversion luminescence enhancement varies depending on the core/shell material, with enhancements ranging from 5-167.7 fold enhancement.^{[99], [100]} These enhancement quantities may vary between upconversion emission peaks as well as between excitation laser power.^[88] Researchers have investigated the optimal thickness of the shell, which leads to an increase in upconversion luminescence efficiency by increasing the distance between the luminescent core and potential luminescence quenching molecules around the particle, and results tend to point to an optimal shell thickness of ~5 nm.^[76]

Other approaches to upconversion luminescence enhancements have focused on engineering homogeneous UCNPs to maximize the number of ions in a single particle while maintaining the distance separating them to prevent cross-relaxation.^{[65], [101]} Another luminescence enhancement is through creating dye-UCNP hybrids, selecting dyes with energy transfers that closely match the selected lanthanide, enabling efficient energy transition between the two. For example, an ATTO 542 dye was adsorbed onto the surface of erbium-doped UCNPs and resulted in 2-3x increase in quantum yield when compared to the as-synthesized particles.^[102] Other research achieved as high as an 18x increase in upconversion luminescence intensity when the optimal amount of Ag₂Se quantum dots were added to quantum dot-UCNP composites.^{[103], [104]} Dye-mediated upconversion luminescence enhancement was found to increase luminescence by 283% when the sensitizer ytterbium was integrated into the shell of the UCNPs to further facilitate dye-core energy transfer.^[105]

Although not the focus of this review, it is important to note that numerous studies use upconversion-capable lanthanide nanoparticles for downconversion luminescence applications often utilizing the NIR-II (1,000-1,700 nm) emissions in conjunction with 980-nm or 808-nm excitation lasers. These luminescence downconversion capabilities have been successfully applied to cell targeting/phototherapy,^{[106], [107]} *in vivo* multiplexing,^{[108], [109], [110], [37]} and imaging optimization.^{[79], [104]} For more information on the topic, Yang and colleagues recently published a review covering NIR-II emitting lanthanide fluorescent probes.^[111]

In addition to the nanoparticles themselves, excitation lasers can be altered to enhance emission intensity in UCNP applications. For example, Yan *et al.* observed a 49% increase in upconversion luminescence signal when ytterbium/erbium UCNPs were simultaneously excited with both 1,550-nm and 980-nm lasers compared to the summation of both intensities individually, potentially

pointing at a synergistic effect in multi-laser excitation.^[63] Additionally, the use of a laser cavity in the excitation laser increased upconversion emission intensity by an order of magnitude.^[112] Wen *et al.* recently published a review more focused on enhancing upconversion luminescence quantum yields for further reading.^[8]

3. Super-Resolution Imaging

In addition to a consistent luminescence signal, imaging experiments with the aim of studying interactions of individual nanoparticles require the ability to resolve individual particles that are located near each other. In light microscopy, the resolution limit is determined by Rayleigh's criterion, stating that the minimum distance that can be resolved between two separate sources is governed by the Equation 1:

$$R = 0.61 * \lambda / n_a \quad \text{Equation 1}$$

where R represents the lateral resolution limit, λ represents the objects' emission wavelength, and n_a is the numerical aperture of the objective lens.^[113] Other similar equations exist dictating the lateral resolution of optical imaging such as Abbe and Sparrow resolution, but only differ in the leading coefficient.^[114]

As a result, typical resolution limits in light microscopy are ~200 nm. One important note is, as wavelength increases, so does the associated resolution limit. Additionally, the resolution limit of optical microscopy is also dependent on the number of photons being absorbed by the imaging probe due to the difference in emission intensity between the center and edges of the excitation laser, enabling multi-photon microscopy to achieve super-resolution images.^{[23], [115]} This reduction

divides the resolution limit by the square root of the number of photons involved in the upconversion process, providing inherently multi-photon UCNPs with increased utility in super-resolution imaging.^[23]

Recent research has developed other techniques aimed at super-resolution imaging. Improvements in resolution through different super-resolution techniques are visually portrayed in Figure 2. One commonly used super-resolution technique is stimulated emission depletion microscopy (STED). In STED, an excitation laser is rapidly followed by a longer wavelength, doughnut-shaped de-excitation laser, reducing signal from objects outside of the doughnut's center, providing improved resolution.^[116] Liu *et al.* applied STED to image UCNPs at resolutions as low as 28 nm by using a 980-nm excitation laser combined with an 808-nm STED laser to isolate the $^3\text{H}_4 \rightarrow ^3\text{H}_6$ transition, achieving the desired reduction in resolution (Figure 2A).^[41] In comparison to the 4-ms pixel dwell time achieved by Liu *et al.*, Peng *et al.* reported a 400-fold reduction in pixel dwell time to 10 μs in STED by increasing dopant ion concentrations while still achieving a lateral resolution limit of 72 nm.^[117]

Alternatively to STED, Chen *et al.* used a single doughnut beam excitation laser to enable NIR-NIR excitation-emission of UCNPs through a 93- μm tissue sample, achieving a lateral resolution of <50 nm. This technique was termed “near-infrared emission saturation nanoscopy” (NIRES).^[118] Additionally, the authors found UCNPs with lower lanthanide ion doping concentrations had lower resolution limits when compared to highly-doped UCNPs at equivalent laser excitation powers.^[118] Chen further developed a technique requiring the same single doughnut-shaped excitation laser, but instead using both 800-nm and 740-nm emissions from the UCNPs to decode images and achieve a resolution of 40 nm, or ~4% of the excitation wavelength.^[119] Similarly, the same research group used a Bessel beam, whose amplitude is

defined by a first-order Bessel function, reporting an excitation power-dependent resolution of 37 nm and a resolution of 98 nm when imaging UCNPs at a depth of 56 μm through MCF7 tumor spheroids, which have a significantly higher density and thus scattering coefficients than typical tissue models.^[120]

Camillis *et al.* also demonstrated multiplexed imaging in another super-resolution technique, super-linear excitation-emission microscopy (uSEE).^[24] This imaging technique was first reported by Denkova *et al.* in 2019, and relies on super-linear probes only being excited by the central, most intense portion of the excitation laser (Figure 2B). The primary advantage to uSEE microscopy is not needing additional modifications to a traditional confocal laser scanning microscope, or requiring exotic or complicated UCNP architectures (NaYF₄: 20% Yb, 8% Tm). After optimizing experimental conditions, the authors reported halving the resolution limit in a fixed cell sample.^[121]

Another common super-resolution technique that has been applied to UCNPs is structured illumination microscopy (SIM). SIM achieves super-resolution by using grates or filters to apply a patterned excitation to the sample. This pattern is then changed and applied to the sample again, and post-processing uses the multiple images to better identify the particle locations and reduce resolution limits.^[122] Figure 2C shows one application of upconversion nonlinear structured illumination microscopy (u-NSIM), which combines the super-resolution capabilities of SIM with the NIR-excitation property of Yb/Tm UCNPs to achieve a resolution of around 130 nm as well as clear resolution of 350 nm lines through a 51.5- μm thick section of liver tissue.^[42]

Multiplexing of imaging probes has further been realized through a similar SIM technique termed time-resolved structured illumination microscopy (TR-SIM), where altering the thickness of a migration layer separating the Nd³⁺sensitizer layer and the Yb³⁺ core can alter the lifetime curve of the UCNPs. Using this technique, the authors were able to have three separate subsets of

UCNPs that only varied by the size of their migration layer, and imaged these UCNPs with a single detector and single excitation laser while achieving a lateral resolution of 185 nm.^[25]

Other super resolution techniques have taken advantage of photon avalanche mechanisms in upconversion, where a nanoparticle material has significantly stronger absorption in an excited state as opposed to ground state energy levels. Upon initial excitation, ions can occupy an excited energy state, and through cross-relaxation then pair with a ground-state ion to create two intermediate-energy ions. Due to a high absorption at this intermediate excited state, these ions can then repeat this process, creating a large number of intermediate and excited-state ions, enabling a “photon avalanche” effect when falling back to ground state.^{[23], [123], [124]} Researchers have developed UCNPs with the capability of absorbing as many 80 photons in the multi-photon process, leading to a proportional reduction through the multi-photon process with resolving capabilities at distances as short as 20 nm.^[23] These photon avalanche, energy-looping UCNPs often use a non-resonant excitation through a 1,064-nm laser to target the excited state energy absorption in thulium ions.

Super-resolution technologies have been further used for UCNP characterization. Ren *et al.* use stochastic optical reconstruction microscopy (STORM), to distinguish 170-nm rod-shaped UCNPs with fluorescent probes solely on the ends of the nanoparticles or evenly distributed throughout the nanoparticle.^[125] STORM imaging excites a selection of optically-resolvable fluorophores in the sample of interest by using multiple lasers to cycle emission sources between light and dark states. By continuing to excite a fraction of total fluorophores through multiple images, emission overlap does not occur, allowing for a more exact location of emitted light to be determined.^[126]

A potential drawback to many of these super-resolution techniques is the laser power needed to achieve the best resolution. For example, NIRES imaging used a laser power of 4 MW/cm^2 and, in achieving 28 nm resolution through STED, excitation lasers at powers of 0.66 MW/cm^2 and suppressive lasers with power as high as 9.75 MW/cm^2 were used.^{[41], [118]} When using the Bessel beam for resolving particles in spheroids, 8.9 MW/cm^2 of laser power was necessary.^[120] For comparison, Liu *et al.* found that a 4 kW/cm^2 , 976-nm laser imaging through a $51.5\text{-}\mu\text{m}$ tissue slice resulted in a 3°C temperature increase in the sample.^[42] Other papers have noted that laser powers in this range are not feasible for live cell imaging experiments and laser powers at 1 kW/cm^2 may lead to photodamaged cells.^[88] Nevertheless, with regards to sample overheating, applying super-resolution techniques to imaging in cellular experiments will require more focus on reducing the laser power necessary to achieve super-resolution or using lower-laser power techniques such as u-NSIM alone combined with post-processing methods such as Hessian deconvolution or artificial intelligence.^{[127], [128], [129], [119]}

iv. Bioimaging of Upconversion Nanoparticles in Live Cells

In living cell microscopy experiments, the desirable characteristics of nanoparticle bioimaging probes include non-cytotoxic behavior, ability to image specific cellular compartments and organelles, and the ability to be used in tandem with other imaging probes. In this section, we explore UCNPs' ability to fulfill each of these characteristics and highlight recent advances in cellular imaging.

1. Cytotoxicity

Two primary means of cell death could occur in UCNP imaging experiments: first, extended NIR laser exposure may lead to a reduction in cell viability due to phototoxicity and overheating;^[130] and second, the UCNPs themselves could induce cytotoxicity. Most research shows minimal UCNP-induced cytotoxicity when dosed with relevant concentrations. For example, Zhang *et al.* found that in clusters of Tm³⁺ and Er³⁺ sensitized UCNPs, minimal cytotoxicity was observed in concentrations up to 500 µg/mL. Additionally, neither 980-nm nor 808-nm lasers with power densities of 2.5 Wcm⁻² for as long as 20 minutes caused a notable reduction in HeLa cell viability. However, at these levels, a nonsignificant downward trend between the controls, 10, and 20 minute timepoints may point to reaching an upper threshold of laser power for this experiment.^[67]

Other studies have found no toxicity in HeLa cells irradiated for three cycles of a 980-nm laser power on for five minutes and off for five minutes at laser powers up to 5.8 Wcm⁻².^[131] However, Levy *et al.* found HeLa cells did not experience ruptured membranes, indicating phototoxic cell death, when exposed to 1,064-nm excitation at 10⁶ Wcm⁻² for over two hours.^[123] Similar nanoparticles dosed in HeLa and Cal27 cells, show a slight downward trend in cell viability with

~80% viable cells after dosing with UCNPs at 1 mg/mL.^{[132], [133]} Numerous other studies engineered UCNPs for photodynamic therapy found minimal reduction upon dosage and a stronger reduction in cell viability following laser activation.^{[134], [135]}

A possible method to account for sample overheating in experiments is through the use of UCNPs capable of temperature sensing in physiological ranges through ratiometric sensing.^{[13], [136], [137]} Alternatively, a pulsed laser excitation as opposed to continuous-wave laser excitation was found to have a proportional impact on sample heating, meaning that using a 1:1 on/off pulsed laser would be expected to reduce sample heating by 50%.^[57] Increasing the time between image acquisition steps could be hypothesized to have similar effects. In whole body imaging, it has been shown that 808-nm lasers have lower effects on tissue overheating than 980-nm lasers while also showing significantly deeper tissue penetration.^[55]

2. Surface Modification

An ideal nanoparticle-based bioimaging probe can be modified to target and enable observation of specific intracellular organelles, proteins, DNA strands, or other areas of interest. Briefly, UCNPs have been coated with DNA strands,^[138] antibodies,^[139] amine groups,^[140] cell membranes,^[141] and ligands/polymers/surface charges^{[133],[142],[30],[143],[6]} among others, and have been engineered to be activatable for imaging or release of loaded molecules (Table 1).^[132] For example, using Nile red dye derivative-modified UCNPs, iron ions were able to be detected in cells at concentrations as low as 89.6 nM.^[144] Presumably, other metal ions of interest could be detected and quantified by similar strategies through finding dyes that selectively react with the targeted ion.

Dress *et al.* were able to use lanthanide resonance energy transfer (LRET), a technique where UCNP proximity is used to selectively excite a nearby luminophore, to visualize the interaction between two mitochondrial matrix proteins Tom20 and Tom7.^[145] Zhan *et al.* used STED to achieve super-resolution cytoskeleton images through conjugating a secondary antibody to their upconversion particles in HeLa cells.^[139] Through immunolabeling, UCNPs have been engineered to differentiate between cell types as well, enabling their use to be applicable in experiments requiring distinction between multiple cell types in heterogeneous cultures.^[146]

Nanoparticles are often labeled with external luminescent compounds to enable visualization in optical imaging. UCNPs exhibit intrinsic upconversion luminescence, i.e. the UCNP itself is the source of the luminescence signal. This characteristic is advantageous in comparison to fluorescently-tagged nanoparticles, where the fluorescent label could alter the surface chemistry of the nanoparticle and in turn alter the downstream nanoparticle-biology and nanoparticle-cell interactions.^{[147], [148]} Being the luminescent label themselves, UCNPs enable label-free nanoparticle tracking in comparison to other fluorescent tagging techniques and thus a wider range of experiments to be conducted.

3. Multiplexed Imaging

Multiplexing is an attractive feature of nanoparticles in cellular experiments. Ideally, the multiplexing nanoparticles would be physically and functionally identical within the cellular environment and only differ in their end target and their emission upon excitation, enabling single-laser excitation if necessary and preventing physicochemical differences between nanoparticles to alter cellular fate.^[75] As compared to fluorescent probes, which require multiple excitations, past work has shown that UCNPs can have tunable emission lifetimes through altering the size of

migration shells, customizable upconversion emission colors through altering laser pulse, or both occurring in the same particle.^{[64], [25], [56]} A summary of these techniques can be seen in Figure 3.

Figure 3A depicts a lifetime-based multiplexing technique where the thickness of an inert inner shell affects the time necessary for the excited outer shell electrons in the sensitizer to transfer energy to the activator, enabling differentiation of UCNPs by taking numerous images in succession and identifying which timeframes each UCNP appears in. An additional technique was developed to distinguish two nanoparticle populations using the doping concentration-dependent laser-power threshold of UCNP emissions. In this paper, Camillis et al. noted the highly-sloped linear relationship between the 455-nm emission in thulium-doped UCNPs and the excitation laser intensity. Exploiting this property, 8 and 16% thulium-doped UCNPs were distinguished from each other by isolating the 455-nm emission through an 808-nm co-excitation laser. To distinguish particles, images were taken with two different laser powers, one below the excitation detection threshold for the 16% particles, but high enough to view the 8% particles at ~10% of the maximum emission, and the other with sufficient laser power to view the 16% particles at ~10% emission and the 8% particles at maximum emission power (Figure 3B).^[24] A similar, single-excitation laser technique has been developed in thulium-doped UCNPs, where altering laser excitation power makes the 1%, 8%, or both sets of UCNPs visible.^[73]

Another promising multiplexing application involves frequency multiplexing. For example, two ytterbium-based UCNPs were made, one with a holmium activator and the other using erbium. When imaged, both particles were visible during 977-nm laser excitation, however co-excitation with a 790-nm laser selectively excited the erbium particles whereas co-excitation with a 750-nm selectively excited the holmium particles (Figure 3C).^[149]

A final potential multiplexing approach that has limited demonstration in current literature is activator-emission based multiplexing. Doping with different activator ions leads to different upconversion emission spectra, enabling engineering of UCNPs to have different emissions from a single excitation laser.^{[40], [150]} By imaging with detectors at each emission peak, the proportional intensities could be used to determine the identity of particles. By coating UCNPs with an identical NaYF₄ core, these particles would have identical surface chemistries and provide an additional avenue for multiplexing of UCNPs with a single-laser imaging setup. In addition to lifetime-multiplexing, this activator-based multiplexing technique has also been demonstrated *in vivo* to identify different nanoparticle populations or to differentiate tumor cell lines in mice.^{[146], [92]}

In summary, multiplexing techniques have been developed for single laser-single detector (lifetime), multi laser-single detector (frequency & excitation power), and single laser-multi detector (activator) imaging setups. These techniques have been employed in systems requiring multiplexing of two or three UCNPs populations. Future work may focus on increasing the number of distinguishable UCNPs populations or increasing the accuracy at which these populations can be distinguished. One potential avenue could be in a combination of multiplexing techniques. For example, Liu *et al.* developed seven UCNPs populations (τ^2 -1 to τ^2 -7) with increasing spectral lifetimes and achieved ~70% accuracy in distinguishing UCNPs populations, and 93% when using three populations. Most misidentifications in the seven-UCNPs population method occurred due to difficulty distinguishing particles with nearby spectral lifetimes (i.e. τ^2 -2 and τ^2 -1/ τ^2 -3).^[25] However, if combined with a frequency encoding method, where populations 1, 3, 5, & 7 were holmium-based UCNPs and populations 2, 4, & 6 were erbium-based UCNPs, the largest source of error could be eliminated, increasing the accuracy of identifying UCNPs.^[149] Alternatively, within cellular imaging, using UCNPs in conjunction with downconverting fluorescent probes to

stain the nucleus, cell membranes, or other cellular compartments of interest can reduce the number of multiplexed channels needed for an experiment.

4. Cellular Actions

In addition to targeting cellular structures and multiplexing, UCNPs have been engineered to enact cellular functions. One particularly interesting study found that by using azobenzene-based 808-nm laser-activated caps, a knockdown siRNA strand targeting a specific gene used to enhance therapeutic efficacy could be released on command from a UCNP cluster.^[132] Further developing this technique could lead to on-demand gene expression/inhibition or release of intracellular proteins in addition to the PDT effects explored in this study. Other gene editing approaches focused on using UCNPs and CRISPR-Cas9 to achieve spatiotemporally-activated gene editing *in vitro* and *in vivo*.^[20] Similarly, UCNPs with a mesoporous silica and amine shell were loaded with DNA to examine transfection and DNA delivery to primary rat heart cell lines.^[140]

The upconversion emissions of UCNPs has further been engineered to stimulate *in vivo* neural cells through the ChR2 receptor, triggering dopamine release, silencing seizures, or recalling memories.^[151] Similar results could be expected in cell culture experiments, and have been used specifically with neural cells to dictate neural differentiation of induced pluripotent stem cells *in vitro* utilizing an 808-nm laser-activated conformational change in the shell resulting in release of retinoic acid from the particle.^[152]

A sizable amount of nanoparticle research is focused on nanoparticle trafficking, or studying how nanoparticles are taken into cells, where they travel once inside cells, and the end fate of nanoparticles interacting with cells. Current methods to monitor nanoparticle trafficking in live cells oftentimes involve fluorescent tagging of the particles of interest or recent research has used

naked nanoparticles and reflected light to visualize cell-particle interactions.^[153] As stated previously, fluorescent surface modifications can alter the pathway a particle may take inside the cell when compared to the label-free particle.^[147] UCNPs circumvent this problem by their core being the source of luminescence, enabling the engineered surface chemistry to be responsible for the particles' cellular fate. To that aim, UCNPs, when combined with methods for inhibiting certain uptake pathways, have been used to determine how nanostructures interact with cellular membranes and enter cells.^[133] Additionally, upon entering the cellular environment, Wang *et al.* developed a technique to track and map the movements of individual 40-nm UCNPs as they move through the cell over the course of multiple minutes.^[73] Combining these technologies with UCNPs coated with silica, lipid membranes or gold could result in particles with identical surface properties to current gold, silica, or lipid nanoparticles with upconversion luminescence capabilities enabling long-term uptake and trafficking observation.^{[154], [155], [156], [99]}

v. **Bioimaging of Upconversion Nanoparticles in Whole Animals**

Contrast agents based on UCNPs for animal-level imaging experiments should exhibit desirable characteristics such as biocompatibility, detection through applicable tissue depths, prolonged circulation times in the bloodstream, and not produce body-level toxicity or other cytotoxic effects. Additionally, being modifiable to target specific organs, tumors, or tissues, UCNPs would enable a wider range of applications including assisted surgery and/or targeted therapies. On this level, much research has been conducted to engineer UCNPs better suited to fit these criteria. A summary of selected publications regarding whole-body and tissue imaging of UCNPs can be found in Table 1. The table explains the architecture, application, excitation, and upconversion emissions of the UCNPs use in the corresponding publications involving tissue/whole body imaging whereas the imaging depth reported may be from a different portion of the corresponding publication if the authors specifically investigated the depth at which their UCNPs were visible. Table 1 provides a representative, non-exhaustive list of UCNP bioimaging applications in tissues and *in vivo* applications sorted by the aim of the paper and, to increase ease of organization, nanoparticle size. Papers falling under multiple table categories are listed in each applicable section.

1. Biocompatibility and Biodistribution

With regards to biocompatibility, poly(ethylene) glycol is a common UCNP, and general nanoparticle surface modification for extending circulation times of nanoparticles *in vivo* by reducing adsorption of unwanted proteins and lowering interactions of PEGylated nanomaterials with organs and cells of the mononuclear phagocyte system .^{[157], [158], [159]} However, recent studies have shown the potential for PEG coatings to cause unwanted immune side effects. As the details

of PEG-mediated toxicity are outside the scope of this paper, the authors recommend a review that was recently published by our research group covering PEG-mediated nanoparticle toxicity and other potential toxic effects of nanoparticles in animals and humans.^[160]

Alternative surface coatings that have been reported include colominic acid, which was demonstrated to have a three times longer circulation time than PEG-particles; or heparosan, a nonimmunogenic natural polysaccharide shown to reduce protein adsorption as efficiently as PEG; or through modifying UCNP surfaces with DNA or proteins.^{[161], [162], [163]} An additional method to avoid immunologic side effects involves red-blood cell membrane-coated UCNPs, which were found to allow “virtually no proteins” to adsorb to the surface of the particles.^[29] Other work has successfully coated nanoparticles with cancer cell membrane proteins to achieve similar results.^{[164], [141]}

For imaging applications, ideally the UCNPs would be eliminated from the body system following use, and organ distribution would be predictable and well-documented.^[165] A prominent advancement towards these aims was published by Peng *et al.* in 2020 where UCNPs with a potassium heptafluozirconate core, viewable 7 mm beneath a mouse’s skin at 1 Wcm⁻² excitation power, were engineered to be biodegradable in aqueous solutions, showing total loss of luminescence signal and clearance from the body within 6 hours, and showing a reduced degradation rate in the mildly acidic tumor microenvironment.^[166] A few key studies have further investigated the pharmacokinetics and biodistribution of UCNPs following administration in mice. In one study, UCNP-maleic anhydride/1-octadecene copolymer- HER2 targeting molecule nanoparticles were injected at a dose of 12.5 µg/g, and showed a substantial, ~20% reduction in circulating concentration between 2- and 5-minutes following injection. The authors noted little to no accumulation in skin or muscles with most accumulation occurring in the liver and spleen and

a relatively low amount of UCNPs in the kidneys. Finally, the authors noted no adverse effects experienced by the mice aside from a brief, slight decrease in total leukocyte count.^[167]

Another study orally fed mice NaGdF₄: 18% Yb/2% Er UCNPs coated with PEG and imaged upconversion luminescence intensity for the mices' stomach, large intestine, small intestine, heart, lungs, liver, and kidney and did not find a noticeable signal outside of the digestive tract. The UCNPs remained in the digestive tract for as long as 5 days following dosage of 500 µg/g.^[168] Presumably, this is due to the UCNPs never leaving the digestive tract, and was supported by findings showing that even 5-nm UCNPs were unable to escape the digestive tract and enter the bloodstream or surrounding tissue.^[168] A few other studies that evaluated biodistribution of UCNPs are available in the literature.^{[131], [141], [159], [169]}

2. Imaging Depth

An additional constraint for bioimaging experiments involving UCNPs is the need for light to penetrate the body deep enough to activate the particles, as well as the light emitted from the particles to be detectable. Table 1 lists imaging depths for a recent selection of *in vivo* bioimaging experiments. Notably, typical laser powers for these experiments range from ~100 mWcm⁻² – 10 Wcm⁻² and can image large numbers of UCNPs at maximum depths of approximately 1 cm below the surface of the mouse skin. Ideally, upconversion luminescence imaging experiments should be able to image UCNPs at applicable depths, using laser powers deemed safe for dermal exposure, or 0.73 Wcm⁻² for a 980-nm laser according to the American National Standards Institute.^[170] An important clarification to make here is, with regards to these *in vivo* bioimaging experiments, the imaging completed is most always not resolving individual UCNPs at the listed depth, but instead locating UCNP ensembles in the body. It should further be noted however, that at a whole body

level, resolving individual UCNPs may be less important than during *in vitro* studies. For example, brain vasculature was accurately mapped at 400 μm through mouse brain tissue using a 980-nm 1 μm -diameter excitation laser with power of 1.7 mW, which was noted to be 800,000x lower than the power needed to activate and image FITC, a common fluorescent dye, at the same depth. This study did not track individual UCNP movement as opposed to observing upconversion luminescence throughout the vasculature during imaging as a result of the presence of large quantities of UCNPs.^[69]

Analogous studies aiming to map mouse brain vasculature used 980-nm laser excitation with a laser power of 20 mW to reach imaging depths of 1 mm when combined with post-image deconvolution methods.^[129] To increase imaging depth in these experiments, one possible strategy would be focusing on tuning emissions to be in the NIR-I (700-1,000 nm), NIR-II (1,000-1,350 nm) or NIR-III (1,550-1,870 nm) optical windows through NIR-NIR imaging, as the upconversion emission light is also subject to tissue attenuation.^[171] This approach has been shown by multiple studies, which have found detection depths of UCNPs for 800-nm, 660-nm, and 540-nm emissions to be 8 and 7.7, 4 and 5, and 2 and 2.3 mm respectively.^{[138], [169]} This result indicates that longer wavelengths cannot only penetrate deeper into tissue, but by using NIR-NIR excitation/emission, upconversion emission signal may also provide visualization of UCNPs further from the surface.

Another simple modification to make, although using a lower wavelength laser may reduce the feasibility of NIR-NIR imaging, is using an 800-nm or 808-nm excitation laser instead of a 980-nm laser. This benefit is typically attributed to the $\sim 10\text{x}$ higher absorbance of Nd^{3+} at 808 nm than Yb^{3+} at 980 nm and the $\sim 25\text{x}$ higher absorbance of 980-nm light than 808-nm light in water. However, it is worth noting that tissue exhibits an increase in light scattering when moving from 980 to 808 nm.^[172] In the study, Wiesholler et al. highlighted the increased performance of 808-

nm excitation at deeper wavelengths but noted the significant impact of closely matching excitation lasers and absorption spectra for optimal imaging depth, noting a ~2.5-fold increase in photon absorption with their Nd³⁺ UCNPs when switching from an 805-nm to a 794-nm excitation laser.^[172] Liu *et al.* conducted experiments on the comparable performance of 800-nm and 980-nm excitation lasers and found that, through raw chicken, the 980-nm laser was able to be detected 0.2 cm beneath the surface, whereas the 800-nm laser was able to be detected 2.5 cm beneath the tissue surface, both at laser power of 0.5 Wcm⁻². Additionally, the 808-nm laser showed lower tissue overheating than the 980-nm laser.^[55]

Although less frequently, excitation lasers with wavelengths longer than 1,000-nm have been investigated for their utility in bioimaging of UCNPs containing a wide range of lanthanide ions.^[38] Of potential interest are data reported by Wang *et al.* showing a 7.1- and 2.1-fold enhancement in imaging spatial resolution through a 3.5-mm tissue phantom for a 1,550-nm excitation laser when compared to 1,064-nm and 1,344-nm lasers, respectively.^[173] Nevertheless, potentially the greatest room for improvement with regards to imaging depth is an increase in UCNP quantum yield. As quantum yield is defined as the ratio of absorbed to emitted photons, a quantum yield increase would lead to stronger emissions from identical non-toxic excitation powers, increasing the amount of tissue through which the particles could be detected.^[174] For example, the UCNPs used by Liu *et al.* to achieve detectable upconversion luminescence at a depth of 2.5 cm had a reported relatively low quantum yield of 0.75%.^[55]

Other techniques and results used to increase imaging depth include (i) an ~3x increase in penetration depth when increasing 808-nm laser pulse frequency from 500 Hz to 71.4 MHz;^[175] (ii) an increase in signal-noise ratio through use of highly doped (60% sensitizer / 40% activator) UCNPs as opposed to UCNPs with a more common, i.e. lower lanthanide ion dopant concentration

of 20% sensitizer and 2% activator;^[170] (iii) a 3% increase in light intensity at 5 mm tissue depth using a high-frequency ultrasound to reduce scattering of light through the tissue;^[176] (iv) or increasing the beam width of excitation lasers, where the increase from 1 to 10 mm lead to a penetration increase of nearly 100% before further plateauing beyond 10 mm.^[44]

Applications that focus less on imaging and more on enacting photo-effects on nanoparticles *in vivo*, such as photodynamic therapy (PDT), or light-based activation of a desired effect, also focus on measuring penetration depth, but focus less on emission detection. For example, Chen et al. showed UCNPs emitting blue light had the capability of activating neurons at depths of up to 4.5 mm using a 2-W 980-nm laser and a calculated quantum yield of 2.5%.^[151] The same study modeled both laser excitation and upconversion emission intensity at different depths through the brain tissue.^[151] One PDT application noted 60-70% death of targeted cells at a depth of 1 cm by using NIR-stimulated upconversion emission from UCNPs to activate KillerRed, a green-light excited ROS generator.^[177] Other UCNP-based PDT applications are summarized in Table 1.

3. *In Vivo* Targeting

As shown previously, UCNPs have been engineered with surface modifications ranging from antibodies for immune-targeting to specific functional groups, as well as tailoring UCNP surface charge for specific applications. These surface modifications have been applied to multiple *in vivo* targeting applications in both systematic and locally-injected UCNPs. Micelles engineered with antibodies targeting a common membrane protein of pancreatic cancer cells were engineered and found to have an elevated targeting efficacy compared to non-targeted UCNPs.^[159] Seok *et al.* conjugated a breast cancer-specific antibody and colon cancer-specific peptide to two UCNP types with identical excitations but distinguishable upconversion emission wavelengths to successfully

identify the location of two separate cancer types in systemically administered UCNPs showing 3-fold increase in accumulation when compared to bare UCNPs.^[146]

UCNPs administered *in vivo* have successfully passed the blood-brain-barrier and delivered anti-cancerous effects to glioblastoma cells through angiopep-2, increasing the median survival time of the mouse treatment group against the control.^[178] Further research used a similar approach, but added an 808-nm induced generation of reactive oxygen, enabling on-demand endolysosomal escape of UCNPs in glioblastoma cells.^[54] Additionally, folic acid conjugated UCNPs were found to enhance targeting capabilities against breast cancer tumors grafted into mice.^[29] Other strategies involved targeting specific miRNA sequences *in vivo* for targeting of cancer cells, potentially leading to an expansion of targeting abilities for cancers or diseases with difficult to target or currently unknown protein elements.^[43]

The primary concern with enhanced targeting of tumors, organs, or biomolecules in whole body systems is a moderately low increase in upconversion signal in these studies between the targeted molecules and the control, with results rarely showing more than a 5-fold increase, and usually, as in the case of the folic acid conjugation, showing an approximate 3x increase in targeting efficiency between the non-targeting and targeted particles.^[29] This is a common issue faced in nanoparticle targeting, specifically within tumor targeting, as a median value of only 0.7% of injected nanoparticles reaching tumors and cancer cells is expected.^{[179],[180],[181],[182]} Regarding UCNPs, methods of increasing delivery efficacy developed in other nanoparticle applications can be applied to upconversion nanoparticles as well. A more in-depth review of nanoparticle-tumor delivery strategies was recently published by Sheth *et al.*^[183]

vi. Applications of Upconversion Nanoparticles in Multimodal Bioimaging

Long-term goals for the field of upconversion luminescence bioimaging may include translating the method into clinical settings. One potential application could be in imaging-guided surgery. UCNPs provide real-time signal and can be designed to have upconversion emissions strong enough to be visible with the naked eye.^[97] This study by Shen et al. achieved naked-eye visible UCNPs for surgical resection through a 15x increase in upconversion luminescence intensity by doping the CaF₂ based UCNPs with a high concentration (98%) of Yb³⁺ sensitizer ions. As opposed to repeatedly referring to ultrasound or MRI screens, upconversion light emission from targeted tissue could lead to an improvement in surgical accuracy and operating time.

UCNPs could further open new opportunities in clinical imaging that are currently unachievable with techniques including X-ray, MRI, PET, and ultrasound. A few examples of these new avenues include (i) the potential for molecular and protein targeting; (ii) instant, visual feedback of optical signal; and (iii) the possibility of multimodal bioimaging. Multimodal bioimaging involves the combination of UCNP imaging and other clinical imaging techniques. With slight modifications, UCNP activity and localization can be visualized with X-ray/computed tomography (CT), photoacoustic imaging (PAI), magnetic resonance imaging (MRI), and single-photon emission computed tomography (SPECT). Examples of each of these applications and sample images are shown in Figure 4.

A few examples of different UCNPs types used in X-ray/CT imaging include BiF₃: 20% Yb³⁺/2% Er³⁺ (Figure 4 bottom right),^[63] NaGdF₄: 18% Yb³⁺/2% Er³⁺,^[168] ¹²⁵I-labeled NaYF₄:Yb³⁺/Er³⁺,^[158] and NaYF₄:Yb/Tm with a NaGdF₄:Yb shell functionalized with cyanamide and gold nanocrystals,^[131] among others. CT values have been found to increase linearly as a function of UCNP concentration enabling at least semi-quantitative signal.^[131] Similar linear

relationships between localized UCNP and gadolinium ion concentration and signal intensity exist in magnetic resonance (MR) imaging.^{[55], [184], [185]} With regards to MRI, a number of published studies use gadolinium ions dopants as the MRI-sensitive portion of the UCNPs. Although yttrium ions may be suitable for MR imaging, gadolinium is commonly used in MR imaging making gadolinium-based UCNPs an attractive contrast agent for MR-UCL bimodal imaging.^[186] For a proof-of-concept, the top right corner of Figure 4 shows elevated signal strength in a mouse abdominal tumor following injection of UCNPs with a gadolinium-based shell. Liu *et al.* used direct intratumoral injection of gadolinium-based UCNPs to show *in vivo* contrast enhancement of MR signal in a mouse liver.^[55] Additional research used gadolinium-doped UCNPs combined with a red blood cell membrane coating and folic acid ligands to enhance nanoparticle localization to breast cancer tumor-grafted mice.^[185] Further studies used a gadolinium-based UCNP core and peptide ligands to monitor accumulating nanoparticles in HCT 116 colon cancer cells.^[99] One potential drawback in MRI-UCNP bimodal imaging could be in the extent of nanoparticle delivery efficiency, as most *in vitro* UCNP-MRI experiments showed limits of UCNP detection when gadolinium concentrations were in the single μM range.^{[187], [184]} Additionally, research into erbium-based UCNPs showed a reduction in upconversion luminescence intensity with gadolinium instead of yttrium particle cores, which could hinder UCL/MR multimodal imaging.^[100] However, because the increasing magnetic field strength currently used in MRI is safe to use in humans, and able to increase signal-noise ratio, future developments will provide lower limits of detection in *in vivo* applications.^[188]

Another prevalent pair of imaging techniques are PET and SPECT. A sample SPECT image of radiolabeled UCNPs can be found in the top left corner of Figure 4. UCNP experiments designed for PET/SPECT imaging have further been used in UCL, MRI, and photoacoustic imaging.^[31]

However, the key difference between PET/SPECT and other imaging modalities previously discussed is PET/SPECT requires the attachment of a radioactive tracer in order to visualize uptake of molecules of interest into tissue, which may take additional preparation, but enables more accurate quantification of nanoparticles, especially in organs located deep inside the body.^[189] For example, Kostiv *et al.* published two papers on multimodal imaging with ¹²⁵I-labeled NaGdF₄ core nanoparticles and used a neridronate linker to attach ¹²⁵I to the UCNPs. These PEG-labeled UCNPs enabled unmodified trimodal imaging of CT, SPECT, & MRI, and monitoring of UCNP biodistribution for up to 14 days following injection in mice.^{[158], [187]}

Whereas UCNP-radiolabeling techniques may alter surface chemistry and in turn, cellular interactions, one study developed a technique involving a two-part dosing process, where the initial red blood cell membrane-coated particles are first dosed into the mouse followed by a dose of fluorine-18 engineered to selectively bind the particles *in vivo* through a click chemistry process.^[185] This approach allowed for cellular uptake and biodistribution as well as UCL/MR imaging to occur before radiotracers entered the system, which may better portray the expected activity of the UCNPs *in vivo*.

Finally, UCNPs show potential utility in photoacoustic imaging (PAI). PAI is based on the photoacoustic effect, where nanosecond pulsed light absorption results in the formation of sound waves from the area of interest, which are detectable and able to be mapped into an image as seen in the bottom left corner of Figure 4. PAI's main advantage as opposed to other optical imaging techniques is the reduction in optical scattering of emission signal, enabling higher resolution in relatively deep biological tissue.^[190] One potential application of PAI in multimodal UCNP imaging was shown by observing tumor angiogenesis and UCNP accumulation over a period of time through PAI and observing full-body distribution using upconversion luminescence

imaging.^[55] Another notable advancement in the field was realized by Wang *et al.* where UCNP excitation by an 800-nm laser was used to excite fluorescent dyes through tissue to use PAI instead of upconversion luminescence imaging of dyes in solution. This approach, combined with UCNP emission tuning through excitation laser modulation could lead to multiple fluorescent probes being imaged through depths >1 cm.^[191]

With regards to photodynamic therapy, PAI has been developed to monitor localization as well as deliver indocyanine green dye to cells, effectively reducing viability.^[192] Additionally, UCNPs engineered to be injected in microbubbles were found to release compounds of interest upon exposure to ultrasonic waves, and in-turn inducing cytotoxicity following confirmed accumulation in the tissue of interest.^[193] Through a similar technique, PAI could be used to achieve a targeted therapeutic effect. Other research has used azobenzene-polymers to enhance PAI contrast, and then use PAI UCNPs for detection and diagnosis of deep tissue diseases before using the more rapid feedback of NIR-II emissions from the same UCNPs in order to provide accurate surgical guidance during operation.^[194] Additional research has combined UCNPs with PAI to monitor the concentration of peroxynitrite, a biomarker for hepatotoxicity to noninvasively monitor drug-induced liver damage in mice.^[195]

vii. Limitations in Advancement of Upconversion Nanoparticle Bioimaging

UCNPs exhibit the primary advantage of NIR excitation and the emission of light with relatively shorter wavelength than the excitation light. Applications of UCNPs in cellular imaging have established methods for these nanoparticles to exhibit multiplexing capabilities that enable the real-time spatiotemporal tracking of UCNPs through cellular environments. However, a limitation in these live cell experiments is in the ability of achieving super-resolution imaging in living cells while still resolving individual UCNPs from other agents or fluorescent dyes used in tandem without exposure to laser powers strong enough to alter cellular function or kill cells. Efforts to reduce the necessary excitation power densities may enable super-resolution imaging of single UCNPs in intact live cells without affecting the biological functions of the cells.

At the whole tissue and whole animal levels, the primary hurdle for optical imaging is penetration depth of light signal due to light extinction. More effective UCNP technologies may enable more accurate non-invasive imaging with better spatiotemporal resolution in smaller, deeper organs or tissues of interest. Furthermore, targeting capabilities have shown relatively low nanoparticle delivery efficiencies in theranostic UCNP doses to specific organs and tissues in mice. Designing UCNPs with more effective tissue and cell targeting efficiencies could substantially advance the UCNP bioimaging capabilities.

With the ultimate goal of translating UCNPs technologies into safe and effective real-world applications and clinical use, additional studies are needed to further assess the fate of administered UCNPs in the body. More comprehensive toxicological studies are needed to evaluate how UCNPs degrade in the body or how these nanoparticles are excreted and eliminated from the body to facilitate the development and clinical translation of UCNP-based imaging technologies.

viii. Conclusions

UCNPs show promise in bioimaging applications. UCNPs have been used in numerous cellular imaging experiments, not only due to inherent utility for upconversion luminescence-based visualization, but further in creating desired cellular actions upon excitation light activation. Super-resolution imaging of individual UCNPs have been demonstrated in the recent literature to track the spatiotemporal distribution. UCNPs are uniquely positioned to enable targeted theranostic functions due to their ability to enact light-dependent localized effects. Potential clinical applications highlight the use of UCNPs for multimodal bioimaging including combinations of X-ray, PET/SPECT, PAI and MRI applications. Further research in the combinations of these bioimaging methods will enable single particle-type combinations of deep tissue imaging and increasingly targeted therapeutics as well as disease diagnosis and surgical guidance among other applications.

c. Live Cell Nanoparticle Uptake Imaging

ii. Light Scattering Imaging

As previously discussed, UCNPs are widely tailorable to specific applications and can easily be imaged with low background noise due to upconversion properties. This enables their use in *in vitro* cell imaging in both living and fixed cells. However, synthesis of lanthanide UCNPs oftentimes requires the use of hazardous and non-ecofriendly chemicals such as 1-octadecene, and lanthanide salts.^[196] In addition, they require relatively laborious synthesis processes, inert gas conditions, and relatively expensive reagents.^{[197], [198]} In contrast, gold nanoparticles are easily synthesized with readily available, relatively low-cost reagents and thus are widely used in nanoparticle research.^[199] Gold nanoparticles have wide arrays of potential surface coatings and could be engineered to match the surface chemistry of any UCNP in a bioimaging experiment.^[200] Because of this, the development of bioimaging techniques where gold nanoparticles have comparable optical capabilities to UCNPs would enable similar *in vitro* bioimaging experiments to be conducted at lower cost and using green chemistry principles, such as using less hazardous chemicals, and preventing waste.^[201] Towards this aim, Kim and colleagues developed a label-free imaging technique using optical diffraction tomography (ODT), exploiting the difference between the refractive indices of gold nanoparticles and cell cytoplasm to locate gold nanoparticles and distinguish single particles from aggregated particles.^[202] Other approaches utilized multiphoton intravital microscopy, taking advantage of a gold nanoparticle's multiphoton absorption-induced luminescence to visualize nanoparticles following vascular injection.^[203] Using a standard confocal microscope, Wang et al. reported a technique where excitation light reflected off nanoparticles can be detected to visualize the interactions of silver nanoparticles with cells in real time.^[204] Utilization of a standard confocal

microscope avoids the added costs of a multiphoton imaging setup and can take advantages of the relatively widespread use of confocal microscopy as compared to holographic microscopy techniques used in ODT.

iii. Endocytosis Pathways

Realization of this technique will aid in the study of how nanoparticles interact and are endocytosed into cells with application in targeted drug delivery and cancer research.^{[205], [206]} Nanoparticles are endocytosed into cells through three primary pathways: clathrin-mediated endocytosis, caveolae-mediated endocytosis, and macropinocytosis. Each of these mechanisms is well described in a work recently published by Sheth et al.^[183] Briefly, clathrin-mediated endocytosis involves vesicles coated with clathrin protein and typically are in the size range of ~100 nm. An in depth review on clathrin-mediated endocytosis and related proteins, assembly, and mechanisms was recently published by Kaksonen et al.^[207] Caveolae-mediated endocytosis involves vesicles coated with the caveolin protein as well as cholesterol and sphingolipids. These vesicles have similar size and invagination processes as clathrin-mediated endocytosis.^[183] As caveolae-mediated endocytosis plays a lesser role regarding nanoparticle uptake in macrophage lines, this pathway was not a primary focus in this experiment.^[208] Macropinocytosis is the third of the three major uptake pathways discussed here. Different from caveolae and clathrin-mediated endocytosis, macropinocytosis involves cell membranes non-specifically engulfing large portions of extracellular molecules in vesicles ranging from 500-2,500 nm.^[183] Macropinocytosis was first identified in macrophage cell lines and occurs in these cells at a significant rate, however, the specific methods by which this occurs appears to vary between macrophages, dendritic cells, and other immune cells.^[209] Additionally, with regards to cancer

treatment, cancer cells are often associated with increased rates of macropinocytosis.^[210] Further regarding drug delivery and cancer therapy, a nanoparticle's uptake pathway influences the particle's end fate within the cell.^{[211], [212]} A few examples of these end fates include transcytosis: releasing particles on the opposite side of the cell with application in blood-brain barrier transport as well as other epithelial barriers;^[213] endosomal escape: releasing nanoparticles inside the cell, which has been shown to be the rate determining step in therapeutic delivery;^[214] or delivery to intracellular lysosomes. In brief, uptake pathways are highly influential in determining a particle's effect at the cellular and subcellular levels and understanding them is critical for effective nanoscale engineering.^[215] Developing methods to target and understand specific cellular uptake pathways of targeted therapeutics could lead to engineering more efficient delivery techniques in nanoparticle research.

iv. Heparosan Gold Nanoparticle Model System

Heparosan is a natural polysaccharide investigated by recent research as a nonimmunogenic surface coating for injected nanoparticles.^[163] As explained previously, poly(ethylene glycol) has been identified as a potential cause of adverse immune effects in injected nanoparticles, but is commonly used to prevent *in vivo* protein adsorption onto nanoparticles and maintain the particles' engineered structure and function. As a model system, heparosan was selected as it was found to have significant uptake in immune cell lines.^[163] Significant uptake enables a more rapid experiment and validation of this live cell technique through 1 hour uptake experiments as opposed to multiple hour uptake experiments. Furthermore, identifying immune cell lines with notable rates of macropinocytosis as a model system enables a multi-pathway endocytosis study. By using the RAW 264.7 macrophage and heparosan-coated gold nanoparticle system, live cell

uptake quantification was able to be developed in a relatively short period of time and uptake data could potentially be applied to other studies within the scope of our group's research.

v. Project Introduction and Goals

This work serves to apply the same light scattering imaging technique described by Wang et al. to gold nanoparticles in living cells. The first chapter will detect gold nanoparticles as small as 15 nm and establish the size-dependent intensity and area of light scattering in gold nanoparticle imaging. Secondly, gold nanoparticles will be shown to have superior photostability capabilities to fluorescent tagging of nanoparticles, enabling the long-term imaging abilities required for live cell uptake studies. Third, light scattering of nanoparticles in living cells will be demonstrated and optimized. Fourth, fixed cell uptake studies in a heparosan-gold nanoparticle model will be used to identify an ideal time frame for live cell studies. Finally, gold nanoparticle uptake following inhibition of uptake pathways will be monitored to identify the role each uptake pathway plays in endocytosis of heparosan-coated gold nanoparticles.

2. Materials and Methods

a. Gold Nanoparticle Synthesis and Characterization

Prior to synthesis, to prevent contamination and enhance monodispersity of colloidal gold, flasks were first cleaned with aqua regia, using a 3:1 ratio of hydrochloric acid (Sigma-Aldrich, ACS reagent, 37%) to nitric acid (Sigma-Aldrich, ACS reagent, 70%). The acid was left in flasks until a deep orange color was visible, then flasks were rinsed thrice with nanopure water, then 15 times following addition of a drop of dish soap and dried before deemed acceptable to use. All water used was nanopure ($>18.2\text{M}\Omega\text{-cm}$, Reppile Purist) water stored and transported in plastic vials to prevent contamination.

The gold synthesis occurred in two steps: synthesis of 15 nm seeds, then controlled growth of particles to sizes ranging from 30 nm-200 nm. Synthesis of 15 nm seeds occurred based on citrate reduction published by Turkevich et al.^[216] To a cleaned flask, 98.9 mL of water was mixed with 1mL of 30 mg/mL tribasic sodium citrate dihydrate (Sigma-Aldrich) and stirred at 200 rpm on a hot plate set at 300 °C. Upon boiling, the stir rate was increased to 400 rpm and 100 μL of 98.5 mg/mL (250 mM) gold (III) chloride trihydrate (Sigma-Aldrich) was quickly added and the reaction was allowed to proceed for 7 minutes covered with aluminum foil before the flask was cooled to room temperature on a tray of ice. The particles were measured by DLS (Malvern Zetasizer) to determine size and absorbance spectra were measured by a UV-Vis spectrophotometer (Agilent Technologies Cary Series) to determine concentration. Here, 100 μL Tween20 (Sigma-Aldrich, Molecular Biology Grade) if larger particles were not being made. The particles were centrifuged at 15,000 $\times g$ for 90 minutes and washed in 0.01% Tween20 + 0.01% tribasic sodium citrate solution twice before final concentrations were measured.

For synthesis of larger particles, reagents from Table 2 were added to cold nanopure water under vigorous stirring (>400 rpm) in the following order: gold chloride solution, tribasic sodium citrate solution, 15 nm gold nanoparticle seeds, and hydroquinone solution (Sigma-Aldrich). The flask opening was covered with aluminum foil and the growth process proceeded for >8 hours at room temperature. Each population's size and concentration were determined by DLS and UV-Vis respectively before centrifugation 3 times at the corresponding speed listed in Table 2 and being resuspended in 0.1% Tween20 + 0.01% sodium citrate tribasic solution. To ensure monodispersity of particles, DLS measurements required a 15-measurement average polydispersity index (PDI) reading of <0.1 to be suitable for further experimentation. The calculation for PDI is displayed below:

$$PDI = (\sigma/d)^2 \quad (1)$$

Where σ is the standard deviation of particle size and d is the mean particle diameter.^[217] Results of final nanoparticle population size and PDI measurements are shown in Table 3.

Transmission electron microscopy (TEM) measurements of particles provide a more accurate measurement of particle size due to DLS measuring hydrodynamic diameter, which is sensitive to the surface coatings of Tween20 and citrate used in the synthesis process. Copper TEM grids (Ted Pella Inc.) were plasma cleaned (Harrick Plasma Plasma Cleaner PDC-32G) to create a hydrophilic surface to allow for enhanced coating of gold nanoparticles. Following cleaning, 3 μ L of nanoparticle sample were drop-cast onto each grid and left to dry. To reduce imaging time, 15 & 80 nm, 30 & 150 nm, and 45 & 200 nm particles were dried onto the same slides and distinguished in image analysis. The 60 nm particles were alone on the fourth slide. Image analysis was performed by ImageJ. Briefly, .tiff images were converted to 16-bit images in ImageJ, the scale was set, the Huang threshold was applied, and then the analyze particles function was used and set

to select particles with areas +/- 50% of the expected area to prevent selection of the smaller or larger particles on the same image. Edge particles were excluded and any holes in the middle of particles were assumed to be image artefacts and counted as area. ImageJ provided an average area of the >12 particles analyzed, and spherical particles were assumed to convert two-dimensional area to particle diameter.

b. PEGylation of Gold Nanoparticles

To prevent particle aggregation upon exposure to solutions with higher ionic strengths, thiolated polyethylene glycol (PEG) was used to coat nanoparticles. Briefly, PEG was suspended in water at a concentration of 1 mM then diluted to the proper concentration for particle populations to have 5 PEG molecules/nm² of gold in solution. This concentration was calculated using particle concentration, diameter, and assuming spherical particles. The binding process was allowed to proceed for 30 minutes before removing excess PEG through two 30-minute centrifuges at the speeds listed in Table 2. PEGylation was confirmed through an increase in hydrodynamic size following centrifugation.

c. Creation of Gold Nanoparticle Polyacrylamide Gels

Polyacrylamide gel particle suspensions were used to visualize nanoparticle size in confocal light scattering imaging. The following reagents diluted in water unless otherwise noted, were added to a final volume of 7 mL: 0.75 g acrylamide, 0.045 g bisacrylamide, 1.17 g sodium chloride, and 1 mL 10x PBS. In a 1.5 mL centrifuge tube, 470 μ L of gel solution was mixed with 10 μ L of 40 pM gold nanoparticles, or the maximum possible concentration, of varying sizes before adding 10 μ L of TEMED and 10 μ L of 10% ammonium persulfate to initiate the reaction. The solution

was quickly vortexed and injected between two #1.5 glass cover slides with a custom 3D printed spacer to allow space for the gel to solidify. Samples were stored at 4 °C wrapped in foil until imaging.

d. Confocal Imaging of Polyacrylamide Gels

Images were taken using an upright Leica SP8 confocal microscope with a HC PL APO CS2 63x/1.4 oil objective. The incident laser was a 561 nm laser with an intensity of 2% and gain of 464.5. A RT 15/85 excitation beam splitter was used, and the detector was set from 556-567 nm and the pinhole was set to 1 airy unit. Because glass cover slips increased background noise, the top cover slip's z-position was first located before adjusting the focus into the gel away from the cover slip until the background noise was no longer visible, and a 20+/- 1 μm section was split into 67+/- 1 sections and imaged with a scan speed of 600 Hz. The files were saved, and the max projections of the z-plane images were utilized for analysis. Analysis was completed by a similar technique described in the analysis of the TEM images.

e. Preparation of Cy5-Labeled Gold Nanoparticles

To prepare Cy5-labeled gold nanoparticles for the photostability study, 19.2 μL of 100 mg/mL thiolated 5 kDa amine-terminal PEG (Laysan Bio) was oxidized with half a molar equivalent of sodium tetrathionate dihydrate (Acros Organics) in a total volume of 48.6 μL 0.1 M pH 8 sodium bicarbonate buffer and incubated at room temperature for one hour. This solution was then dialyzed (0.1mL Pierce Slide-A-Lyzer™ MINI Dialysis Device 3.5 kDa MWCO) against 200 mL of sodium bicarbonate buffer on a stir plate (IKE C-MAG HS 7) at a setting of 0.5 for one hour at room temperature. The solution was then pH adjusted to 8 and 2 molar equivalents of NHS-Cy5

dye (Sigma-Aldrich) as added to the dialyzed solution, then wrapped in aluminum foil and vortexed for three hours at room temperature. 100 PEG-molar equivalents of dithiothreitol (Sigma-Aldrich) was then added to the solution and incubated for one hour at room temperature to reduce the thiol bonds. This solution was then passed through a NAP-25 column (Sephadex G25 GE Healthcare) equilibrated with 0.1 M pH 8 sodium bicarbonate buffer. The collected sample was then dialyzed overnight at 40C against nanopure water. To determine purity and success of synthesis, a 0.5% agarose gel was ran on the impure fraction, the pure fraction, the final flowthrough, and a previous stock of Cy5-PEG and the results are shown below. Briefly, 0.375g of agarose powder (Fisher BioReagents) was dissolved in 75 mL of 10x tris-borate-EDTA buffer (Sigma-Aldrich) diluted 1:20 in water using a microwave and then allowed to solidify before each 3 μ L sample was mixed with 2 μ L 150 mg/mL Ficoll 400 solution (Sigma-Aldrich) to properly sit in the gel and ran at 50 V for 30 minutes, or until proper separation was achieved, (VWR Mini Gel II) and the visible light or Cy5 emission was imaged using an Azure C600 system. The results are shown in Figure 5. To coat Cy5-PEG onto gold nanoparticles, a similar procedure to the PEGylation procedure previously described was used. To confirm fluorescent labeling of particles, another agarose gel was ran following a similar protocol with Cy5-PEG, Cy5-PEG labeled gold nanoparticles, methoxy-terminated PEG (10 kDa) gold nanoparticles, and citrate-coated gold nanoparticles.

f. Photostability Study Imaging Experiment

Cy5-PEG 100 nm gold nanoparticles were dropped between two, round #1.5 cover glass slips (Deckgläser) and allowed to dry while covered in foil at room temperature. Images were taken on a Zeiss LSM 880 with Airyscan microscope with a 633 nm excitation laser. Light scattering images

utilized a 2% laser power, 15/85 dichroic mirror, detector set from 628-638 nm. Fluorescent imaging utilized a 20% laser power, a TD 488/461/633 nm filter, and a detector set from 643-750 nm. A z-plane with thickness of 900 μm was imaged with continuous excitation over the course of 15 minutes. Analysis was completed using ImageJ. The first image was used to create an image mask to isolate each emission center. On each image, the mask was used to obtain the integrated density, or sum of all pixel intensities, at the center of each emission point. These numbers were then converted to proportions of the initial intensity for each individual particle, and those proportions were averaged and plotted as seen in Figure 7.

g. Heparosan Coating of Gold Nanoparticles

Gold nanoparticles were coated with 13 kDa heparosan, synthesized as described in the paper cited here.^[218] Briefly, the required amount of heparosan to achieve the saturation point of 3 molecules/ nm^2 was added to pH 3 hydrochloric acid (Sigma-Aldrich) and gold nanoparticles with a final solution concentration of 1.1 nM 50 nm gold nanoparticles and >50% volume of TCHB buffer. The solution was allowed to sit for five minutes at room temperature before the salt concentration was brought to 0.3 M through addition of 3.43 M sodium chloride (Sigma-Aldrich). After 20 minutes of incubation at room temperature, the salt concentration was brought to 0.7 M and the particles were then concentrated at 1500 xg for 30 minutes before being resuspended in water and DLS and UV-Vis were performed to measure size and concentration compared to initial stock. The hydrodynamic diameter of particles increased ~60 nm, indicating a successful coating.

h. Culture of RAW 264.7 Macrophages

RAW 264.7 macrophages (ATCC, USA) were cultured on T25 and T75 cell culture flasks (NEST) in DMEM (Gibco) supplemented with 10% FBS (Life Technologies) and 1% penicillin-streptomycin (Life Technologies). To passage, cells were removed from the culture surface with a cell scraper and transferred to the proper vessels. For imaging studies, cells were cultured on glass bottom well plates pre-incubated for greater than 2 hours with 2 mg/mL gelatin (Sigma-Aldrich) in water and washed out with both 1x PBS and water.

i. Fixing of Cells

To fix cells, a 4% paraformaldehyde solution (Thermo) in 1x PBS was added to each well for 10 minutes at room temperature. The paraformaldehyde was aspirated, and cell samples were washed 5 times with sterile 1x PBS. Cells were then stained with WGA 488 membrane stain (Biotium) diluted to working concentration in 1x PBS, incubated for 10 minutes at room temperature covered by aluminum foil, and then the solution was aspirated out and cells were washed 3 times with 1x PBS. The same protocol was used to stain the nucleus with Nuc Blue Fixed Cell stain (Invitrogen), except the incubation was for 5 minutes instead of 10. Samples were stored at 4°C and covered in foil until imaging.

j. Cell Imaging Settings

A Zeiss LSM 880 with Airyscan was used for all live cell imaging experiments. A Plan-Apochromat 63x/1.4 Oil DIC M27 objective was used with the following channels: nucleus stain with excitation at 405 nm and emission >445 nm, membrane stain with excitation 488 nm and emission >545 nm, and light scattering channel with excitation at 561 nm and emission from 556-566 nm. Pinholes were standardized to result in the same slice thickness. Laser power and gain

were both kept constant in each sample in an experiment and were set to allow visualization of signal without saturating detectors. These settings were used for both fixed and live cell imaging.

k. Live-Cell Heparosan-Coated Gold Nanoparticle Uptake Study

RAW 264.7 macrophages were cultured on glass bottom plates to a confluency of ~50-60% for imaging. Cells were stained with Nuc Blue Live Cell stain (Invitrogen) and WGA 488 membrane stain (Biotium) for 20 minutes in an incubator before being washed 5 times with 1x PBS. One hour before imaging began, cells were dosed with either 3 μ M cytochalasin D (macropinocytosis inhibitor) or 23.5 μ M chlorpromazine (clathrin-mediated endocytosis inhibitor), each concentration was previously determined to be nontoxic and effective, and placed in a cell incubator to take effect. Cells were loaded onto the microscope equipped with a live cell incubator set at 37⁰C and 5% CO₂ and a 4-frame averaged blank image was taken with the following channels: Nucleus stain, membrane stain, bright field, and light scattering (See settings in *Cell Imaging Settings*). Two different locations in each well were imaged to increase the quantity of cells being monitored in the study. Next, 100 pM 50 nm HEP-AuNPs were dosed into the cell media and gently mixed to homogenize. Each 5 minutes for the next hour, both locations on the plate were imaged with the same settings as the blank control in the z-plane to maximize nuclear area, identifying the center of the cells. This was completed for each of three test groups: cytochalasin D, chlorpromazine, and a non-inhibited control. Data was saved and transferred to ImageJ for analysis. ImageJ's histogram function was utilized for uptake quantification. First, all light scattering-channel images were converted to 8-bit images. Blank controls were analyzed and the maximum pixel intensities across each pre-administration blank was around 25. Thus, to quantify nanoparticle uptake, in each subsequent image the total number of pixels with intensities

above 25 were counted. The number of pixels with intensity greater than 25 was then divided by the number of nuclei in the frame of view to arrive at the unit of analysis: super-threshold pixel counts per cell. This was used because light scattering has relatively high resolution limits, not allowing for distinguishing of individual and aggregated nanoparticles in close proximity.

3. Results

a. Correlation of Scattered Light Intensity and Gold Nanoparticle Size

The results depicting the correlation between measured TEM diameter and light scattering area are shown in Figure 6. Notably, a quadratic relationship is observed due to the quadratic relationship between diameter (TEM) and 2D area in confocal microscopy images (light scattering). The standard deviation in the 200 nm particles may appear large. However, a PDI of 0.1 in 200 nm particles is considered monodisperse.^{[219], [220]} According to equation 1, a PDI of 0.1 in 200 nm particles would result in a particle diameter standard deviation of 62 nm, nearly 1/3 of the actual particle size. Due to a lower post-synthesis yield, 200 nm particles were also dosed in lower concentrations than the other particles, leading to fewer particles being analyzed and thus an increased standard deviation as well. Additional error may arise from the imaging plane not being the plane at which the particles are the largest. Due to their larger size, this is more likely to occur in the 200 nm particles. These results validate the capability of light scattering imaging in gold nanoparticles, show light scattering intensity and particle size are correlated, and show particles were not aggregated when exposed to the high salt concentrations in the hydrogels.

c. Photostability of Cy5-Gold Nanoparticles in Fluorescent and Scattered Light Imaging

To realize live cell imaging over extended periods of time, the nanoparticle must be capable of continued, non-degrading signal over the course of a multiple hour imaging experiment. Scattered light imaging provides a promising avenue to achieve this by using the light reflected off the surface of particles as opposed to light emitted from the particle itself. As mentioned previously, fluorescent particles photo bleach over extended periods of time, reducing their capability to be used in nanoparticle uptake experiments requiring constant imaging over an extended period of time. Figure 7 shows the results of a photostability study, where Cy5-labeled gold nanoparticles were imaged with fluorescent and light scattering imaging techniques over the course of 15 minutes. The fluorescent probes covalently attached to the particles' surface showed a rapid decrease in emission intensity to as low as 20% of the initial intensity whereas scattered light particles maintained a consistently strong signal over the course of the imaging time frame. This effect is visualized in the inset of Figure 7 showing particles imaged before and after exposure to incident light. The figure shows the average relative intensity of 220 particles over the course of the experiment. Fluctuations in scattered light intensity may be due to several factors including variability of laser intensity, interference from cover slips as polyacrylamide gels were not used due to their inability to maintain constant form due to heat-induced volume changes or light-induced dehydration, or light being reflected from other materials on the cover slips. With the fluorescent signal showing lower variations in intensity, and the primary difference between the two being the detector being red-shifted in relation to the excitation laser in the fluorescent imaging setup, the fluctuation in the excitation laser at low intensities may be the most likely cause.

d. Live Cell Imaging Validation and Optimization

Before incorporating uptake pathway analysis into live cell microscopy, validating light scattered imaging of nanoparticles in cells was first required. Light scattering worked as expected in nanoparticle-dosed cells, however a few adjustments were made to better realize this technique: (1) frame averaging was used to reduce in-solution nanoparticle noise and eliminate the need for washing out in solution nanoparticles before imaging and (2) high pass filtering of light scattering pixel intensity was used to prevent the natural light scattering abilities of cellular components from being misidentified as endocytosed nanoparticles. Frame averaging simply images the field of view multiple times and averages each pixel's intensity before moving on to the next channel. In solution particles will show constant Brownian motion, preventing them from accumulating a strong signal in each scan.^[221] In contrast, particles in the process of endocytosis will show drastically less motion, appearing in the same pixel in each scan and thus showing an increase in signal strength. A blank portion of Figure 8 shows differences in background noise quantified before and after addition of line averaging. Secondly, Figure 9 shows the light scattering signal intensity of a cell due to cellular organelles and components in the cytoplasm and a raw image of a cell after nanoparticle endocytosis. Figure 9 then shows the same images with the developed post-image processing applied to eliminate cell background signal and only view the increase in light scattering, or nanoparticles in the cell. The combination of these two techniques enables near total elimination of background signal, as in solution particles are reduced to $\frac{1}{4}$ of their initial intensity and are thus below the background threshold, eliminating them from post-processed images.

e. Fixed Cell Nanoparticle Uptake

With the end goal of quantifying nanoparticle uptake rates at through different endocytotic pathways, the next aim was to find a model setting for these experiments to occur. First, it was noted that the optimal size for nanoparticle uptake experiments was in the 50 nm range.^[222] Previous studies in our research group suggested macrophages have elevated rates of endocytosis, specifically with heparosan coated particles. Because of these previous findings, the model system for validation of gold nanoparticle endocytosis pathway analysis in living cells, a 50 nm heparosan coated gold nanoparticle-RAW 264.7 macrophage system was selected. Particles were coated with heparosan and a statistically significant increase in hydrodynamic diameter was observed (Figure 11). Rapid uptake was required to minimize cost of microscope rental and increase the number of samples possible. Cytochalasin D and chlorpromazine were selected to inhibit uptake through macropinocytosis and clathrin-mediated endocytosis respectively. The next step was to validate the time frame the study would occur. Ideally, sizable uptake within the first hour after dosing with nanoparticles would allow for three different test subjects to be imaged in the four hour maximum imaging window used by the imaging core. To do this, nanoparticles were dosed into untreated, cytochalasin D treated, and chlorpromazine treated RAW 264.7 macrophages and fixed after 30 minutes and 4 hours. Representative results are shown in Figure 11. From these results, it is clear uptake had begun to occur and was quantifiable at the 30 minute timepoint, but was not complete. Additionally, the results show both inhibitors worked, indicating multiple endocytotic mechanisms at play in the uptake of these nanoparticles. With this data, the live cell imaging experiment was planned to mirror the same setup, with the exception of imaging occurring every five minutes through the first hour following dosage with nanoparticles.

f. Live Cell Endocytosis Pathway Monitoring of Gold Nanoparticles

With the information gained from live cell optimization and fixed cell imaging studies, the imaging protocol was adjusted accordingly to realize live cell monitoring of nanoparticle uptake pathways. Figure 12 shows representative images of time progressions in the untreated control, cytochalasin D or macropinocytosis inhibited group, and chlorpromazine or clathrin-mediated endocytosis group. The time points at which images were taken in each group vary slightly due to time needed to readjust the frame of view but are roughly equivalent in each row and are distributed over the course of the first hour following administration of the heparosan coated 50 nm nanoparticles. The results shown here clearly support that heparosan-coated gold nanoparticles are endocytosed into RAW 264.7 macrophages in significant quantities within one hour of administration through both macropinocytosis and clathrin-mediated endocytosis and potentially in a synergistic manner between the two. Within the first hour, the clathrin-mediated endocytosis inhibited cells showed an ~80% reduction in nanoparticle uptake whereas the macropinocytosis inhibited cells showed an ~90% reduction in nanoparticle uptake as shown in Figure 13.

4. Discussion and Future Directions

a. Discussion

The primary interest in this research is the results depicted in Figures 11, 12, and 13 showing how these nanoparticles are endocytosed into the RAW 264.7 macrophages. Notably, the results in the live cell study do not appear to match the results in the fixed cell study. Primarily, the cytochalasin D treated cells in the fixed cell study appear to have notable nanoparticle uptake both in the 30 minute and 4 hour time point whereas the cytochalasin D treated live cells show very little uptake throughout the first hour following administration. Although both results support a macropinocytosis-based and clathrin-mediated endocytosis mechanism, the extent to which each pathway contributed to overall uptake is in question. A few possible explanations for this are: first, the cells were more comfortable in the incubator than in the microscope incubator, causing higher uptake in the fixed cells which weren't imaged over the course of the uptake. However, if this was the case, a proportional drop in the control would be expected, which did not occur. The differences between the control and treated groups were in the administration of uptake pathway inhibitors, which may have affected cell viability. However, cell membrane rupture was observed in previous experiments (data not shown) but did not occur here, meaning the cells were alive throughout the whole hour of imaging. Potentially the combination of near constant laser excitation and uptake inhibitors may reduce the activity of cells as a viability assay, not a metabolic assay was conducted to determine acceptable inhibitor doses. However, no literature was found to support any sort of light-mediated effects of either inhibitor. Other potential sources of variation between the fixed and live cell images could be that nanoparticles attached to cell membranes in the fixed cell image or in extracellular matrices were not entirely washed out and thus are visible in the fixed cell image but are not truly inside the cell. However,

this effect was not visible on the chlorpromazine-treated cells in the fixed images. It is noted that chlorpromazine prevents the assembly of clathrin lattices in intracellular vesicles and on cell membranes, which, if the nanoparticles bind this lattice, could explain the nanoparticles around the membrane of the macropinocytosis-inhibited cells where the clathrin lattice still forms and not the clathrin-mediated inhibited cells.^[223] This could also be a source of the synergistic effect, where macropinosomes are able to engulf large amounts of cytosol at once, and if nanoparticles are already bound to clathrin lattices on the cell membrane, the number of nanoparticles engulfed in a macropinosome would increase notably. Additional support for this hypothesis is in the rapid increase in signal in the macropinocytosis-inhibited live cells, indicating nanoparticles associating with the cell membrane, but a notably slower increase in signal over the course of the rest of the hour, potentially indicating these nanoparticles have saturated the membrane and moving in at a slower rate. However, the variation in uptake in the control near the end of the hour may point to the results being within measurement error and more information and studies will need to be conducted before using this technique to more confidently make statements regarding the rates of uptake in these experiments. Regardless of the mechanism, our live cell images support the fixed cell image data showing that both clathrin-mediated endocytosis and macropinocytosis play influential roles in the uptake of heparosan nanoparticles and this was determined using a live cell imaging technique enabling quantification at many time points and minimal preparation for uptake analysis in our model study.

b. Future Directions

In addition to replicating the experiment to confirm preliminary results, future experimentation is required to better realize the capabilities of this technology. In order to increase the accuracy of measurements, a first step would be developing a macro in ImageJ to

more rapidly analyze large data sets, enabling quantification of individual cell uptake as opposed to dividing total uptake by the total number of cells. Reanalyzing the current data using a cell-specific technique and confirming matching results would be useful. Additionally, development of a more accurate analysis technique and multiple trials would enable more accurate conclusions to be made about the uptake rate over the course of the time imaged.

With regards to the apparent synergistic enhancement of macropinocytosis and clathrin-mediated endocytosis, in addition to repeating the experiment to confirm current results, a potential experiment would be to conjugate antibodies or proteins to nanoparticles that bind to a different cell membrane receptor to enhance macropinocytosis efficiency with the hypothesis that, if the idea that nanoparticles are binding to clathrin lattices on cell membranes but then endocytosed through macropinocytosis, finding an alternative binding site on a cell membrane should achieve approximately equal uptake rates as the untreated control when dosed with a clathrin-mediated endocytosis inhibitor.

Live cell imaging and nanoparticle tracking in tandem also have the capability to monitor intracellular nanoparticle fate in addition to their uptake pathway. Of potential interest and current pursuit is in labeling endosomes and lysosomes and using increased zoom objectives to track and establish relationships between the monitored uptake pathway and the intracellular fate.

Finally, if more accurate quantifications of cellular uptake are coupled with the ability to track nanoparticles as they progress to an intracellular fate, this technique will have the capability to, in real-time, identify the ratios by which endocytosis pathways contribute to nanoparticle uptake and use each pathway-inhibited test group to see the intracellular destination of each pathway-specific nanoparticle population. By realizing this technology, and conducting

tests on how size, surface coating, and other physicochemical properties affect a nanoparticle's uptake and intracellular pathway, rational, results-based design can be applied to nanoparticle engineering to increase therapeutic efficacy and delivery efficiency.

c. Contributions

For the initial review manuscript covering the applications of upconversion nanoparticles in bioimaging, concepts and revisions were made by other lab members and advisors. The author of this thesis developed figures, conducted background research, and was primarily responsible for all writing in the manuscript. In the research portion of the thesis, the project idea was presented by the principal investigator, and the thesis author completed all imaging experiments, developed techniques for live cell imaging and background reduction, analyzed all data, and drew independent conclusions from the data presented.

5. Acknowledgments

This research was supported in part by the University of Oklahoma (OU) IBEST-OUHSC Seed Grant for Interdisciplinary Research, the Oklahoma Center for the Advancement of Science and Technology OCAST (HR20-106), the NSF CAREER (2048130), the University of Oklahoma Faculty Investment Program, the Oklahoma Tobacco Settlement Endowment Trust (TSET) awarded to the University of Oklahoma, Stephenson Cancer Center, and an NIH COBRE award (P20GM135009).

Additional thanks to my graduate thesis committee: Dr. Stefan Wilhelm, Dr. Rebecca Scott, & Dr. Wei Chen; core facility staff: Dr. Ben Fowler, Dr. Tingting Gu, and Justin Willige; laboratory colleagues: Vinit Sheth, Wen Yang, Dr. Lin Wang, Alex Frickenstein, Dr. Nathan Donahue, Alyssa Holden, and Emmy Francek; friends, family and wife Lily.

6. Figures

a. Figure 1: Interactions Between Light and Biological Tissue

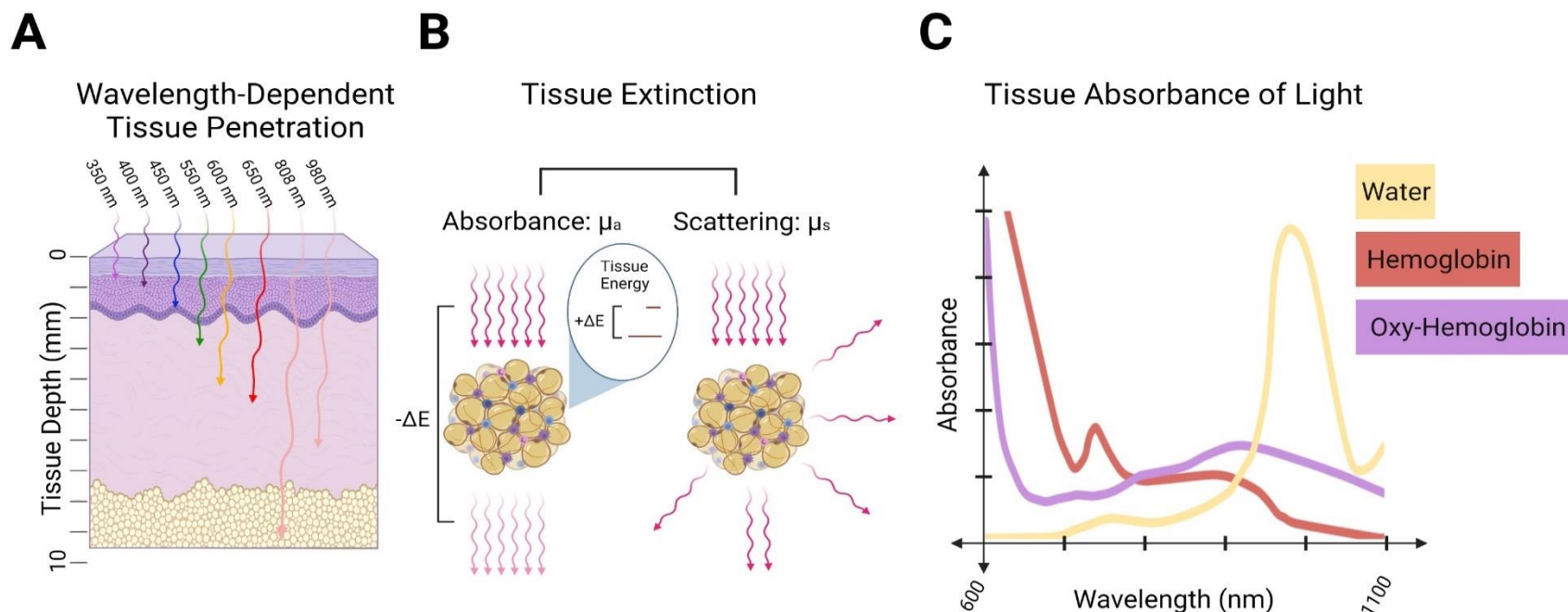


Figure 1: (A) The tissue penetration of light is wavelength-dependent. Longer wavelengths typically tend to exhibit deeper penetration depths in biological tissue. The light tissue penetration data in this diagram is based on a report by Ash *et al.* and indicates the approximate depth at which 1% of incident light energy of a 10-mm-wide laser in a skin model still exists.^{[44], [52]} Note: The 808-nm and 980-nm lasers are commonly used excitation sources for upconversion nanoparticles. It should be noted the 808-nm and 980-nm laser depths are from a separate study and thus not directly comparable to the visible light penetration depths due to change in experimental conditions.^{[44], [52]} (B) This wavelength-dependent light penetration depth is a result of longer wavelengths typically exhibiting lower coefficients of absorbance (μ_a) and scattering (μ_s), i.e. lower extinction. Light absorbance occurs when light energy is transferred to the tissue upon irradiation. Light scattering occurs when light reflects off the tissue components, causing a reduction in the intensity of light continuing through the tissue. (C) The near-infrared (NIR)-I optical window of biological tissue is in the wavelength range of ~700-1,000 nm. Biological tissues exhibit a relatively low tissue attenuation within the NIR-I window, enabling improved light-based imaging through NIR-based lasers. Within this optical window, 808-nm lasers typically exhibit deeper tissue penetration than 980-nm lasers due

to the locally elevated absorbance of water in the 950-1,050 nm range. On the other hand, wavelengths <700 nm are absorbed efficiently by tissue components, such as hemoglobin.^[224]

b. Figure 2: Visualization of Individual Upconversion Nanoparticles Through Super-Resolution Techniques

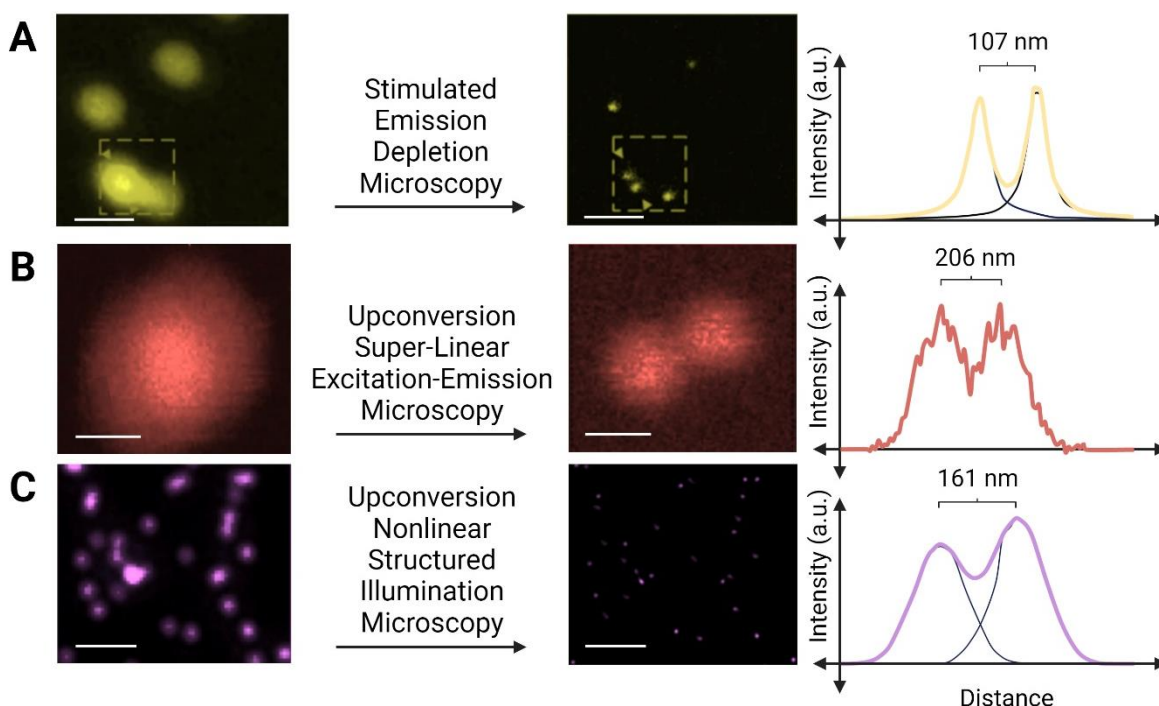


Figure 2: (A) Super-resolution stimulated emission depletion microscopy (STED) images of 40-nm UCNPs doped with NaYF₄ (20% Yb and 8% Tm). The authors reported a lateral resolution limit of 28 nm when using 13-nm UCNPs at an excitation power of 7.5 MWcm⁻² (scale bar = 500 nm).^[41] Reprinted by permission from Springer Nature: Nature, Amplified stimulated emission in upconversion nanoparticles for super-resolution nanoscopy, Liu *et al.* Copyright 2017. (B) Upconversion super-linear excitation-emission microscopy (uSEE) can resolve NaYF₄ (20% Yb/8% Tm) UCNPs separated by ~200 nm. The authors reported lateral and axial resolutions of 184 nm & 390 nm respectively using the uSEE technique (scale bar = 200 nm).^[121] Reprinted with permission from reference 121 with permission. (C) Upconversion nonlinear structured illumination microscopy (U-NSIM) has been used to image NaYF₄ (20% Yb/4% Tm) UCNPs. The authors noted the ability to resolve individual UCNPs separated by 161 nm (scale bar = 2 μm).^[42] Adapted with permission from Liu *et al.* Upconversion Nonlinear Structured Illumination Microscopy. *Nano Lett.* 20, 4775–4781 (2020). Copyright 2020 American Chemical Society.

c. **Figure 3: Potential Approaches for Upconversion Nanoparticle-Based Multiplexing in Cellular Imaging**

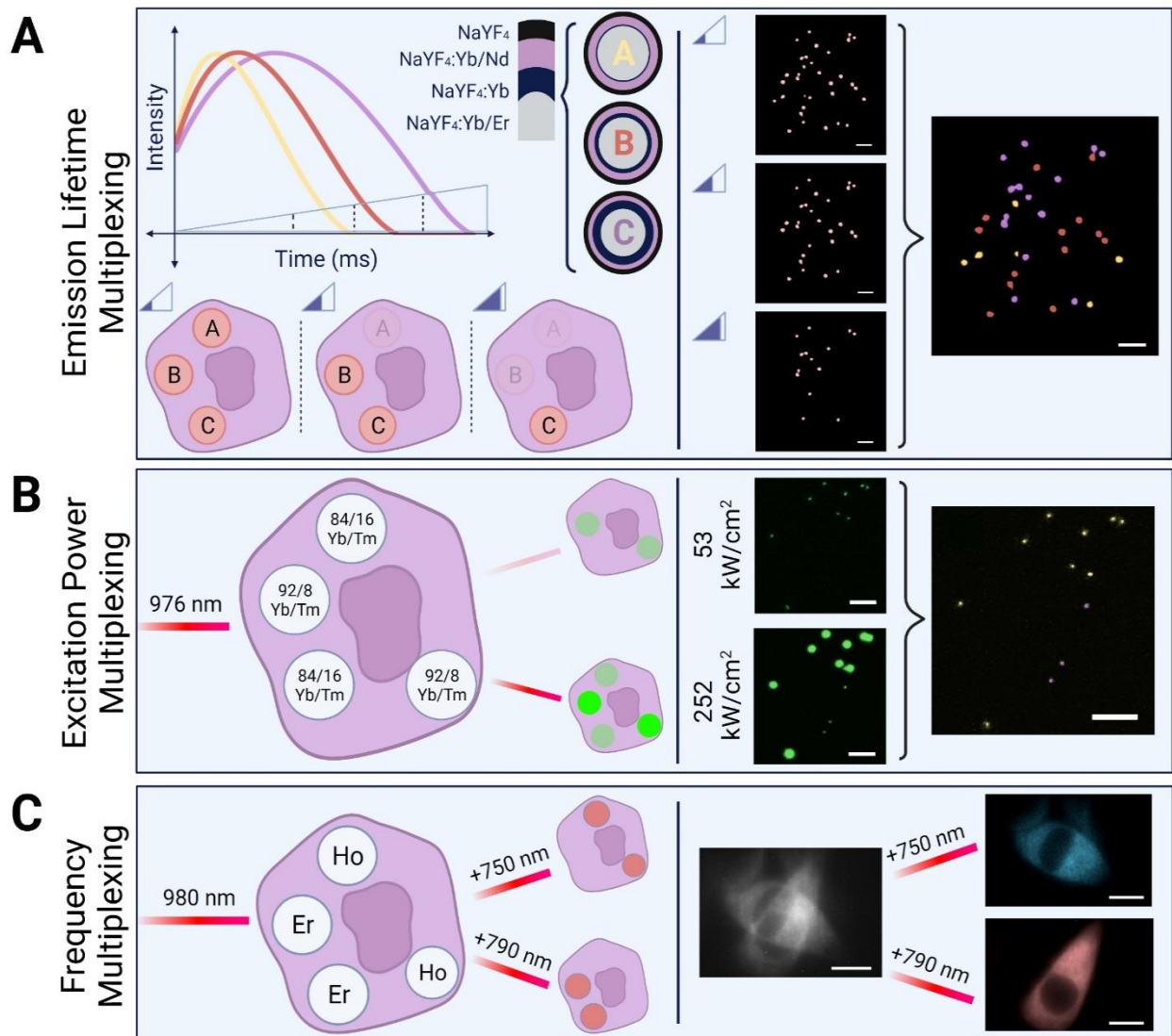


Figure 3: (A) Wang *et al.* demonstrated upconversion luminescence lifetime engineering to control the UCNPs' emission lifetimes through nanoparticle design (scale bars = 2 μm).^[25] The engineered UCNPs can be detected and identified by their characteristic upconversion luminescence lifetimes in selected timepoint images potentially enabling UCNPs emission lifetime multiplexing for cellular imaging. Reproduced from reference 25 with permission from the Royal Society of Chemistry. (B) Excitation power multiplexing of UCNPs exploits changes in lanthanide ion dopant concentrations of various UCNPs to alter the power thresholds necessary for UCNPs detection. Combined with the super-linear relationship between excitation power and upconversion emission intensity, lower-doped UCNPs are visible at lower excitation powers and saturate at similar laser powers where the higher-doped UCNPs begin to be visible, enabling distinction of the two UCNPs populations for potential applications in cellular imaging (scale bar = 1 μm).^[24] Reproduced from reference 24 with permission from the Royal Society of Chemistry.

(C) Vosch *et al.* demonstrated a frequency-encoding method to enable UCNP multiplex imaging (scale bar = 10 μm). Co-excitation with secondary lasers targeted specific energy transitions for enhanced absorption by either holmium or erbium.^[149] Adapted with permission from Lisberg, M. B., Lahtinen, S., Sloth, A. B., Soukka, T. & Vosch, T. Frequency Encoding of Upconversion Nanoparticle Emission for Multiplexed Imaging of Spectrally and Spatially Overlapping Lanthanide Ions. *J. Am. Chem. Soc.* 143, 19399–19405 (2021). Copyright 2021. American Chemical Society.

d. **Figure 4: Upconversion Nanoparticles Enable Multimodal Imaging and In Vivo Imaging**

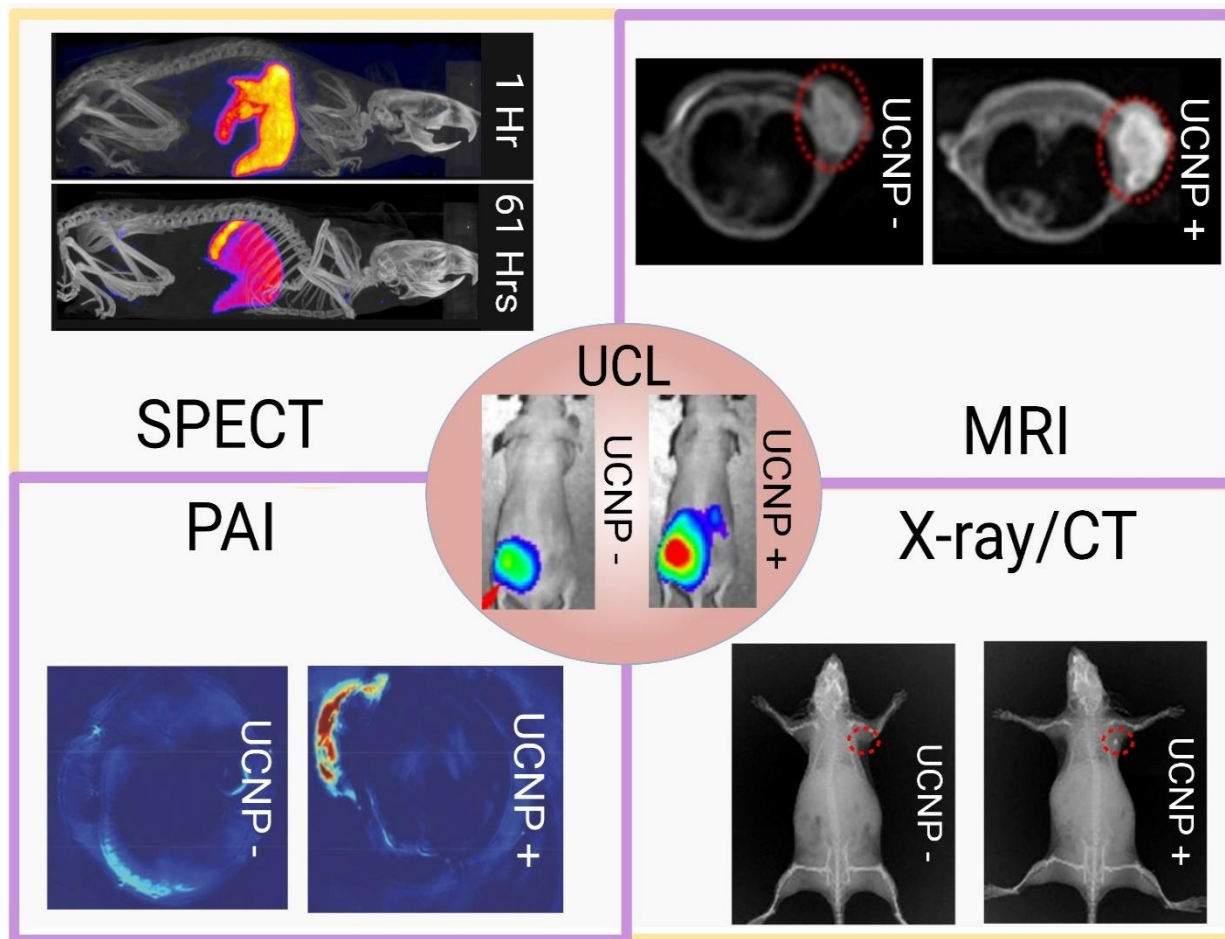


Figure 4: UCNPs can be designed for multimodal imaging, including but not limited to X-ray/computed tomography (CT) imaging, photoacoustic imaging (PAI), single-photon emission computed tomography (SPECT) and magnetic resonance imaging (MRI). The center circle shows the substantial increase in upconversion luminescence signal following local administration of UCNPs in mice.^[43] Reprinted with permission from Zhao, J., Chu, H., Zhao, Y., Lu, Y. & Li, L. A NIR Light Gated DNA Nanodevice for Spatiotemporally Controlled Imaging of MicroRNA in Cells and Animals. *J. Am. Chem. Soc.* 141, 7056–7062 (2019). Copyright 2019 American Chemical Society. T₁-MRI images of tumor bearing mice following injection of PEGylated NaYF₄:Yb,Er@NaGdF₄ encapsulated in tumor-targeting antibody-conjugated micelles (Top Right).^[159] Reproduced with permission from reference 159. CT imaging following subcutaneous injection of BiF₃:Yb,Er UCNPs (Bottom Right).^[63] Reproduced with permission from reference 63. Photoacoustic *in vivo* images of gold nanorod dimer-UCNP-chlorin e6 injected via tail injection accumulating in mouse-grafted HeLa cell tumors (Bottom Left).^[225] Reproduced with permission from reference 225. SPECT imaging monitoring ¹⁵³Sm radiolabeled UCNPs accumulation in specific organs following injection in mice (Top Left).^[226] Reproduced with permission from reference 226.

e. **Figure 5: Agarose gels**

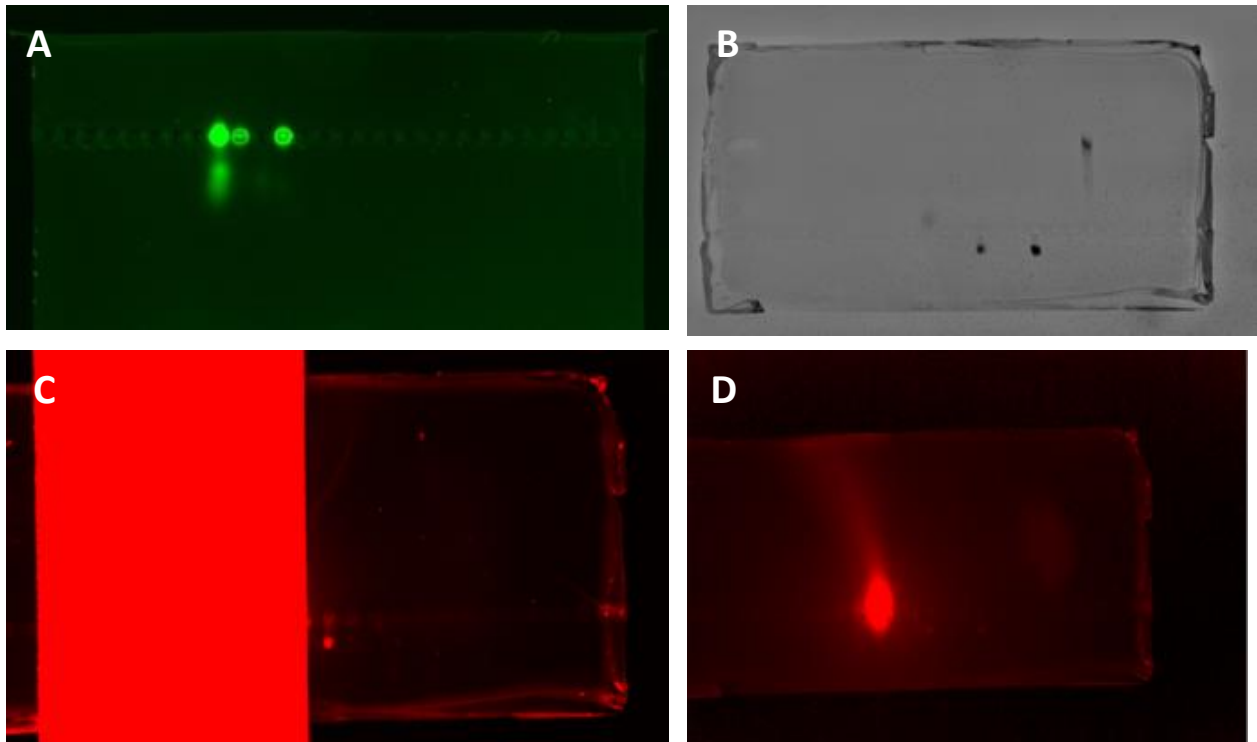


Figure 5: Agarose gels assessing purity of Cy5-PEG and efficiency of fluorescent tagging of gold nanoparticles. (A) From left to right: impure fraction, pure fraction, column flowthrough, and previously synthesized Cy5-PEG imaged with fluorescence camera and Cy5 excitation (633 nm). (B) Visual image of gel following agarose gel separation. From left to right: Cy5-PEG, Cy5-gold nanoparticles, PEGylated gold nanoparticles (10 kDa methoxy-terminated PEG), and citrate-coated gold nanoparticles. (C) High exposure Cy5 (633 nm) image of gel in B with Cy5-PEG well blocked to prevent overblown signal. (D) Low exposure image of gel showing fluorescence of Cy5-PEG.

f. Figure 6: Correlation of Scattered Light Intensity and TEM Size in Gold Nanoparticles

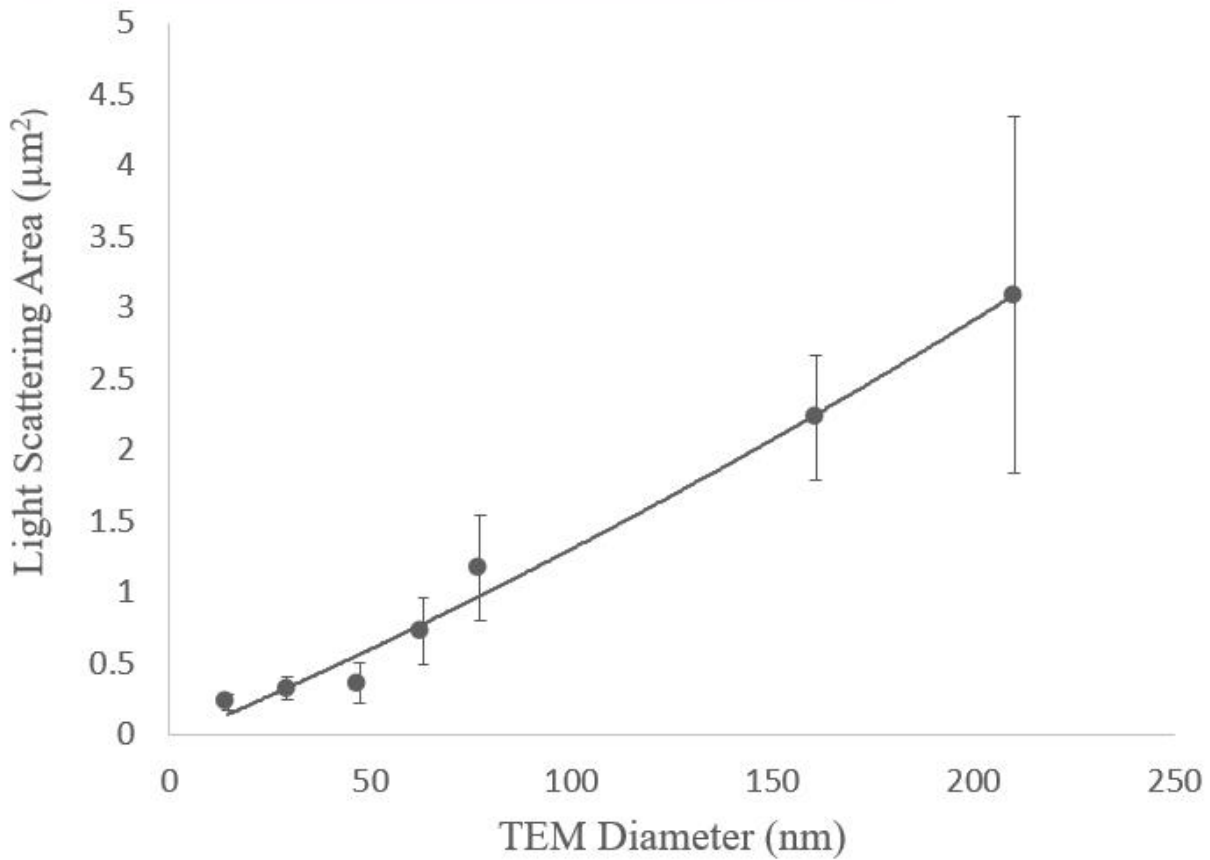
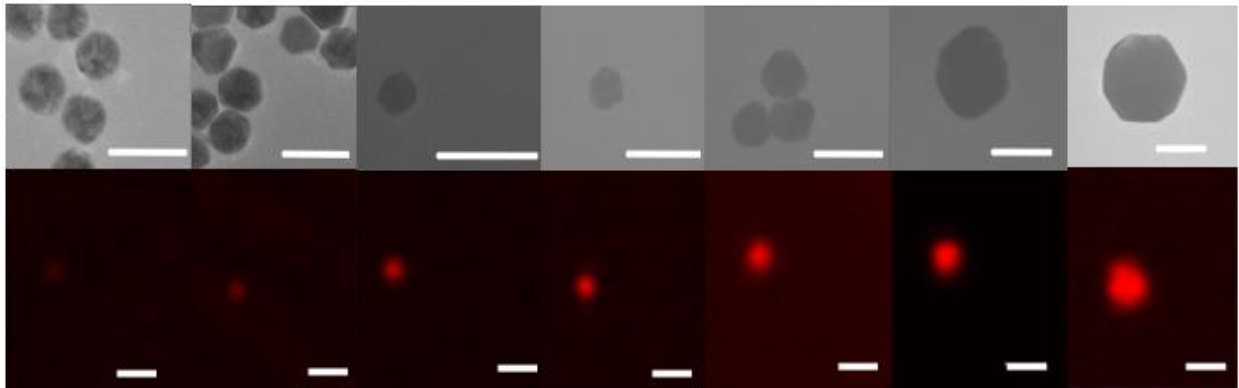


Figure 6: Size correlation between TEM (A) and light scattering (B) images of gold nanoparticles (Left to Right: 15, 30, 45, 60, 80, 150, & 200 nm). TEM number of particles analyzed: 23, 111, 12, 13, 16, 12, 22. Light scattering number of particles analyzed: 24, 64, 37, 57, 50, 44, 13. TEM scale bars: 25, 50, 125, 125, 125, 125, 125 nm. Light scattering scale bars: 1 μm . Error bars represent one standard deviation in measured area.

g. Figure 7: Photostability of Light Scattering Imaging

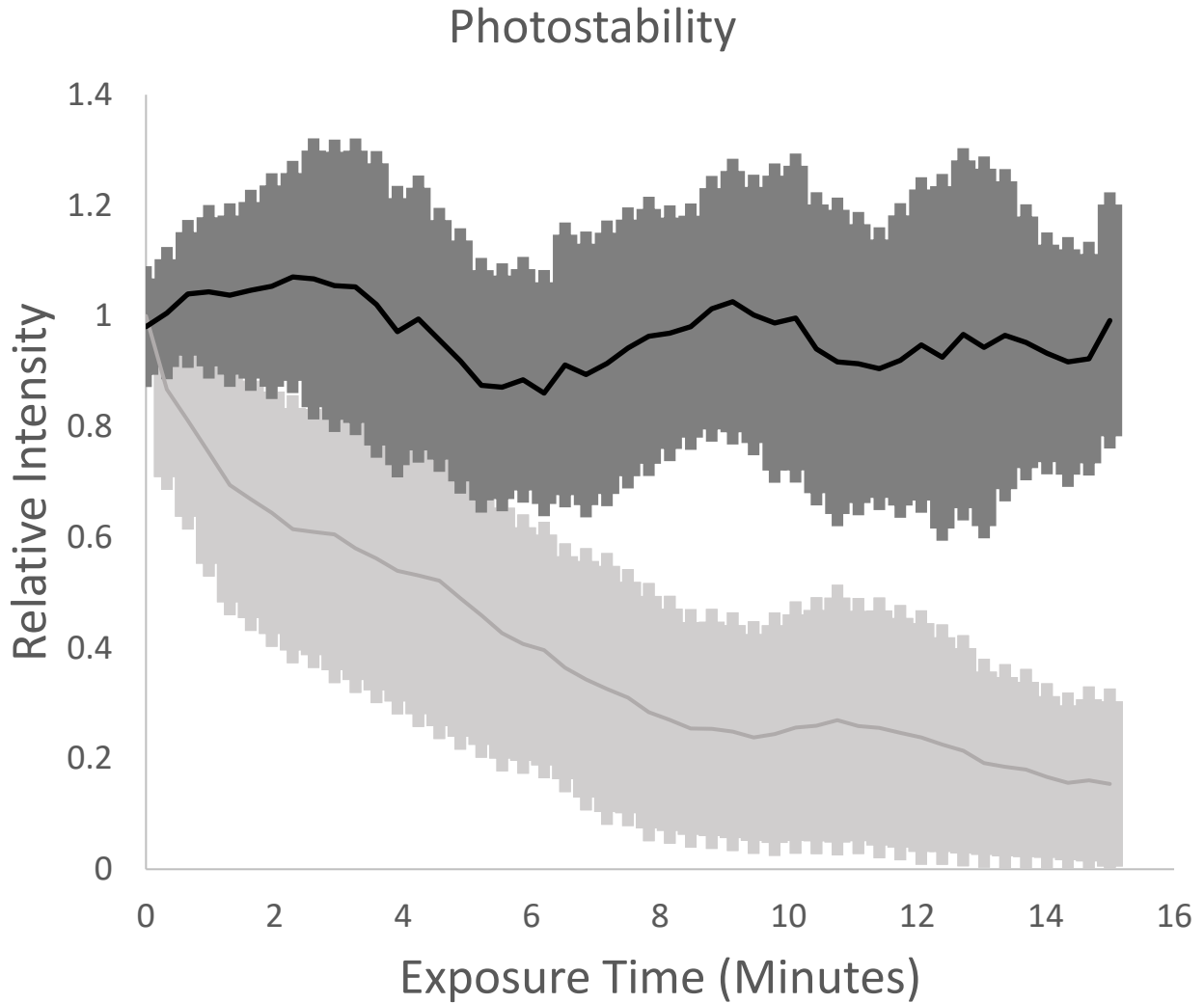


Figure 7: Relative intensities as a function of exposure time for scattered light imaging (black) and fluorescent imaging (grey) of the same Cy5-labeled gold nanoparticles. The results shown are averaged relative intensities of 220 particles. Representative intensities of a Cy5-labeled nanoparticle imaged with fluorescent (left/green) and light scattering (right/gray) techniques before (left pair) and after (right pair) 15-minute exposure to excitation laser. Shaded areas represent one standard deviation of the particle population analyzed.

Figure 8: Effect of Frame Averaging

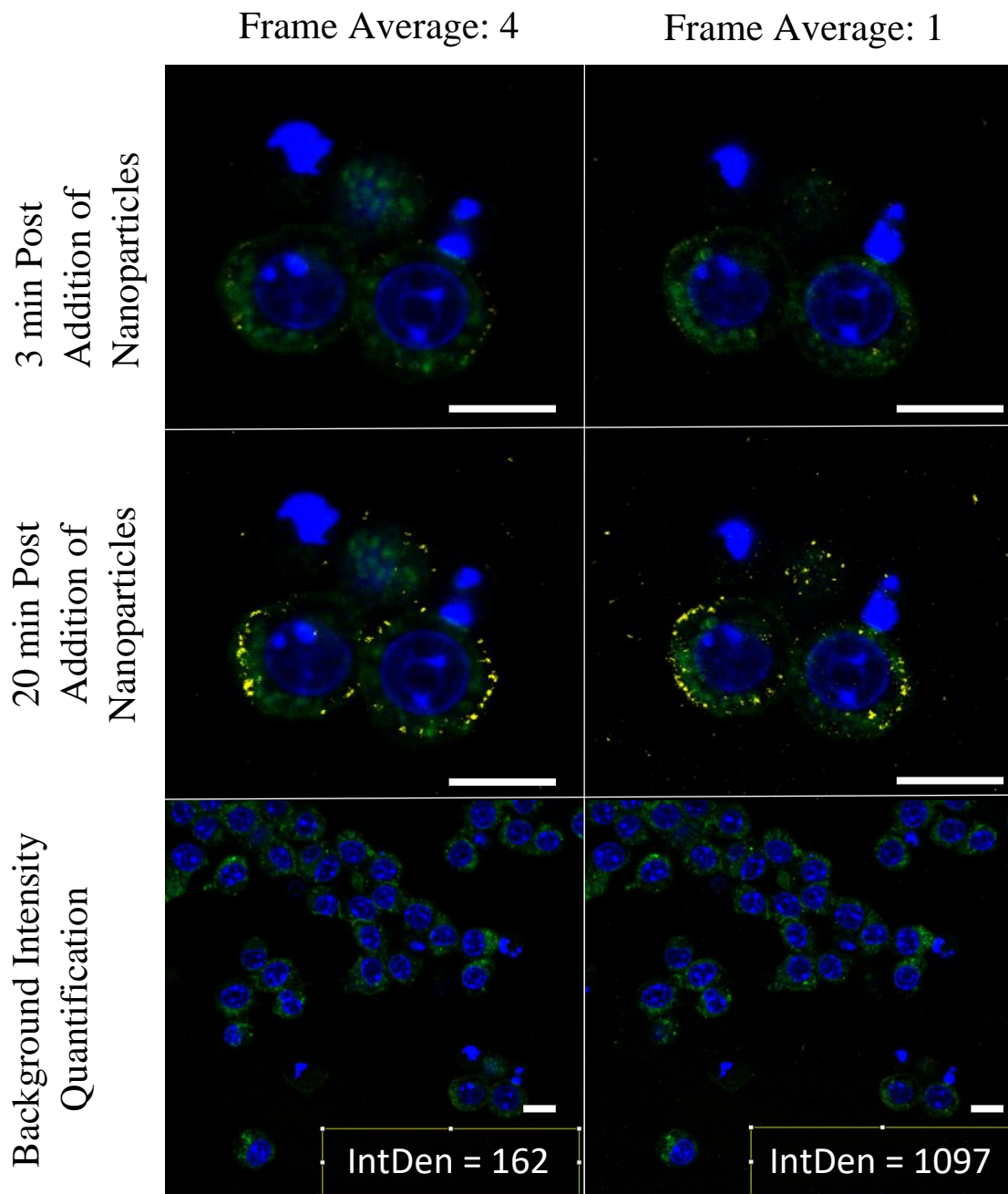


Figure 8: Reduction of in solution nanoparticle signal through use of frame averaging. The same cells were imaged twice, once with a frame average of 4 (left) and once with a frame average of one (right). In post-processing, background was removed through blank-adjustment and then raw data was portrayed (top) and the dynamic range was adjusted to better show nanoparticle signal (middle). Finally, background intensity was quantified over the boxed region, and frame averaging was found to reduce background noise by a factor of ~6.5 (bottom). Blue represents a nucleus stain, green is a membrane stain, and yellow is the light scattering signal, scale bars = 10 μm .

h. Figure 9: Effect of Background Filtering

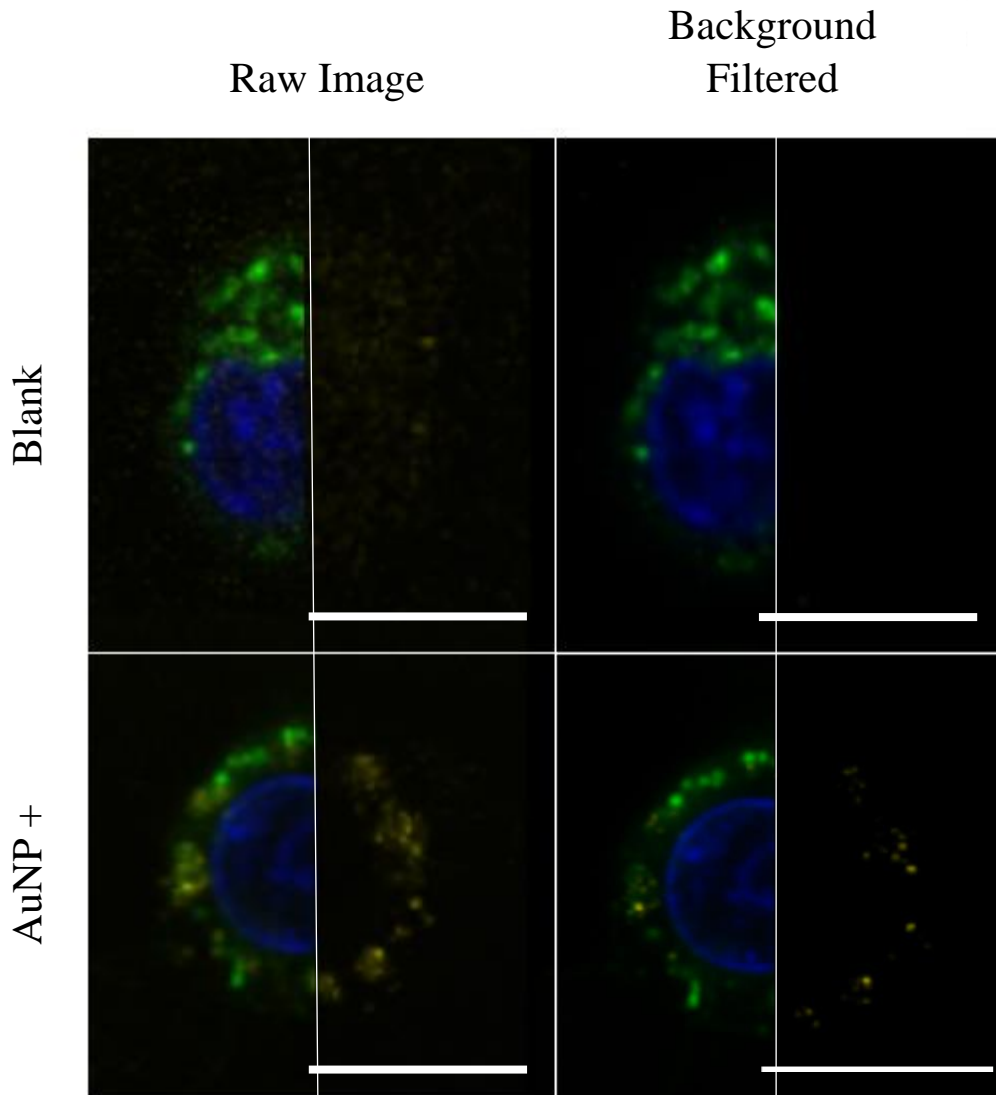


Figure 9: Utilization of pixel-intensity filtering to eliminate light scattering signal from cellular components. A blank control (top) and a nanoparticle-treated sample (bottom) are shown with the membrane and nucleus signal removed on the right half of the images, isolating the light scattering signal before (left) and after (right) applying the same high-pass pixel intensity filter, which was shown to eliminate the cell light scattering signal while still allowing endocytosed nanoparticles to be visible. Blue represents a nucleus stain, green is a membrane stain, and yellow is the light scattering signal, scale bars = 10 μm .

i. Figure 10: Heparosan Coating of AuNPs

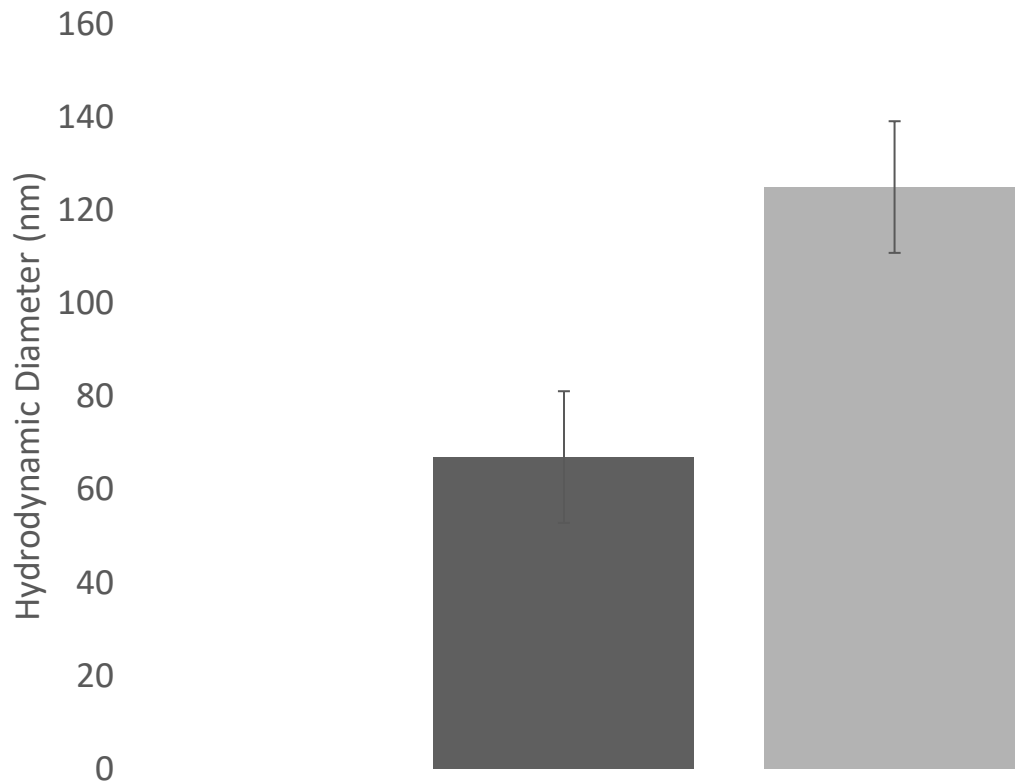


Figure 10: Hydrodynamic diameter and standard deviation of nanoparticles before (left) and after (right) coating of nanoparticles with heparosan by pH adjustment. Error bars represent one standard deviation as calculated by the polydispersity index (PDI). The results confirm successful synthesis with a p-value well below the 0.05 threshold.

j. **Figure 11: Fixed Cell Imaging of Heparosan AuNPs with Uptake Inhibitors**

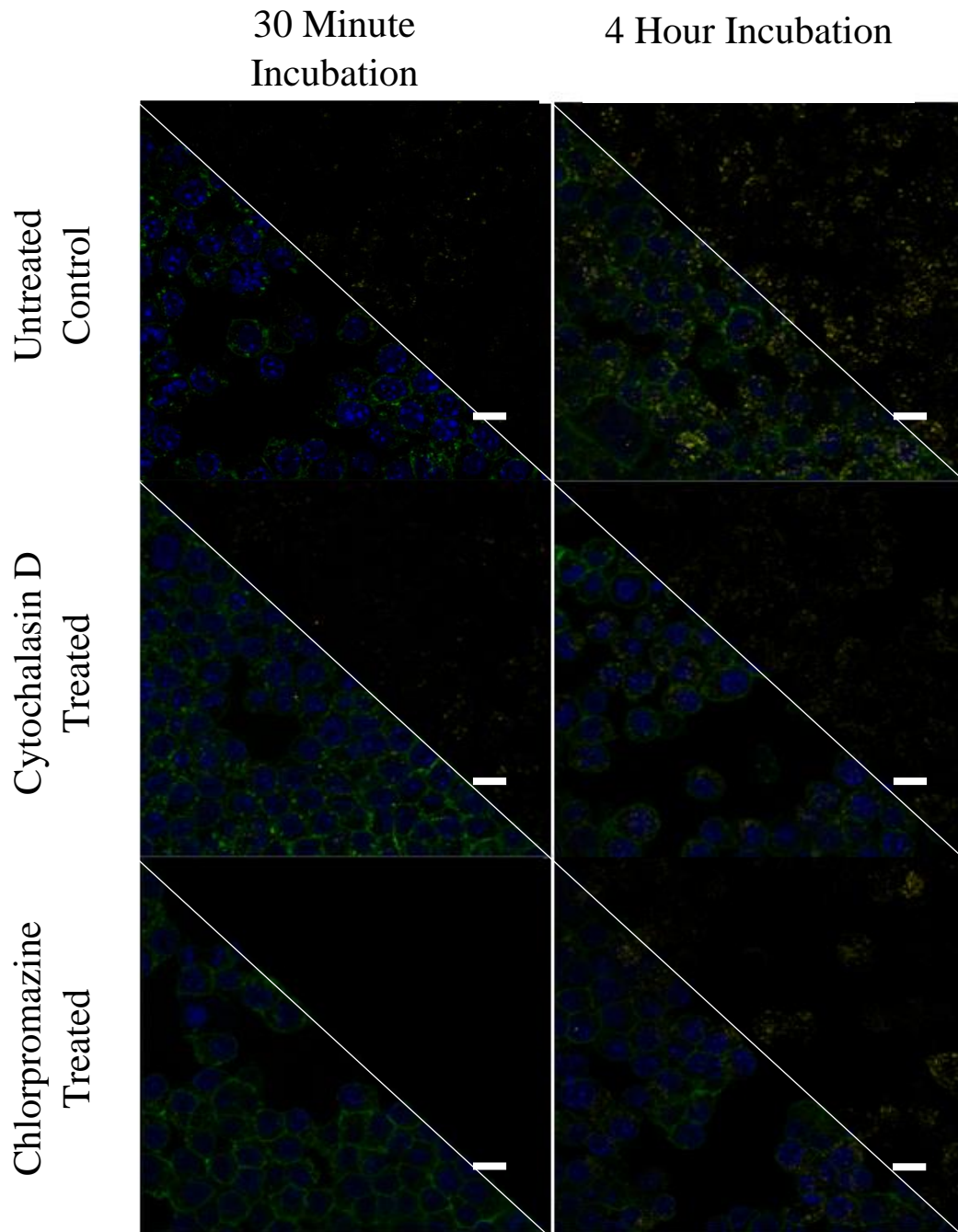


Figure 11: Fixed cell visualization of nanoparticle uptake by RAW 264.7 macrophages untreated (top), treated with cytochalasin D (middle), or treated with chlorpromazine (bottom), following 30 minutes (left) or 4 hours (right) of incubation with heparosan-coated nanoparticles. Nanoparticle uptake is visible at the 30-minute time point and both inhibitors qualitatively appear to reduce nanoparticle uptake when compared to the control. Once again, the membrane and nucleus signal are removed in the top right of the images to better visualize light scattering signal. Blue represents a nucleus stain, green is a membrane stain, and yellow is the light scattering signal, scale bars = 10 μ m.

k. **Figure 12: Live Cell Imaging of Heparosan AuNPs with Uptake Inhibitors**

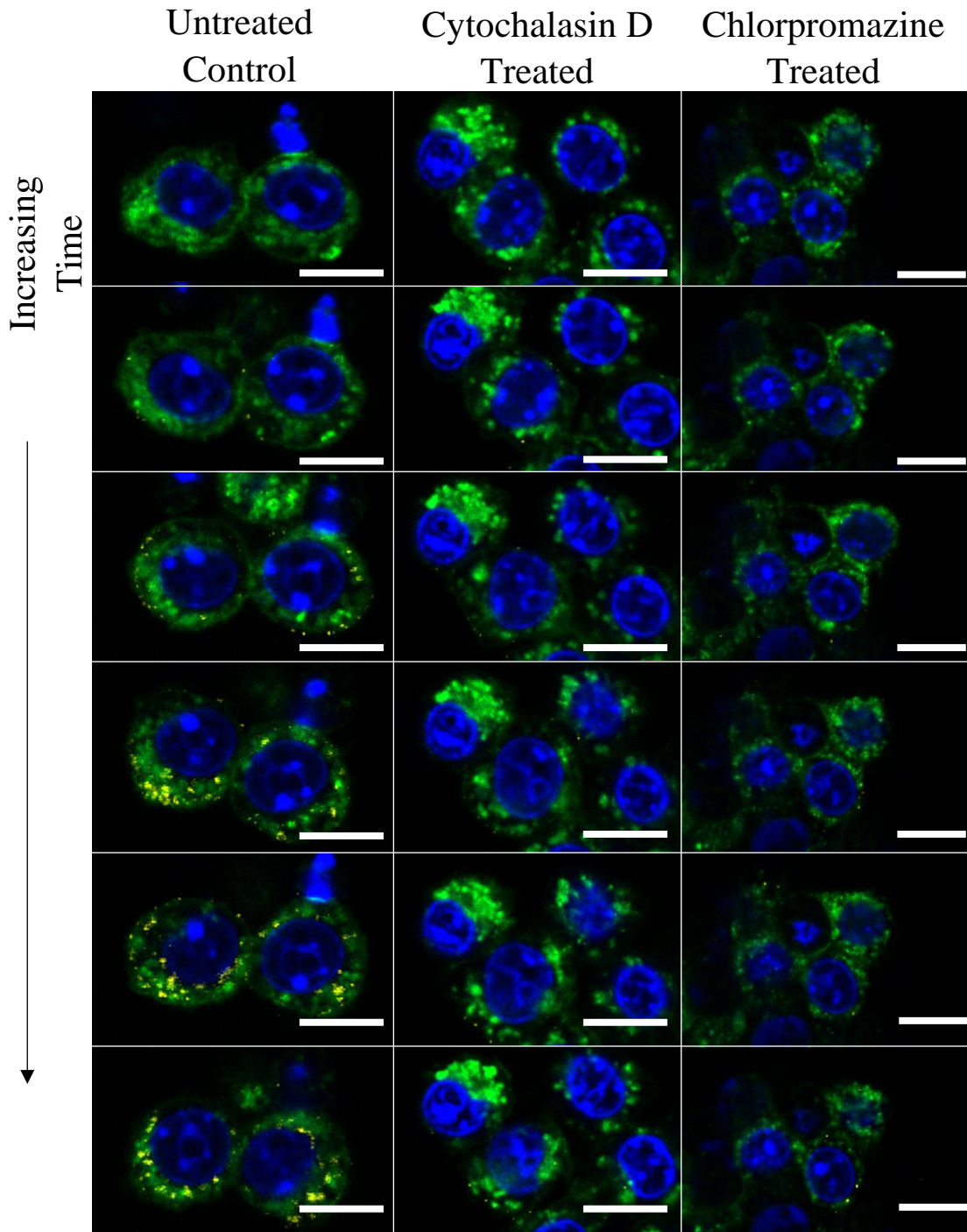


Figure 12: Live cell nanoparticle uptake by RAW 264.7 macrophages in first hour following administration of 100 pM heparosan AuNPs untreated (left), treated with cytochalasin D (middle, micropinocytosis inhibited), or treated with chlorpromazine (right, clathrin-mediated endocytosis inhibitor). Blue represents a nucleus stain, green is a membrane stain, and yellow is the light scattering signal, scale bars = 10 μm

1. Figure 13: Quantification of Heparosan AuNP Nanoparticle Uptake

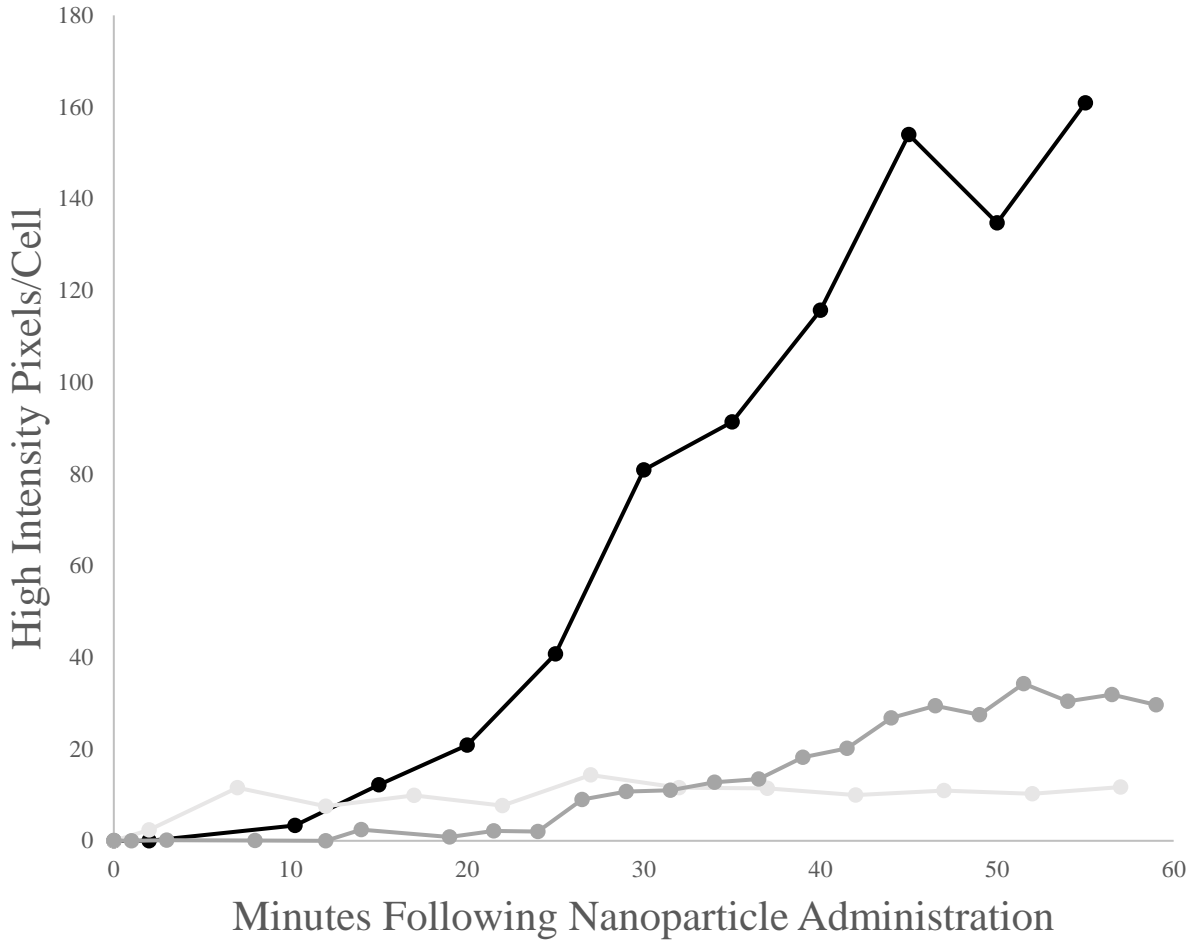


Figure 13: Quantification of high intensity pixels per cell in RAW 264.7 macrophages following administration of 100 pM heparosan AuNPs. Both the macropinocytosis inhibitor cytochalasin D (light grey) and the clathrin-mediated endocytosis inhibitor chlorpromazine (dark grey) showed notable reductions in nanoparticle uptake when compared to the untreated control (black). Each test group was analyzed with the same technique and shows the average pixel count of over 25 cells in the field of view. A single analysis was completed so no error bars are available.

7. Tables

a. **Table 1: Select Examples of Bioimaging Applications with Upconversion Nanoparticles***

UCNP Composition	UCNP Size (nm)	Demonstrated Application	Imaging Depth	Excitation/ Emission (nm)	Ref.
Image Enhancement					
NaYF ₄ @NaYbF ₄ @NaYF ₄ :10-99% Yb/1% Tm@NaYF ₄ @PAA	6-49	In vivo lifetime multiplexing of UCNPs	6 mm	980	[92]
LiF ₄ : 99% Er/1% Tm@LiYF ₄	8	Imaging onion microstructures	Imaged in onion cells	980/Visible	[227]
NaF ₄ : 40% Yb/60% Er@NaYGdF	12	Low excitation intensity upconversion imaging	Imaged in mammary pads 3-4 mm deep	980/530-550	[170]
NaF ₄ : 98% Yb/2% Er@CaF ₂	14	Emission intensity optimization for naked eye-visible UCNPs	Visible in mouse forearm	980/Visible	[97]
NaYF ₄ : 20% Gd/0.5% Tm@NaGdF ₄	15	Energy-looping nanoparticles for imaging through brain tissue phantoms	1 mm	1064/800	[123]
NaGdF ₄ : 20% Yb/2% Er@CaF ₂	16	Novel cation exchange UCNP synthesis method as well as shell UCL enhancement	Imaged near mouse hip	980/<680	[228]
NaLuF ₄ : 20% Yb/1% Tm	19	Increase in contrast and reduction in tissue overheating using time-gating imaging approach	Imaged near mouse side	980	[57]
NaYF ₄ : 20% Yb/2% Tm	20	Early paper showing in vivo imaging of UCNPs	Imaged in mouse abdomen	975/800	[229]
NaYF ₄ : 20% Yb/2% Er@polyglutamic dendron	23	Mapping mouse vasculature as well as pH sensing with low power excitation	0.2 mm	980, 808	[69]

NaYF ₄ : 20% Yb/8% Tm@PEI	25	Time-gating approach for reduction in background fluorescence	Imaged in excised spleen	975/455	[61]
NaYF ₄ : Mn ²⁺ /18% Yb/2% Er@PEG	25 (no PEG)	<i>In vivo</i> imaging of mice following injection of particles	15 mm	980/<800	[53]
NaYF ₄ : 20% Yb/0.5% Tm	~25	Super-resolution technique for resolving lines through liver tissue with increased speed of imaging	0.051 mm	976/800	[42]
NaF ₄ : 66% Yb/30% Gd/2% Ce/2% Er@NaYF ₄ :10% Yb@Ag ₂ Se QDs	26	Quantum dot-sensitized UCNPs for imaging of traumatic brain injury	11 mm	980/>1300	[104]
NaF ₄ : 99.5% Er/0.5% Tm@NaYF ₄ @SiO ₂	28	Multi-excitabile UCNPs with enhanced upconversion	Imaged near mouse hip	1532, 980, 808/Short pass	[230]
NaYF ₄ : 80% Yb/6% Er@NaYF ₄	28	Imaging of nanoparticles <i>in vivo</i> using minimal excitation power	4 mm	980/647-673	[231]
NaYF ₄ : 20% Yb/2% Er@Dendrimer	30	Deep mapping of mouse brain vasculature at low excitation power	1 mm	980/<890	[129]
NaYF ₄ : 40% Yb/4% Tm	41	Super-resolution techniques for imaging individual nanoparticles through liver tissue	0.093 mm	980/<842	[118]
NaGdF ₄ : 20% Yb/2% Er @ BSA·DTPAGd	43	Strategies for gadolinium integration for MRI in mice	MRI only	N/A	[232]
ZrOCl ₂ : 3.14% DCDPA/3.14% Pd-TCPP	55	Metal organic alternative framework for low power density (0.005 W/cm ²) of lymph nodes	Imaged subcutaneous lymph nodes	532/425-475	[233]
NaYF ₄ : 20% Yb/5% Gd/2% Er@NaYF ₄ @Ag ₂ Se QDs	62	Enhancement of PDT and luminescence activity through quantum dots	Imaged in mouse back	800	[103]
NaYF ₄ : 30% Yb/0.5% Tm@NaYF ₄ @SiO ₂ @OTMS@F127	84	Brain vessel mapping and <i>in vivo</i> UCL imaging	Imaged in mouse chest	980/750-900	[234]

Novel Architectures and Surface Coatings					
K ₃ ZrF ₇ : 20% Yb/2% Er	27	Monitoring biodegradable nanoparticles <i>in vivo</i>	~7 mm	980/Visible	[166]
NaGdF ₄ : 70% Yb/1% Tm@NaGdF ₄ @Poly-d-lysine/DNA	38	Specific MiRNA-enhanced luminescence for detection in mice	Imaged near mouse hip	980	[43]
NaGdF ₄ : 18% Yb/ 2% Tm@NaGdF ₄ @Cancer Cell Membrane	48	Multimodal targeting and differentiation between triple negative and MCF7 breast cancer cells	Imaged near mouse rear	980/790	[141]
ZrOCl ₂ : 3.14% DCDPA/3.14% Pd-TCPP	55	Metal organic alternative framework for low power density (0.005W/cm ²) of lymph nodes	Imaged subcutaneous lymph nodes	532/425-475	[233]
NaYF ₄ : 18% Yb/0.6% Tm@NaYF ₄ @PMAO/PEG	75	Imaging UCNP accumulation in tumor using amphiphilic polymer coating	Imaged in mouse lungs	975/Visible	[235]
NaYF ₄ : 18% Yb/0.6% Tm@NaYF ₄ @PMAO	75	Simultaneous bioimaging and local light-activated hyperthermia	Imaged near mouse shoulder	980/800	[87]
NaYF ₄ : 18% Yb/2% Er@SiO ₂ @AuNP@DNA hairpin	~75	DNA-functionalized UCNPs for biocompatibility, deep tissue imaging, and guided drug release	Imaged in mouse abdomen	980/750-830	[138]
NaYF ₄ : 30% Yb/1% Er@Cancer cell membrane	80	Cancer cell-coated UCNPs for tumor targeting and imaging	Imaged throughout mice	980/535	[164]
NaYF ₄ : 30% Yb/1% Er@RBC proteins	90	Erythrocyte membrane-coated UCNPs for increased biocompatibility	Imaged near mouse hip	980/535	[29]
NaYF ₄ : 20% Yb/2% Tm@NaYF ₄ @PEI@Colomnic acid	90	Colomnic acid prolongs circulation and enables blood vessel and inflammation imaging	Imaged in mouse blood vessels	975	[161]

NaYF ₄ : 20% Yb/0.5% Tm@NaGdF ₄ :Yb@g-C ₃ N ₄ /Au ₂₅ /PEG	110	Graphitic-phase carbon and gold nanocluster-mediated ROS generation for PDT & trimodal MRI/CT	Imaged in mouse shoulder (Supplemental)	980	[131]
NaYF ₄ : 20% Yb/2% Er@PEG/ ¹²⁵ I	120	SPECT/CT tracking of radiolabeled nanoparticles	Whole body SPECT	N/A	[158]
NaYF ₄ : 20% Yb/2% Tm@NaYF ₄ @PMAO/DARPin	213	DARPin-mediated targeting of HER2 positive cells in xenograft tumor	Imaged in mouse leg	980/485-831	[167]
NaYF ₄ : 18% Yb/2% Tm@NaYF ₄ : 21.4% Yb/21.4% Nd@CNQDs in nanobubbles	428	PDT through light-mediated carbon nitride quantum dot ROS generation and ultrasound-mediated release	Imaged near mouse hip	808/830+	[193]
In Vivo Targeting/Sensing					
NaGdF ₄ : 28% Yb/2% Er/10% Ce@PEG/cMBP	13	Targeting of overexpressed squamous cell cancer protein for multimodal diagnosis	N/A	808	[236]
NaF ₄ : 99.5% Er/0.5% Tm@NaYF ₄ @NaGdF ₄ : 15%Tb@Folic acid	17	X-ray activated PDT and tumor targeting	Imaged subcutaneous tumor	980	[157]
NaGdF ₄ : 35% Yb/0.5% Tm@NaGdF ₄ @PEG-FA/PC70	20	Fluorescent, UCL, & MRI imaging of tumor-targeted nanoparticles for PDT	Imaged near mouse hip	980	[98]
NaYF ₄ : 20% Yb/2% Er@polyglutamic dendron	23	Mapping mouse vasculature as well as pH sensing with low power excitation	0.2 mm	980, 808	[69]F
NaF ₄ : 15% Yb/85% Er@NaGdF ₄ :20% Yb@SiO ₂	23	Tumor targeting and comparison of peptide performance for colorectal cancer identification	Imaged in mouse colon	980/<675	[99]
NaF ₄ : 98% Er/2% Ho@NaYF ₄	24	Patch for <i>in vivo</i> sensing of H ₂ O ₂ and inflammation	Imaged UCNPs on dermal patch	1530/1180 & 980	[237]

NaGdF ₄ : 70% Yb/1% Tm@NaGdF ₄ @Poly-d-lysine/DNA	38	Specific MiRNA-enhanced luminescence for detection in mice	Imaged near mouse hip	980	[43]
NaYF ₄ : 20% Yb/2% Er@NaYF ₄ : 10% Yb/40% Nd@NaYF ₄ @PEG/ANG2	42	Passing through the blood-brain barrier and light-mediated endolysosomal escape for metronomic chemotherapy	Imaged in mouse brain	808 PDT. 980/<950	[54]
NaGdF ₄ : 18% Yb/2% Tm@NaGdF ₄ @Cancer Cell Membrane	48	Multimodal targeting and differentiation between triple negative and MCF7 breast cancer cells	Imaged near mouse rear	980/790	[141]
Na(Y ⁹⁰ Y)F ₄ : 20% Yb/0.6% Tm @PMAO@ DARPin-PE40	75	DARPin for targeted, 2200x synergistic therapeutic increase with PE40/radioactive yttrium-mediated therapeutics against HER2+ breast cancer cells.	Imaged in mouse thigh	980/485-831	[238]
NaYF ₄ : 18% Yb/2% Er/Mn@IR-780/mTHPC/ANG2	80	Targeted PDT of intravenously injected UCNP for glioblastoma treatment	Imaged in brain and excised organs	675/730-760	[178]
NaYF ₄ : 30% Yb/1% Er@Cancer cell membrane	80	Cancer cell-coated UCNP for tumor targeting and imaging	Imaged throughout mice	980/535	[164]
NaYF ₄ : 18% Yb/2% Er@NaGdF ₄ @PEG/CD326mAb	85	MRI/UCL to monitor antibody-dependent increase in UCNP uptake for pancreatic cancer detection	Imaged near mouse shoulder	980/650	[159]
NaGdF ₄ : 18% Yb/2% Tm/2% Ca@NaLuF ₄ @PEG/anti-HER mAb	115	SPECT/CT/UCL imaging for metastatic lymphnode detection, prolonged circulation, and tumor targeting	7.7 mm	980	[169]
NaYF ₄ : 5% Nd@BDM/PtTPBP	165	<i>In vivo</i> sensitive temperature sensing	5 mm	808, 638/485-575, 980-1300	[239]
NaYF ₄ : 20% Yb/2% Tm@NaYF ₄ @PMAO/DARPin	213	DARPin-mediated targeting of HER2 positive cells in xenograft tumor	Imaged in mouse leg	980/485-831	[167]
PdTPBP/(perylene or BPEA)@SiO ₂ @peptide	216	Multiple UCNP injection for single-excitation identification of two tumor types <i>in vivo</i>	Imaged near mice hips	635/515 or 475	[146]

Photodynamic Therapy					
NaF ₄ : 99.5% Er/0.5% Tm@NaYF ₄ @NaGdF ₄ : 15% Tb@Folic acid	17	X-ray activated PDT and tumor targeting	Imaged subcutaneous tumor	980	[157]
NaGdF ₄ : 35% Yb/0.5% Tm@NaGdF ₄ @PEG-FA/PC70	20	Fluorescent, UCL, & MRI imaging of tumor-targeted nanoparticles for PDT	Imaged near mouse hip	980/Not Listed	[98]
NaGdF ₄ : Yb/Er@Ce6/DNA	20	MRI/CT/UCL/PA Imaging-guided ce6-mediated PDT	Imaged near mouse hip	980	[225]
NaErF ₄ @NaYF ₄ @NaYbF ₄ : 0.5% Tm@NaYF ₄ @TiO ₂	40	Imaging-guided PDT using titanium dioxide-mediated ROS generation	Imaged in mouse chest	980 PDT, 808/Not listed	[17]
NaYF ₄ : 20% Yb/2% Er@NaYF ₄ :Yb@PDA/ICG	40	PDT of injected nanoparticles	N/A	808	[240]
NaYF ₄ : 20% Yb/2% Er@NaYF ₄ : 10% Yb/40% Nd@NaYF ₄ @PEG/ANG2	42	Passing through the blood-brain barrier and light-mediated endolysosomal escape for metronomic chemotherapy	Imaged in mouse brain	808 PDT. 980/<950	[54]
NaGdF ₄ : 20% Yb/2% Er@NaGdF ₄ : 30% Nd/10% Yb@IR-808@Ce6/MC540 SiO ₂	46	Dye sensitization for increased PDT with minimal heating effects & trimodal UCL/CT/MRI	MRI/CT near mouse shoulder	808	[241]
NaGdF ₄ : 18% Yb/2% Er/2% Co/3% Mn@SiO ₂ /FITC/CuS/ZnPc/DOX	48	CT/MRI multimodal imaging for PDT application	N/A	980	[242]
NaYF ₄ : 20% Yb/5% Gd/2% Er@NaYF ₄ @Ag ₂ Se QDs	62	Enhancement of PDT and luminescence activity through quantum dots	Imaged in mouse back	800	[103]
NaYF ₄ : 18% Yb/0.6% Tm@NaYF ₄ @PMAO	75	Simultaneous bioimaging and local light-activated hyperthermia	Imaged near mouse shoulder	980/800	[87]

NaYF ₄ : 18% Yb/2% Er@SiO ₂ @AuNP@DNA hairpin	~75	DNA-functionalized UCNPs for biocompatibility, deep tissue imaging, and guided drug release	Imaged in mouse abdomen	980/750-830	[138]
NaYF ₄ : 18% Yb/2% Er/Mn@IR-780/mTHPC/angiopep-2	80	Targeted PDT of intravenously injected UCNPs for glioblastoma treatment	Imaged in brain and excised organs	675/730-760	[178]
NaYF ₄ : 20% Yb/0.5% Tm@NaGdF ₄ :Yb@g-C ₃ N ₄ /Au ₂₅ /PEG	110	Graphitic-phase carbon and gold nanocluster-mediated ROS generation for PDT & trimodal MRI/CT	Imaged in mouse shoulder (Supplemental)	980	[131]
NaYF ₄ : 18% Yb/2% Tm@NaYF ₄ : 21.4% Yb/21.4% Nd@CNQDs in nanobubbles	428	PDT through light-mediated carbon nitride quantum dot ROS generation and ultrasound-mediated release	Imaged near mouse hip	808/830+	[193]
Multimodal Imaging					
NaGdF ₄ : 28% Yb/2% Er/10% Ce@PEG/cMBP	13	Targeting of overexpressed squamous cell cancer protein for multimodal diagnosis	N/A	808	[236]
NaGdF ₄ : 35% Yb/0.5% Tm@NaGdF ₄ @PEG-FA/PC70	20	Fluorescent, UCL, & MRI imaging of tumor-targeted nanoparticles for PDT	Imaged near mouse hip	980/Not Listed	[98]
NaGdF ₄ : Yb/Er@Ce6/DNA	20	MRI/CT/UCL/PA Imaging-guided ce6-mediated PDT	Imaged near mouse hip	980	[225]
NaGdF ₄ : 18% Yb/2% Er@PEG	21	Bimodal x-ray & UCL imaging to monitor consumed UCNP escape from digestive tract	Imaged in surgically removed organs	980/528-552	[168]
NaYF ₄ : 20% Yb/2% Er/1% Tm@GdCl ₃ @Aminocaproic Acid@ ¹⁸ F	30	Multimodal UCL/MRI/PET imaging	Imaged in mouse chest organs	980/800	[243]

NaGdF ₄ : 20% Yb/2% Er@BSA·DTPAGd	43	Strategies for gadolinium integration for MRI in mice	MRI only	N/A	[232]
NaGdF ₄ : 20% Yb/2% Er@NaGdF ₄ : 30% Nd/10% Yb@IR-808@Ce6/MC540 SiO ₂	46	Dye sensitization for increased PDT with minimal heating effects & trimodal UCL/CT/MRI	MRI/CT near mouse shoulder	808	[241]
NaGdF ₄ : 18% Yb/2% Tm@NaGdF ₄ @Cancer Cell Membrane	48	Multimodal targeting and differentiation between triple negative and MCF7 breast cancer cells	Imaged near mouse rear	980/790	[141]
NaGdF ₄ : 18% Yb/2% Er/2% Co/3% Mn@SiO ₂ /FITC/CuS/ZnPc/DOX	48	CT/MRI multimodal imaging for PDT application	N/A	980	[242]
NaYF ₄ : 18% Yb/2% Er@NaYF ₄ : 10% Yb@NaF ₄ : 90% Nd/10% Yb@NaYF ₄ @NaGdF ₄ @HDA-G2	54	Deep multimodal imaging through PAI, MRI, and UCL	Imaged in mouse rear, 25 mm experimental	800/<700	[55]
NaYF ₄ : 20% Yb/2% Er@NaYF ₄ : 10% Yb/30% Nd@SiO ₂ /ICG	62	Photoacoustic enhancement using UCNP/indocyanine green for mouse brain and depth imaging	Imaged mouse brain (PAI)	800	[192]
aYF ₄ : 18% Yb/2% Er@NaGdF ₄ @PEG/CD326mAb	85	MRI/UCL to monitor antibody-dependent increase in UCNP uptake for pancreatic cancer detection	Imaged near mouse shoulder	980/650	[159]
NaYF ₄ : 20% Yb/0.5% Tm@NaGdF ₄ :Yb@g-C ₃ N ₄ /Au ₂₅ /PEG	110	Graphitic-phase carbon and gold nanocluster-mediated ROS generation for PDT & trimodal MRI/CT	Imaged in mouse shoulder (Supplemental)	980	[131]

BiF ₃ : 20% Yb/2% Er	~110	Bimodal x-ray & UCL imaging	Imaged following intraperitoneal injection	980/<700	[63]
NaGdF ₄ : 18% Yb/2% Tm/2% Ca@NaLuF ₄ @PEG/anti-HER mAb	115	SPECT/CT/UCL imaging for metastatic lymph node detection, prolonged circulation, and tumor targeting	7.7 mm	980	[169]
NaYF ₄ : 20% Yb/2% Er@PEG/ ¹²⁵ I	120	SPECT/CT tracking of radiolabeled nanoparticles	Whole body SPECT	N/A	[158]

*Non-exhaustive list of uses of UCNPs in tissue/whole body imaging grouped by application in image enhancement, surface coating, *in vivo* targeting capabilities, photodynamic therapy, and multimodal imaging and organized by particle size. Publications applicable to multiple categories are listed multiple times. If papers used multiple particle architectures, the architecture and size used in the tissue/*in vivo* bioimaging application are listed in the table. In the excitation/emission wavelength column, if an imaging application uses multiple excitations or emissions, the wavelengths are separated by commas and a slash separates excitation from emission wavelengths.

b. Table 2: Reagents Used in Synthesis of Gold Nanoparticles of Varying Size

Size (nm)	Nanopure Water (mL)	25mM H ₂ AuCl ₄ (mL)	15mM tribasic sodium citrate (mL)	15 nm seeds (@ 2.4nM) (mL)	25 mM hydroquinone (mL)	Centrifuge speed (xg)
30	86.05	0.887	0.887	11.29	0.887	3500
45	93.75	0.967	0.967	3.35	0.967f.	2000
60	95.63	0.986	0.986	1.41	0.986	1200
80	96.42	0.994	0.994	0.595	0.994	900
100	96.7	0.997	0.997	0.305	0.997	750
150	96.91	0.999	0.999	0.09	0.999	180
200	96.96	0.999	0.999	0.038	0.999	100

c. Table 3: Characterization of Synthesized Nanoparticles

Size (nm)	30	45	60	80	100	150	200
DLS	25.7	44.4	61.6	67.2	96.3	178.3	246.9
PDI	0.033	0.081	0.077	0.069	0.074	0.041	0.089
TEM	14.5	29.3	47.3	63.1	77.2	160.9	210.1

8. References

- [1] D. Yang, C. Li, J. Lin, *Nanomed.* **2015**, *10*, 2573.
- [2] G. Liang, H. Wang, H. Shi, H. Wang, M. Zhu, A. Jing, J. Li, G. Li, *J. Nanobiotechnology* **2020**, *18*, 154.
- [3] B. P. Burke, C. Cawthorne, S. J. Archibald, *Philos. Trans. R. Soc. Math. Phys. Eng. Sci.* **2017**, *375*, 20170261.
- [4] O. S. Wolfbeis, *Chem. Soc. Rev.* **2015**, *44*, 4743.
- [5] S. Wilhelm, *ACS Nano* **2017**, *11*, 10644.
- [6] S. Wilhelm, M. Kaiser, C. Würth, J. Heiland, C. Carrillo-Carrion, V. Muhr, O. S. Wolfbeis, W. J. Parak, U. Resch-Genger, T. Hirsch, *Nanoscale* **2015**, *7*, 1403.
- [7] C. Würth, M. Kaiser, S. Wilhelm, B. Grauel, T. Hirsch, U. Resch-Genger, *Nanoscale* **2017**, *9*, 4283.
- [8] S. Wen, J. Zhou, K. Zheng, A. Bednarkiewicz, X. Liu, D. Jin, *Nat. Commun.* **2018**, *9*, 2415.
- [9] S. K. Murthy, *Int. J. Nanomedicine* **2007**, *2*, 129.
- [10] S. Wilhelm, *undefined* **2015**.
- [11] F. Xu, Y. Sun, H. Gao, S. Jin, Z. Zhang, H. Zhang, G. Pan, M. Kang, X. Ma, Y. Mao, *ACS Appl. Mater. Interfaces* **2021**, *13*, 2674.
- [12] S. Radunz, E. Andresen, C. Würth, A. Koerdt, H. R. Tschiche, U. Resch-Genger, *Anal. Chem.* **2019**, *91*, 7756.
- [13] M. Xu, X. Zou, Q. Su, W. Yuan, C. Cao, Q. Wang, X. Zhu, W. Feng, F. Li, *Nat. Commun.* **2018**, *9*, 2698.
- [14] M. del Barrio, R. Cases, V. Cebolla, T. Hirsch, S. de Marcos, S. Wilhelm, J. Galbán, *Talanta* **2016**, *160*, 586.
- [15] M. del Barrio, S. de Marcos, V. Cebolla, J. Heiland, S. Wilhelm, T. Hirsch, J. Galbán, *Biosens. Bioelectron.* **2014**, *59*, 14.
- [16] S. Wilhelm, M. del Barrio, J. Heiland, S. F. Himmelstoß, J. Galbán, O. S. Wolfbeis, T. Hirsch, *ACS Appl. Mater. Interfaces* **2014**, *6*, 15427.
- [17] J. Zuo, L. Tu, Q. Li, Y. Feng, I. Que, Y. Zhang, X. Liu, B. Xue, L. J. Cruz, Y. Chang, H. Zhang, X. Kong, *ACS Nano* **2018**, *12*, 3217.
- [18] Z. Qiu, J. Shu, D. Tang, *Anal. Chem.* **2018**, *90*, 1021.
- [19] Z. Farka, M. J. Mickert, A. Hlaváček, P. Skládal, H. H. Gorris, *Anal. Chem.* **2017**, *89*, 11825.
- [20] Y. Pan, J. Yang, X. Luan, X. Liu, X. Li, J. Yang, T. Huang, L. Sun, Y. Wang, Y. Lin, Y. Song, *Sci. Adv.* **2019**, *5*, eaav7199.
- [21] Y. Ma, J. Bao, Y. Zhang, Z. Li, X. Zhou, C. Wan, L. Huang, Y. Zhao, G. Han, T. Xue, *Cell* **2019**, *177*, 243.
- [22] X. Wu, G. Chen, J. Shen, Z. Li, Y. Zhang, G. Han, *Bioconjug. Chem.* **2015**, *26*, 166.
- [23] A. Bednarkiewicz, E. M. Chan, A. Kotulska, L. Marciniak, K. Prorok, *Nanoscale Horiz.* **2019**, *4*, 881.
- [24] S. D. Camillis, P. Ren, Y. Cao, M. Plöschner, D. Denkova, X. Zheng, Y. Lu, J. A. Piper, *Nanoscale* **2020**, *12*, 20347.
- [25] B. Liu, J. Liao, Y. Song, C. Chen, L. Ding, J. Lu, J. Zhou, F. Wang, *Nanoscale Adv.* **2022**, *4*, 30.
- [26] F. Wang, X. Liu, *Acc. Chem. Res.* **2014**, *47*, 1378.

- [27] M. I. Saleh, B. Rühle, S. Wang, J. Radnik, Y. You, U. Resch-Genger, *Sci. Rep.* **2020**, *10*, 19318.
- [28] E. L. Guryev, A. S. Smyshlyaeva, N. Y. Shilyagina, E. A. Sokolova, S. Shanwar, A. B. Kostyuk, A. V. Lyubeshkin, A. A. Schulga, E. V. Konovalova, Q. Lin, I. Roy, I. V. Balalaeva, S. M. Deyev, A. V. Zvyagin, *Mol. Basel Switz.* **2020**, *25*, E4302.
- [29] L. Rao, Q.-F. Meng, L.-L. Bu, B. Cai, Q. Huang, Z.-J. Sun, W.-F. Zhang, A. Li, S.-S. Guo, W. Liu, T.-H. Wang, X.-Z. Zhao, *ACS Appl. Mater. Interfaces* **2017**, *9*, 2159.
- [30] V. Muhr, S. Wilhelm, T. Hirsch, O. S. Wolfbeis, *Acc. Chem. Res.* **2014**, *47*, 3481.
- [31] J. Rieffel, F. Chen, J. Kim, G. Chen, W. Shao, S. Shao, U. Chitgupi, R. Hernandez, S. A. Graves, R. J. Nickles, P. N. Prasad, C. Kim, W. Cai, J. F. Lovell, *Adv. Mater.* **2015**, *27*, 1785.
- [32] P. Sarder, D. Maji, S. Achilefu, *Bioconjug. Chem.* **2015**, *26*, 963.
- [33] M. Zhang, J. Yue, R. Cui, Z. Ma, H. Wan, F. Wang, S. Zhu, Y. Zhou, Y. Kuang, Y. Zhong, D.-W. Pang, H. Dai, *Proc. Natl. Acad. Sci.* **2018**, *115*, 6590.
- [34] G. Yuan, D. E. Gómez, N. Kirkwood, K. Boldt, P. Mulvaney, *ACS Nano* **2018**, *12*, 3397.
- [35] S. F. Himmelstoß, T. Hirsch, *Methods Appl. Fluoresc.* **2019**, *7*, 022002.
- [36] A. Gulzar, J. Xu, P. Yang, F. He, L. Xu, *Nanoscale* **2017**, *9*, 12248.
- [37] X. Zhu, X. Liu, H. Zhang, M. Zhao, P. Pei, Y. Chen, Y. Yang, L. Lu, P. Yu, C. Sun, J. Ming, I. M. Abraham, A. M. El-Toni, A. Khan, F. Zhang, *Angew. Chem. Int. Ed.* **2021**, *60*, 23545.
- [38] B. Zhou, L. Yan, J. Huang, X. Liu, L. Tao, Q. Zhang, *Nat. Photonics* **2020**, *14*, 760.
- [39] T. Sun, Y. Li, W. L. Ho, Q. Zhu, X. Chen, L. Jin, H. Zhu, B. Huang, J. Lin, B. E. Little, S. T. Chu, F. Wang, *Nat. Commun.* **2019**, *10*, 1811.
- [40] D. Przybylska, A. Ekner-Grzyb, B. F. Grześkowiak, T. Grzyb, *Sci. Rep.* **2019**, *9*, 8669.
- [41] Y. Liu, Y. Lu, X. Yang, X. Zheng, S. Wen, F. Wang, X. Vidal, J. Zhao, D. Liu, Z. Zhou, C. Ma, J. Zhou, J. A. Piper, P. Xi, D. Jin, *Nature* **2017**, *543*, 229.
- [42] B. Liu, C. Chen, X. Di, J. Liao, S. Wen, Q. P. Su, X. Shan, Z.-Q. Xu, L. A. Ju, C. Mi, F. Wang, D. Jin, *Nano Lett.* **2020**, *20*, 4775.
- [43] J. Zhao, H. Chu, Y. Zhao, Y. Lu, L. Li, *J. Am. Chem. Soc.* **2019**, *141*, 7056.
- [44] C. Ash, M. Dubec, K. Donne, T. Bashford, *Lasers Med. Sci.* **2017**, *32*, 1909.
- [45] S. Sindhvani, A. M. Syed, S. Wilhelm, W. C. W. Chan, *Bioconjug. Chem.* **2017**, *28*, 253.
- [46] A. M. Syed, P. MacMillan, J. Ngai, S. Wilhelm, S. Sindhvani, B. R. Kingston, J. L. Y. Wu, P. Llano-Suárez, Z. P. Lin, B. Ouyang, Z. Kahiel, S. Gadde, W. C. W. Chan, *Nano Lett.* **2020**, *20*, 1362.
- [47] A. M. Syed, S. Sindhvani, S. Wilhelm, B. R. Kingston, D. S. W. Lee, J. L. Gommerman, W. C. W. Chan, *J. Am. Chem. Soc.* **2017**, *139*, 9961.
- [48] S. Sindhvani, A. M. Syed, S. Wilhelm, D. R. Glancy, Y. Y. Chen, M. Dobosz, W. C. W. Chan, *ACS Nano* **2016**, *10*, 5468.
- [49] S. Wäldchen, J. Lehmann, T. Klein, S. van de Linde, M. Sauer, *Sci. Rep.* **2015**, *5*, 15348.
- [50] G. Chen, Y. Cao, Y. Tang, X. Yang, Y. Liu, D. Huang, Y. Zhang, C. Li, Q. Wang, *Adv. Sci.* **2020**, *7*, 1903783.
- [51] G. Chen, H. Qiu, P. N. Prasad, X. Chen, *Chem. Rev.* **2014**, *114*, 5161.
- [52] D. E. Hudson, D. O. Hudson, J. M. Wininger, B. D. Richardson, *Photomed. Laser Surg.* **2013**, *31*, 163.
- [53] G. Tian, Z. Gu, L. Zhou, W. Yin, X. Liu, L. Yan, S. Jin, W. Ren, G. Xing, S. Li, Y. Zhao, *Adv. Mater.* **2012**, *24*, 1226.

- [54] M. J. Y. Ang, J. Yoon, M. Zhou, H.-L. Wei, Y. Y. Goh, Z. Li, J. Feng, H. Wang, Q. Su, D. S. T. Ong, X. Liu, *Adv. Mater.* **2022**, *34*, 2106194.
- [55] Y. Liu, N. Kang, J. Lv, Z. Zhou, Q. Zhao, L. Ma, Z. Chen, L. Ren, L. Nie, *Adv. Mater.* **2016**, *28*, 6411.
- [56] H. Dong, L.-D. Sun, W. Feng, Y. Gu, F. Li, C.-H. Yan, *ACS Nano* **2017**, *11*, 3289.
- [57] X. Zheng, X. Zhu, Y. Lu, J. Zhao, W. Feng, G. Jia, F. Wang, F. Li, D. Jin, *Anal. Chem.* **2016**, *88*, 3449.
- [58] Y. Wu, J. Xu, E. T. Poh, L. Liang, H. Liu, J. K. W. Yang, C.-W. Qiu, R. A. L. Vallée, X. Liu, *Nat. Nanotechnol.* **2019**, *14*, 1110.
- [59] W. Zheng, P. Huang, Z. Gong, D. Tu, J. Xu, Q. Zou, R. Li, W. You, J.-C. G. Bünzli, X. Chen, *Nat. Commun.* **2018**, *9*, 3462.
- [60] Y. Lu, J. Zhao, R. Zhang, Y. Liu, D. Liu, E. M. Goldys, X. Yang, P. Xi, A. Sunna, J. Lu, Y. Shi, R. C. Leif, Y. Huo, J. Shen, J. A. Piper, J. P. Robinson, D. Jin, *Nat. Photonics* **2014**, *8*, 32.
- [61] A. B. Kostyuk, A. D. Vorotnov, A. V. Ivanov, A. B. Volovetskiy, A. V. Kruglov, L. M. Sencha, L. Liang, E. L. Guryev, V. A. Vodeneev, S. M. Deyev, Y. Lu, A. V. Zvyagin, *Nano Res.* **2019**, *12*, 2933.
- [62] X. Liu, Z.-H. Chen, H. Zhang, Y. Fan, F. Zhang, *Angew. Chem.* **2021**, *133*, 7117.
- [63] X. Yan, T. Li, L. Guo, H. Li, P. Chen, M. Liu, *RSC Adv.* **2019**, *9*, 10889.
- [64] R. Deng, F. Qin, R. Chen, W. Huang, M. Hong, X. Liu, *Nat. Nanotechnol.* **2015**, *10*, 237.
- [65] J. Zuo, Q. Li, B. Xue, C. Li, Y. Chang, Y. Zhang, X. Liu, L. Tu, H. Zhang, X. Kong, *Nanoscale* **2017**, *9*, 7941.
- [66] Y. Wu, J. Xu, X. Qin, J. Xu, X. Liu, *Nat. Commun.* **2021**, *12*, 2022.
- [67] Z. Zhang, M. K. G. Jayakumar, S. Shikha, Y. Zhang, X. Zheng, Y. Zhang, *ACS Appl. Mater. Interfaces* **2020**, *12*, 12549.
- [68] B. Krajnik, L. W. Golacki, U. Kostiv, D. Horák, A. Podhorodecki, *ACS Omega* **2020**, *5*, 26537.
- [69] T. V. Esipova, X. Ye, J. E. Collins, S. Sakadžić, E. T. Mandeville, C. B. Murray, S. A. Vinogradov, *Proc. Natl. Acad. Sci.* **2012**, *109*, 20826.
- [70] N. Bagheri, Q. Liu, J. Bergstrand, R. Pu, Q. Zhan, M. H. M. Ara, H. Ågren, H. Liu, J. Widengren, *Opt. Mater.* **2019**, *97*, 109389.
- [71] N. D. Donahue, E. R. Francek, E. Kiyotake, E. E. Thomas, W. Yang, L. Wang, M. S. Detamore, S. Wilhelm, *Anal. Bioanal. Chem.* **2020**, *412*, 5205.
- [72] N. D. Donahue, S. Kanapilly, C. Stephan, M. C. Marlin, E. R. Francek, M. Haddad, J. Guthridge, S. Wilhelm, *Nano Lett.* **2022**, *22*, 294.
- [73] F. Wang, S. Wen, H. He, B. Wang, Z. Zhou, O. Shimoni, D. Jin, *Light Sci. Appl.* **2018**, *7*, 18007.
- [74] J.-M. Rabanel, V. Adibnia, S. F. Tehrani, S. Sanche, P. Hildgen, X. Banquy, C. Ramassamy, *Nanoscale* **2019**, *11*, 383.
- [75] N. D. Donahue, H. Acar, S. Wilhelm, *Adv. Drug Deliv. Rev.* **2019**, *143*, 68.
- [76] C. Würth, S. Fischer, B. Grauel, A. P. Alivisatos, U. Resch-Genger, *J. Am. Chem. Soc.* **2018**, *140*, 4922.
- [77] Y. Zheng, Q. Li, J. Wu, Z. Luo, W. Zhou, A. Li, Y. Chen, T. Rouzi, T. Tian, H. Zhou, X. Zeng, Y. Li, X. Cheng, Y. Wei, Z. Deng, F. Zhou, X. Hong, *Chem. Sci.* **2021**, *12*, 1843.
- [78] Y. Zhong, Z. Ma, S. Zhu, J. Yue, M. Zhang, A. L. Antaris, J. Yuan, R. Cui, H. Wan, Y. Zhou, W. Wang, N. F. Huang, J. Luo, Z. Hu, H. Dai, *Nat. Commun.* **2017**, *8*, 737.

- [79] Y. Zhong, Z. Ma, F. Wang, X. Wang, Y. Yang, Y. Liu, X. Zhao, J. Li, H. Du, M. Zhang, Q. Cui, S. Zhu, Q. Sun, H. Wan, Y. Tian, Q. Liu, W. Wang, K. C. Garcia, H. Dai, *Nat. Biotechnol.* **2019**, *37*, 1322.
- [80] A. P. Demchenko, *Methods Appl. Fluoresc.* **2020**, *8*, 022001.
- [81] J. Bailes, *Methods Mol. Biol. Clifton NJ* **2020**, *2118*, 343.
- [82] R. An, F. Zhang, X. Zou, Y. Tang, M. Liang, I. Oshchapovskyy, Y. Liu, A. Honarfar, Y. Zhong, C. Li, H. Geng, J. Chen, S. E. Canton, T. Pullerits, K. Zheng, *ACS Appl. Mater. Interfaces* **2018**, *10*, 39222.
- [83] D. Song, M. Zhu, S. Chi, L. Xia, Z. Li, Z. Liu, *Anal. Chem.* **2021**, *93*, 7949.
- [84] S. Wu, G. Han, D. J. Milliron, S. Aloni, V. Altoe, D. V. Talapin, B. E. Cohen, P. J. Schuck, *Proc. Natl. Acad. Sci.* **2009**, *106*, 10917.
- [85] Q. Wu, B. Huang, X. Peng, S. He, Q. Zhan, *Opt. Express* **2017**, *25*, 30885.
- [86] S. H. Nam, Y. M. Bae, Y. I. Park, J. H. Kim, H. M. Kim, J. S. Choi, K. T. Lee, T. Hyeon, Y. D. Suh, *Angew. Chem. Int. Ed.* **2011**, *50*, 6093.
- [87] I. V. Krylov, R. A. Akasov, V. V. Rocheva, N. V. Sholina, D. A. Khochenkov, A. V. Nechaev, N. V. Melnikova, A. A. Dmitriev, A. V. Ivanov, A. N. Generalova, E. V. Khaydukov, *Front. Chem.* **2020**, *8*, 295.
- [88] Q. Liu, Y. Zhang, C. S. Peng, T. Yang, L.-M. Joubert, S. Chu, *Nat. Photonics* **2018**, *12*, 548.
- [89] Q. Lin, L. Wang, Z. Li, H. Shen, L. Guo, Y. Kuang, H. Wang, L. S. Li, *ACS Photonics* **2018**, *5*, 939.
- [90] K. Rurack, M. Spieles, *Anal. Chem.* **2011**, *83*, 1232.
- [91] H. Jia, Z. Wang, T. Yuan, F. Yuan, X. Li, Y. Li, Z. Tan, L. Fan, S. Yang, *Adv. Sci.* **2019**, *6*, 1900397.
- [92] H. Li, M. Tan, X. Wang, F. Li, Y. Zhang, L. Zhao, C. Yang, G. Chen, *J. Am. Chem. Soc.* **2020**, *142*, 2023.
- [93] C. M. S. Jones, D. Biner, S. Misopoulos, K. W. Krämer, J. Marques-Hueso, *Sci. Rep.* **2021**, *11*, 13910.
- [94] B. Chen, F. Wang, *Acc. Chem. Res.* **2020**, *53*, 358.
- [95] N. J. J. Johnson, S. He, S. Diao, E. M. Chan, H. Dai, A. Almutairi, *J. Am. Chem. Soc.* **2017**, *139*, 3275.
- [96] O. Dukhno, F. Przybilla, V. Muhr, M. Buchner, T. Hirsch, Y. Mély, *Nanoscale* **2018**, *10*, 15904.
- [97] B. Shen, S. Cheng, Y. Gu, D. Ni, Y. Gao, Q. Su, W. Feng, F. Li, *Nanoscale* **2017**, *9*, 1964.
- [98] M. Guan, H. Dong, J. Ge, D. Chen, L. Sun, S. Li, C. Wang, C. Yan, P. Wang, C. Shu, *NPG Asia Mater.* **2015**, *7*, e205.
- [99] X. Li, L. Liu, Y. Fu, H. Chen, M. M. A. Abualrejal, H. Zhang, Z. Wang, H. Zhang, *Acta Biomater.* **2020**, *104*, 167.
- [100] Q. Feng, W. Zheng, J. Pu, Q. Chen, W. Shao, *Front. Chem.* **2021**, *9*, 342.
- [101] X. Xu, C. Clarke, C. Ma, G. Casillas, M. Das, M. Guan, D. Liu, L. Wang, A. Tadich, Y. Du, C. Ton-That, D. Jin, *Nanoscale* **2017**, *9*, 7719.
- [102] M. D. Wisser, S. Fischer, C. Siefe, A. P. Alivisatos, A. Salleo, J. A. Dionne, *Nano Lett.* **2018**, *18*, 2689.
- [103] D. Song, S. Chi, X. Li, C. Wang, Z. Li, Z. Liu, *ACS Appl. Mater. Interfaces* **2019**, *11*, 41100.
- [104] D. Song, M. Zhu, S. Chi, L. Xia, Z. Li, Z. Liu, *Anal. Chem.* **2021**, *93*, 7949.

- [105] C. Hazra, S. Ullah, Y. E. S. Correales, L. G. Caetano, S. J. L. Ribeiro, *J. Mater. Chem. C* **2018**, *6*, 4777.
- [106] R. Lv, Y. Wang, B. Lin, X. Peng, J. Liu, W. Lü, J. Tian, *Anal. Chem.* **2021**, *93*, 4984.
- [107] H. Zhou, X. Zeng, A. Li, W. Zhou, L. Tang, W. Hu, Q. Fan, X. Meng, H. Deng, L. Duan, Y. Li, Z. Deng, X. Hong, Y. Xiao, *Nat. Commun.* **2020**, *11*, 6183.
- [108] H. Xu, Y. Yang, L. Lu, Y. Yang, Z. Zhang, C.-X. Zhao, F. Zhang, Y. Fan, *Anal. Chem.* **2022**, *94*, 3661.
- [109] Q. Jia, L. Ma, X. Zhai, W. Fu, Y. Liu, X. Liao, J. Zhou, *Anal. Chem.* **2020**, *92*, 14762.
- [110] Y. Fan, P. Wang, Y. Lu, R. Wang, L. Zhou, X. Zheng, X. Li, J. A. Piper, F. Zhang, *Nat. Nanotechnol.* **2018**, *13*, 941.
- [111] Y. Yang, D. Tu, Y. Zhang, P. Zhang, X. Chen, *iScience* **2021**, *24*, 102062.
- [112] L. M. Jin, X. Chen, C. K. Siu, F. Wang, S. F. Yu, *ACS Nano* **2017**, *11*, 843.
- [113] S. Ram, E. S. Ward, R. J. Ober, *Proc. Natl. Acad. Sci.* **2006**, *103*, 4457.
- [114] M. A. Lauterbach, *Opt. Nanoscopy* **2012**, *1*, 8.
- [115] J. J. Field, K. A. Wernsing, S. R. Domingue, A. M. A. Motz, K. F. DeLuca, D. H. Levi, J. G. DeLuca, M. D. Young, J. A. Squier, R. A. Bartels, *Proc. Natl. Acad. Sci.* **2016**, *113*, 6605.
- [116] K. I. Willig, B. Harke, R. Medda, S. W. Hell, *Nat. Methods* **2007**, *4*, 915.
- [117] X. Peng, B. Huang, R. Pu, H. Liu, T. Zhang, J. Widengren, Q. Zhan, H. Ågren, *Nanoscale* **2019**, *11*, 1563.
- [118] C. Chen, F. Wang, S. Wen, Q. P. Su, M. C. L. Wu, Y. Liu, B. Wang, D. Li, X. Shan, M. Kianinia, I. Aharonovich, M. Toth, S. P. Jackson, P. Xi, D. Jin, *Nat. Commun.* **2018**, *9*, 3290.
- [119] C. Chen, B. Liu, Y. Liu, J. Liao, X. Shan, F. Wang, D. Jin, *Adv. Mater.* **2021**, *33*, 2008847.
- [120] Y. Liu, F. Wang, H. Lu, G. Fang, S. Wen, C. Chen, X. Shan, X. Xu, L. Zhang, M. Stenzel, D. Jin, *Small* **2020**, *16*, 1905572.
- [121] D. Denkova, M. Ploschner, M. Das, L. M. Parker, X. Zheng, Y. Lu, A. Orth, N. H. Packer, J. A. Piper, *Nat. Commun.* **2019**, *10*, 3695.
- [122] R. Heintzmann, T. Huser, *Chem. Rev.* **2017**, *117*, 13890.
- [123] E. S. Levy, C. A. Tajon, T. S. Bischof, J. Iafrati, A. Fernandez-Bravo, D. J. Garfield, M. Chamanzar, M. M. Maharbiz, V. S. Sohal, P. J. Schuck, B. E. Cohen, E. M. Chan, *ACS Nano* **2016**, *10*, 8423.
- [124] A. Fernandez-Bravo, K. Yao, E. S. Barnard, N. J. Borys, E. S. Levy, B. Tian, C. A. Tajon, L. Moretti, M. V. Altoe, S. Aloni, K. Beketayev, F. Scotognella, B. E. Cohen, E. M. Chan, P. J. Schuck, *Nat. Nanotechnol.* **2018**, *13*, 572.
- [125] W. Ren, S. Wen, S. Abdulkader Tawfik, Q. P. Su, G. Lin, L. A. Ju, M. J. Ford, H. Ghodke, A. M. van Oijen, D. Jin, *Chem. Sci.* **2018**, *9*, 4352.
- [126] M. J. Rust, M. Bates, X. Zhuang, *Nat. Methods* **2006**, *3*, 793.
- [127] R. Strack, *Nat. Methods* **2018**, *15*, 407.
- [128] H. Wang, Y. Rivenson, Y. Jin, Z. Wei, R. Gao, H. Günaydın, L. A. Bentolila, C. Kural, A. Ozcan, *Nat. Methods* **2019**, *16*, 103.
- [129] S. Plunkett, M. E. Khatib, İ. Şencan, J. E. Porter, A. T. N. Kumar, J. E. Collins, S. Sakadžić, S. A. Vinogradov, *Nanoscale* **2020**, *12*, 2657.
- [130] I. Khan, E. Tang, P. Arany, *Sci. Rep.* **2015**, *5*, 10581.

- [131] L. Feng, F. He, Y. Dai, B. Liu, G. Yang, S. Gai, N. Niu, R. Lv, C. Li, P. Yang, *ACS Appl. Mater. Interfaces* **2017**, *9*, 12993.
- [132] Z. Zhang, M. K. G. Jayakumar, X. Zheng, S. Shikha, Y. Zhang, A. Bansal, D. J. J. Poon, P. L. Chu, E. L. L. Yeo, M. L. K. Chua, S. K. Chee, Y. Zhang, *Nat. Commun.* **2019**, *10*, 4586.
- [133] D. Zhang, L. Wei, M. Zhong, L. Xiao, H.-W. Li, J. Wang, *Chem. Sci.* **2018**, *9*, 5260.
- [134] S. Y. Lee, R. Lee, E. Kim, S. Lee, Y. I. Park, *Front. Bioeng. Biotechnol.* **2020**, *8*, 275.
- [135] K.-Y. Pham, L.-C. Wang, C.-C. Hsieh, Y.-P. Hsu, L.-C. Chang, W.-P. Su, Y.-H. Chien, C.-S. Yeh, *J. Mater. Chem. B* **2021**, *9*, 694.
- [136] P. Rodríguez-Sevilla, Y. Zhang, P. Haro-González, F. Sanz-Rodríguez, F. Jaque, J. G. Solé, X. Liu, D. Jaque, *Adv. Mater.* **2016**, *28*, 2421.
- [137] O. A. Savchuk, J. J. Carvajal, C. D. S. Brites, L. D. Carlos, M. Aguiló, F. Diaz, *Nanoscale* **2018**, *10*, 6602.
- [138] S. Han, A. Samanta, X. Xie, L. Huang, J. Peng, S. J. Park, D. B. L. Teh, Y. Choi, Y.-T. Chang, A. H. All, Y. Yang, B. Xing, X. Liu, *Adv. Mater. Deerfield Beach Fla* **2017**, *29*, DOI 10.1002/adma.201704811.
- [139] Q. Zhan, H. Liu, B. Wang, Q. Wu, R. Pu, C. Zhou, B. Huang, X. Peng, H. Ågren, S. He, *Nat. Commun.* **2017**, *8*, 1058.
- [140] J.-H. Wang, H.-Y. Chen, C.-C. Chuang, J.-C. Chen, *RSC Adv.* **2020**, *10*, 41013.
- [141] H. Fang, M. Li, Q. Liu, Y. Gai, L. Yuan, S. Wang, X. Zhang, M. Ye, Y. Zhang, M. Gao, Y. Hou, X. Lan, *Nano-Micro Lett.* **2020**, *12*, 62.
- [142] S. F. Himmelstoß, T. Hirsch, *Part. Part. Syst. Charact.* **2019**, *36*, 1900235.
- [143] S. Wilhelm, T. Hirsch, W. M. Patterson, E. Scheucher, T. Mayr, O. S. Wolfbeis, *Theranostics* **2013**, *3*, 239.
- [144] R. Wei, Z. Wei, L. Sun, J. Z. Zhang, J. Liu, X. Ge, L. Shi, *ACS Appl. Mater. Interfaces* **2016**, *8*, 400.
- [145] C. Drees, A. N. Raj, R. Kurre, K. B. Busch, M. Haase, J. Piehler, *Angew. Chem. Int. Ed.* **2016**, *55*, 11668.
- [146] O. S. Kwon, H. S. Song, J. Conde, H. Kim, N. Artzi, J.-H. Kim, *ACS Nano* **2016**, *10*, 1512.
- [147] L. Rodriguez-Lorenzo, K. Fytianos, F. Blank, C. von Garnier, B. Rothen-Rutishauser, A. Petri-Fink, *Small Weinh. Bergstr. Ger.* **2014**, *10*, 1341.
- [148] P. Àlamo, V. Pallarès, M. V. Céspedes, A. Falgàs, J. M. Sanchez, N. Serna, L. Sánchez-García, E. Voltà-Duràn, G. A. Morris, A. Sánchez-Chardi, I. Casanova, R. Manges, E. Vazquez, A. Villaverde, U. Unzueta, *Pharmaceutics* **2020**, *12*, 1004.
- [149] M. B. Liisberg, S. Lahtinen, A. B. Sloth, T. Soukka, T. Vosch, *J. Am. Chem. Soc.* **2021**, *143*, 19399.
- [150] O. Ehlert, R. Thomann, M. Darbandi, T. Nann, *ACS Nano* **2008**, *2*, 120.
- [151] S. Chen, A. Weitemier, X. Zeng, L. He, X. Wang, Y. Tao, A. Huang, Y. Hashimoto-dani, M. Kano, H. Iwasaki, L. K. Parajuli, S. Okabe, D. B. L. Teh, A. H. All, I. Tsutsui-Kimura, K. F. Tanaka, X. Liu, T. McHugh, *Science* **2018**, *359*, 679.
- [152] Y. Zhang, L. M. Wiesholler, H. Rabie, P. Jiang, J. Lai, T. Hirsch, K.-B. Lee, *ACS Appl. Mater. Interfaces* **2020**, *12*, 40031.
- [153] F. Wang, B. Chen, B. Yan, Y. Yin, L. Hu, Y. Liang, M. Song, G. Jiang, *J. Am. Chem. Soc.* **2019**, *141*, 14043.
- [154] A. Priyam, N. M. Idris, Y. Zhang, *J. Mater. Chem.* **2011**, *22*, 960.

- [155] D. Li, W.-Y. Lai, Q. Shao, W. Huang, *RSC Adv.* **2017**, *7*, 11491.
- [156] P. Thanasekaran, C.-H. Chu, S.-B. Wang, K.-Y. Chen, H.-D. Gao, M. M. Lee, S.-S. Sun, J.-P. Li, J.-Y. Chen, J.-K. Chen, Y.-H. Chang, H.-M. Lee, *ACS Appl. Mater. Interfaces* **2019**, *11*, 84.
- [157] Y. Feng, X. Liu, Q. Li, S. Mei, K. Wu, J. Yuan, L. Tu, I. Que, F. Tamburini, F. Baldazzi, A. Chan, L. J. Cruz, J. Zuo, C. Yao, H. Zhang, *J. Mater. Chem. C* **2021**, *10*, 688.
- [158] U. Kostiv, V. Lobaz, J. Kučka, P. Švec, O. Sedláček, M. Hrubý, O. Janoušková, P. Francová, V. Kolářová, L. Šefc, D. Horák, *Nanoscale* **2017**, *9*, 16680.
- [159] Y. Han, Y. An, G. Jia, X. Wang, C. He, Y. Ding, Q. Tang, *J. Nanobiotechnology* **2018**, *16*, 7.
- [160] W. Yang, L. Wang, E. M. Mettenbrink, P. L. DeAngelis, S. Wilhelm, *Annu. Rev. Pharmacol. Toxicol.* **2021**, *61*, 269.
- [161] P. A. Demina, N. V. Sholina, R. A. Akasov, D. A. Khochenkov, N. A. Arkharova, A. V. Nechaev, E. V. Khaydukov, A. N. Generalova, *Biomater. Sci.* **2020**, *8*, 4570.
- [162] R. Lane, M. Haller, A. Chavarroche, A. Almond, P. L. DeAngelis, *Glycobiology* **2017**, *27*, 1062.
- [163] W. Yang, L. Wang, M. Fang, V. Sheth, Y. Zhang, A. M. Holden, N. D. Donahue, D. E. Green, A. N. Frickenstein, E. M. Mettenbrink, T. A. Schwemley, E. R. Francek, M. Haddad, M. N. Hossen, S. Mukherjee, S. Wu, P. L. DeAngelis, S. Wilhelm, *Nano Lett.* **2022**, *22*, 2103.
- [164] L. Rao, L.-L. Bu, B. Cai, J.-H. Xu, A. Li, W.-F. Zhang, Z.-J. Sun, S.-S. Guo, W. Liu, T.-H. Wang, X.-Z. Zhao, *Adv. Mater.* **2016**, *28*, 3460.
- [165] W. Poon, Y.-N. Zhang, B. Ouyang, B. R. Kingston, J. L. Y. Wu, S. Wilhelm, W. C. W. Chan, *ACS Nano* **2019**, *13*, 5785.
- [166] P. Peng, N. Wu, L. Ye, F. Jiang, W. Feng, F. Li, Y. Liu, M. Hong, *ACS Nano* **2020**, *14*, 16672.
- [167] E. L. Guryev, N. Y. Shilyagina, A. B. Kostyuk, L. M. Sencha, I. V. Balalaeva, V. A. Vodeneev, O. M. Kutova, A. V. Lyubeshkin, R. I. Yakubovskaya, A. A. Pankratov, F. I. Ingel, T. S. Novik, S. M. Deyev, S. A. Ermilov, A. V. Zvyagin, *Toxicol. Sci.* **2019**, *170*, 123.
- [168] Z. Chen, X. Wu, S. Hu, P. Hu, H. Yan, Z. Tang, Y. Liu, *MedChemComm* **2017**, *8*, 1053.
- [169] S. Qiu, J. Zeng, Y. Hou, L. Chen, J. Ge, L. Wen, C. Liu, Y. Zhang, R. Zhu, M. Gao, *Nanoscale* **2018**, *10*, 21772.
- [170] B. Tian, A. Fernandez-Bravo, H. Najafiaghdam, N. A. Torquato, M. V. P. Altoe, A. Teitelboim, C. A. Tajon, Y. Tian, N. J. Borys, E. S. Barnard, M. Anwar, E. M. Chan, P. J. Schuck, B. E. Cohen, *Nat. Commun.* **2018**, *9*, 3082.
- [171] S. Golovynskyi, I. Golovynska, L. I. Stepanova, O. I. Datsenko, L. Liu, J. Qu, T. Y. Ohulchansky, *J. Biophotonics* **2018**, *11*, e201800141.
- [172] L. M. Wiesholler, F. Frenzel, B. Grauel, C. Würth, U. Resch-Genger, T. Hirsch, *Nanoscale* **2019**, *11*, 13440.
- [173] S. Wang, L. Liu, Y. Fan, A. M. El-Toni, M. S. Alhoshan, D. li, F. Zhang, *Nano Lett.* **2019**, *19*, 2418.
- [174] H. Liu, C. T. Xu, G. Dumlupinar, O. B. Jensen, P. E. Andersen, S. Andersson-Engels, *Nanoscale* **2013**, *5*, 10034.
- [175] A. Barbora, O. Bohar, A. A. Sivan, E. Magory, A. Nause, R. Minnes, *PLOS ONE* **2021**, *16*, e0245350.

- [176] Z.-H. Hsieh, C.-H. Fan, Y.-J. Ho, M.-L. Li, C.-K. Yeh, *Sci. Rep.* **2020**, *10*, 17406.
- [177] L. Liang, Y. Lu, R. Zhang, A. Care, T. A. Ortega, S. M. Deyev, Y. Qian, A. V. Zvyagin, *Acta Biomater.* **2017**, *51*, 461.
- [178] Y.-C. Tsai, P. Vijayaraghavan, W.-H. Chiang, H.-H. Chen, T.-I. Liu, M.-Y. Shen, A. Omoto, M. Kamimura, K. Soga, H.-C. Chiu, *Theranostics* **2018**, *8*, 1435.
- [179] S. Wilhelm, A. Tavares, Q. Dai, S. Ohta, J. Audet, H. Dvorak, W. Chan, *Nat. Rev. Mater.* **n.d.**, *1*, 16014.
- [180] Y. Huai, M. N. Hossen, S. Wilhelm, R. Bhattacharya, P. Mukherjee, *Bioconjug. Chem.* **2019**, *30*, 2247.
- [181] Q. Dai, S. Wilhelm, D. Ding, A. M. Syed, S. Sindhvani, Y. Zhang, Y. Y. Chen, P. MacMillan, W. C. W. Chan, *ACS Nano* **2018**, *12*, 8423.
- [182] S. Sindhvani, A. M. Syed, J. Ngai, B. R. Kingston, L. Maiorino, J. Rothschild, P. MacMillan, Y. Zhang, N. U. Rajesh, T. Hoang, J. L. Y. Wu, S. Wilhelm, A. Zilman, S. Gadde, A. Sulaiman, B. Ouyang, Z. Lin, L. Wang, M. Egeblad, W. C. W. Chan, *Nat. Mater.* **2020**, *19*, 566.
- [183] V. Sheth, L. Wang, R. Bhattacharya, P. Mukherjee, S. Wilhelm, *Adv. Funct. Mater.* **2021**, *31*, 2007363.
- [184] X. Mou, J. Wang, X. Meng, J. Liu, L. Shi, L. Sun, *J. Lumin.* **2017**, *190*, 16.
- [185] M. Li, H. Fang, Q. Liu, Y. Gai, L. Yuan, S. Wang, H. Li, Y. Hou, M. Gao, X. Lan, *Biomater. Sci.* **2020**, *8*, 1802.
- [186] B. J. Tickner, G. J. Stasiuk, S. B. Duckett, G. Angelovski, *Chem. Soc. Rev.* **2020**, *49*, 6169.
- [187] U. Kostiv, J. Kučka, V. Lobaz, N. Kotov, O. Janoušková, M. Šlouf, B. Krajník, A. Podhorodecki, P. Francová, L. Šefc, D. Jiráček, D. Horák, *Sci. Rep.* **2020**, *10*, 20016.
- [188] M. E. Ladd, P. Bachert, M. Meyerspeer, E. Moser, A. M. Nagel, D. G. Norris, S. Schmitter, O. Speck, S. Straub, M. Zaiss, *Prog. Nucl. Magn. Reson. Spectrosc.* **2018**, *109*, 1.
- [189] S. Alonso-de Castro, E. Ruggiero, A. Lekuona Fernández, U. Cossío, Z. Baz, D. Otaegui, V. Gómez-Vallejo, D. Padro, J. Llop, L. Salassa, *Inorganics* **2019**, *7*, 60.
- [190] A. B. E. Attia, G. Balasundaram, M. Moothanchery, U. S. Dinish, R. Bi, V. Ntziachristos, M. Olivo, *Photoacoustics* **2019**, *16*, 100144.
- [191] D. Wang, W. Wei, A. Singh, G. S. He, R. Kannan, L.-S. Tan, G. Chen, P. N. Prasad, J. Xia, *ACS Photonics* **2017**, *4*, 2699.
- [192] R. Lv, D. Wang, L. Xiao, G. Chen, J. Xia, P. N. Prasad, *Sci. Rep.* **2017**, *7*, 15753.
- [193] M.-H. Chan, Y.-T. Pan, Y.-C. Chan, M. Hsiao, C.-H. Chen, L. Sun, R.-S. Liu, *Chem. Sci.* **2018**, *9*, 3141.
- [194] S. He, J. Song, J. Liu, L. Liu, J. Qu, Z. Cheng, *Adv. Opt. Mater.* **2019**, *7*, 1900045.
- [195] H. Zhuang, B. Li, M. Zhao, P. Wei, W. Yuan, M. Zhang, X. Han, Y. Chen, T. Yi, *Nanoscale* **2020**, *12*, 10216.
- [196] I. Blinova, M. Muna, M. Heinlaan, A. Lukjanova, A. Kahru, *Nanomaterials* **2020**, *10*, 328.
- [197] J. Zhao, D. Jin, E. P. Schartner, Y. Lu, Y. Liu, A. V. Zvyagin, L. Zhang, J. M. Dawes, P. Xi, J. A. Piper, E. M. Goldys, T. M. Monro, *Nat. Nanotechnol.* **2013**, *8*, 729.
- [198] G. Liang, H. Wang, H. Shi, H. Wang, M. Zhu, A. Jing, J. Li, G. Li, *J. Nanobiotechnology* **2020**, *18*, 154.
- [199] Y.-C. Yeh, B. Creran, V. M. Rotello, *Nanoscale* **2012**, *4*, 1871.

- [200] K. Mahato, S. Nagpal, M. A. Shah, A. Srivastava, P. K. Maurya, S. Roy, A. Jaiswal, R. Singh, P. Chandra, *3 Biotech* **2019**, *9*, 57.
- [201] O. US EPA, “Basics of Green Chemistry,” can be found under <https://www.epa.gov/greenchemistry/basics-green-chemistry>, **2013**.
- [202] D. Kim, N. Oh, K. Kim, S. Lee, C.-G. Pack, J.-H. Park, Y. Park, *Methods* **2018**, *136*, 160.
- [203] S. Burkitt, M. Mehraein, R. K. Stanciauskas, J. Campbell, S. Fraser, C. Zavaleta, *Nanomater. Basel Switz.* **2020**, *10*, E2239.
- [204] F. Wang, B. Chen, B. Yan, Y. Yin, L. Hu, Y. Liang, M. Song, G. Jiang, *J. Am. Chem. Soc.* **2019**, *141*, 14043.
- [205] K. Bromma, A. Bannister, A. Kowalewski, L. Cicon, D. B. Chithrani, *Cancer Nanotechnol.* **2020**, *11*, 8.
- [206] L. M. Bareford, P. W. Swaan, *Adv. Drug Deliv. Rev.* **2007**, *59*, 748.
- [207] M. Kaksonen, A. Roux, *Nat. Rev. Mol. Cell Biol.* **2018**, *19*, 313.
- [208] J. Couet, M. M. Belanger, E. Roussel, M. C. Drolet, *Adv. Drug Deliv. Rev.* **2001**, *49*, 223.
- [209] X. P. Lin, J. D. Mintern, P. A. Gleeson, *Membranes* **2020**, *10*, 177.
- [210] S. Song, Y. Zhang, T. Ding, N. Ji, H. Zhao, *Front. Oncol.* **2021**, *10*.
- [211] S. Behzadi, V. Serpooshan, W. Tao, M. A. Hamaly, M. Y. Alkawareek, E. C. Dreaden, D. Brown, A. M. Alkilany, O. C. Farokhzad, M. Mahmoudi, *Chem. Soc. Rev.* **2017**, *46*, 4218.
- [212] A. Panariti, G. Miserocchi, I. Rivolta, *Nanotechnol. Sci. Appl.* **2012**, *5*, 87.
- [213] V. M. Pulgar, *Front. Neurosci.* **2019**, *12*.
- [214] S. A. Smith, L. I. Selby, A. P. R. Johnston, G. K. Such, *Bioconjug. Chem.* **2019**, *30*, 263.
- [215] R. Firdessa, T. A. Oelschlaeger, H. Moll, *Eur. J. Cell Biol.* **2014**, *93*, 323.
- [216] J. Turkevich, P. C. Stevenson, J. Hillier, *Discuss. Faraday Soc.* **1951**, *11*, 55.
- [217] N. Raval, R. Maheshwari, D. Kalyane, S. R. Youngren-Ortiz, M. B. Chougule, R. K. Tekade, in *Basic Fundam. Drug Deliv.* (Ed.: R.K. Tekade), Academic Press, **2019**, pp. 369–400.
- [218] W. Yang, L. Wang, M. Fang, V. Sheth, Y. Zhang, A. M. Holden, N. D. Donahue, D. E. Green, A. N. Frickenstein, E. M. Mettenbrink, T. A. Schwemley, E. R. Francek, M. Haddad, M. N. Hossen, S. Mukherjee, S. Wu, P. L. DeAngelis, S. Wilhelm, *Nano Lett.* **2022**, *22*, 2103.
- [219] J. M. Hughes, P. M. Budd, A. Grieve, P. Dutta, K. Tiede, J. Lewis, *J. Appl. Polym. Sci.* **2015**, *132*, DOI 10.1002/app.42061.
- [220] H. K. Ardani, C. Imawan, W. Handayani, D. Djuhana, A. Harmoko, V. Fauzia, *Mater. Sci. Eng. Conf. Ser.* **2017**, *188*, 012056.
- [221] L. Kohler, M. Mader, C. Kern, M. Wegener, D. Hunger, *Nat. Commun.* **2021**, *12*, 6385.
- [222] P. Foroozandeh, A. A. Aziz, *Nanoscale Res. Lett.* **2018**, *13*, 339.
- [223] F. Chen, L. Zhu, Y. Zhang, D. Kumar, G. Cao, X. Hu, Z. Liang, S. Kuang, R. Xue, C. Gong, *Sci. Rep.* **2018**, *8*, 7268.
- [224] T. G. Phan, A. Bullen, *Immunol. Cell Biol.* **2010**, *88*, 438.
- [225] M. Sun, L. Xu, W. Ma, X. Wu, H. Kuang, L. Wang, C. Xu, *Adv. Mater.* **2015**, *28*, 898.
- [226] Y. Sun, Q. Liu, J. Peng, W. Feng, Y. Zhang, P. Yang, F. Li, *Biomaterials* **2013**, *34*, 2289.
- [227] Y. Qiao, S. Qiao, X. Yu, Q. Min, C. Pi, J. Qiu, H. Ma, J. Yi, Q. Zhan, X. Xu, *Nanoscale* **2021**, *13*, 8181.
- [228] H. Dong, L.-D. Sun, L.-D. Li, R. Si, R. Liu, C.-H. Yan, *J. Am. Chem. Soc.* **2017**, *139*, 18492.

- [229] M. Nyk, R. Kumar, T. Y. Ohulchanskyy, E. J. Bergey, P. N. Prasad, *Nano Lett.* **2008**, *8*, 3834.
- [230] Q. Chen, X. Xie, B. Huang, L. Liang, S. Han, Z. Yi, Y. Wang, Y. Li, D. Fan, L. Huang, X. Liu, *Angew. Chem.* **2017**, *129*, 7713.
- [231] D. Li, S. Wen, M. Kong, Y. Liu, W. Hu, B. Shi, X. Shi, D. Jin, *Anal. Chem.* **2020**, *92*, 10913.
- [232] H. Du, J. Yu, D. Guo, W. Yang, J. Wang, B. Zhang, *Langmuir* **2016**, *32*, 1155.
- [233] J. Park, M. Xu, F. Li, H.-C. Zhou, *J. Am. Chem. Soc.* **2018**, *140*, 5493.
- [234] W. Liu, R. Chen, S. He, *J. Innov. Opt. Health Sci.* **2019**, *12*, 1950013.
- [235] A. N. Generalova, V. V. Rocheva, A. V. Nechaev, D. A. Khochenkov, N. V. Sholina, V. A. Semchishen, V. P. Zubov, A. V. Koroleva, B. N. Chichkov, E. V. Khaydukov, *RSC Adv.* **2016**, *6*, 30089.
- [236] J. Wu, J. Liu, B. Lin, R. Lv, Y. Yuan, X. Tao, *ACS Biomater. Sci. Eng.* **2021**, *7*, 1640.
- [237] L. Liu, S. Wang, B. Zhao, P. Pei, Y. Fan, X. Li, F. Zhang, *Angew. Chem. Int. Ed.* **2018**, *57*, 7518.
- [238] E. L. Guryev, N. O. Volodina, N. Y. Shilyagina, S. V. Gudkov, I. V. Balalaeva, A. B. Volovetskiy, A. V. Lyubeshkin, A. V. Sen', S. A. Ermilov, V. A. Vodeneev, R. V. Petrov, A. V. Zvyagin, Z. I. Alferov, S. M. Deyev, *Proc. Natl. Acad. Sci.* **2018**, *115*, 9690.
- [239] M. Xu, X. Zou, Q. Su, W. Yuan, C. Cao, Q. Wang, X. Zhu, W. Feng, F. Li, *Nat. Commun.* **2018**, *9*, 2698.
- [240] B. Liu, C. Li, B. Xing, P. Yang, J. Lin, *J. Mater. Chem. B* **2016**, *4*, 4884.
- [241] J. Xu, P. Yang, M. Sun, H. Bi, B. Liu, D. Yang, S. Gai, F. He, J. Lin, *ACS Nano* **2017**, *11*, 4133.
- [242] Y. Wang, G. Yang, Y. Wang, Y. Zhao, H. Jiang, Y. Han, P. Yang, *Nanoscale* **2017**, *9*, 4759.
- [243] Q. Liu, Y. Sun, C. Li, J. Zhou, C. Li, T. Yang, X. Zhang, T. Yi, D. Wu, F. Li, *ACS Nano* **2011**, *5*, 3146.